Exotic forms of matter created by interactions with free-electron lasers

Henry Isaac Bryan Banks

A dissertation submitted in partial fulfillment

of the requirements for the degree of

Doctor of Philosophy

of

University College London.

Department of Physics and Astronomy

University College London

February 6, 2019

I, Henry Isaac Bryan Banks, confirm that the work presented in this thesis is my own. Where information has been derived from other sources, I confirm that this has been indicated in the work.

The parts of this thesis that have been published individually are listed below:

Chapter 3: A. O. G. Wallis, H. I. B. Banks, and A. Emmanouilidou. Traces in ion yields and electron spectra of the formation of Ar inner-shell hollow states by free-electron lasers. *Phys. Rev. A*, 91:063402, Jun 2015

Chapter 5: H. I. B. Banks, D. A. Little, J. Tennyson, and A. Emmanouilidou. Interaction of molecular nitrogen with free-electron-laser radiation. *Phys. Chem. Chem. Phys.*, 19:19794–19806, 2017

Chapter 6: H. I. B. Banks, D. A. Little, and A. Emmanouilidou. Multiple core-hole formation by free-electron laser radiation in molecular nitrogen. *Journal of Physics B: Atomic, Molecular and Optical Physics*, 51(9):095001, 2018

Abstract

In this thesis, we investigate the formation of atomic and molecular states with multiple core electrons missing. These multiple-core-hole (MCH) states are of interest due to their sensitivity to their chemical environment. These MCH states are formed by successive single-photon ionisations of core electrons. This can be achieved by x-ray photons and a sufficiently large intensity such that the photo-ionisation rate competes with the Auger decay rate of core-hole states.

To understand the pathways that lead to the formation of MCH states, we study the interaction of free-electron laser (FEL) pulses with atoms and molecules. These lasers are capable of producing short, high-intensity pulses with high photon energy, which make them ideal for forming MCH states. In order to understand the interaction of an FEL with an atom or molecule, we model these interactions computationally. We construct rate equations and track how the population of an atom or molecule transitions between different states. These rate equations involve single-photon ionization processes and Auger transitions. To account for these processes, we compute photo-ionisation cross-sections and Auger decay rates.

We develop a computational model that allows us to calculate the ion yields produced when an atom or molecule interacts with an FEL pulse. Further, by calculating how the population transitions via different pathways of intermediate atomic and molecular states, we determine the proportion of the population which accesses MCH states. We also compute electron spectra, which provide measurable observables indicating the formation of MCH states.

Impact Statement

Molecules with missing core electrons on multiple atomic sites are sensitive to their chemical environment and can act as a basis for spectroscopic measurements. However, these states are also extremely short-lived and their creation typically requires very high photon flux. As a result, it is important to understand the processes that create these states and the conditions that maximise their creation. Free-electron lasers are ideal for producing these core-hole states due to the high pulse intensity, short duration and high-energy photons involved. Free-electron lasers (FELs) also provide new methods of producing high-resolution images of molecules. These lasers are also capable of producing high-intensity pulses that can image molecules before the molecule breaks down due to sequential ionisation and the resultant Coulomb forces.

To explore FEL interactions with atoms and molecules, we construct rate equation models that allow us to investigate how population transfers between different states. To account for the transitions in these interactions, we calculate the photo-ionisation cross-sections and Auger rates. For the molecular calculations, we computed molecular bound and continuum orbital wavefunctions. By using molecular orbital wavefunctions, we can obtain more accurate values than calculations using atomic continuum orbitals. Using these rate equation models, we were able to recreate experimental results. We also vary the pulse parameters to investigate the effects of different parameters on the ion yields and electron spectra produced by FEL pulses. Further, we determine the sequences of transitions that form these states and determine the proportions of the population that followed each sequence of transitions. This allows us to explore the formation of intermediate states, such

as multiple-core-hole states. By theoretically modelling laser-matter interactions, we obtain a better understanding of the processes involved and how different types of transitions contribute to the final yields.

Acknowledgements

Firstly, I'd like to thank my supervisor, Dr Agapi Emmanouilidou, for all of her help and support throughout my PhD. In addition, the post-docs Dr Duncan Little and Dr Alisdair Wallis were both extremely helpful and taught me a lot. I also must thank the other members of the group, Dr Ahai Chen, Dr Hugh Price, Dr Arnau Casanovas and George Katsoulis for their enlightening and entertaining discussions.

On a more personal note, I thank my father, Keith Banks for his ever-present love and support and my sister, Isabel Banks, whose own academic accomplishments spurred me on in a way that only sibling rivalry can achieve. I'm also extremely grateful to Adrienn Győri for her love and for putting up with my various short-comings.

Lastly I'd like to thank all of my friends at UCL, in particular: Dr Katy Chubb, Dr Tom Galley, Richard Juggins, Dr Jacob Lang, Andy Maxwell, Tom Meltzer, Haneesh Sidhu, Mike Staddon and Albert Wood. My time at UCL has been enjoyable and has taught me a lot, both about myself and about calculating Auger rates in atoms and molecules.

Contents

List of Figures

List of Tables

Chapter 1

Introduction

The advent of x-ray free-electron lasers (FELs) [4, 5] has introduced new tools for the imaging and exploration of novel states of atoms and molecules [6, 7]. These lasers are capable of producing high intensity ($\sim 10^{18}\,\mathrm{Wcm^{-2}}$) pulses with x-ray photons and femtosecond durations [8]. The high photon energy means that these pulses can produce high-resolution images of molecules and the high intensity means that these molecules can be imaged before they break down due to radiation damage [9, 10, 11, 12]. As the molecule is ionised, it will be distorted by to the Coulomb repulsion of the positively-charged holes. The high intensity of FEL pulses means the molecular structure can be imaged before it changes significantly. The short, high intensity FEL pulses with x-ray photons are also ideal for the creation of multiple-core-hole (MCH) states.

In MCH states, multiple electrons have been ionised from the core orbitals of an atom or molecule. To produce these states, we must first ionise a single core electron, creating a single-core-hole (SCH) state. Due to the energy difference between core and valence electrons, states with core holes are unstable and will decay rapidly via the Auger process. In this process, a core hole is filled in by a more excited electron and the released energy ejects another electron. This means that to produce a MCH state, a second core ionisation must occur before the SCH state can decay. X-ray FELs are ideal for producing these states, as they have sufficiently high-energy photons to photo-ionise core electrons and, due to the high intensity of the pulse, photo-ionisation competes with Auger decay. In addition, the short

pulse duration means that the high-intensity portion of the pulse will be reached before too many transitions have occurred. This ensures that a large proportion of the population will remain unionised until the high-intensity portion of the pulse is reached.

MCH states are of interest primarily because of their chemical sensitivity. When there are two core holes on different atomic sites, i.e. a two-site double-core-hole state (TSDCH), the energy of the state will be highly dependent on the chemical environment [13, 14, 15, 16]. This energy sensitivity is caused by the relaxation of the other electrons, due to the changing potential, and the Coulomb repulsion between the core vacancies. TSDCH states have been the focus of a large amount of experimental work [17, 18, 19, 20, 21] as well as theoretical studies [16, 22, 23].

Other work also investigated the energy levels of different MCH states, calculated using a variety of techniques and basis sets in molecular nitrogen [24]. Triple-core-hole (TCH) states have also been studied. The creation of triply excited hollow states in laser-driven Lithium with subsequent auto-ionisation to doubly excited states [25] and the production of TCH states in plasmas with optical lasers have also been studied [26].

The interaction of FELs with atoms, in particular noble gases, has been the subject of a large body of work [27, 28, 29, 30, 31, 32, 33]. These interactions are dictated by the interplay of single-photon ionisations and Auger decay transitions. There has been a significant amount of work on calculating these Auger rates and photo-ionisation cross sections in atoms [34, 35, 36, 37, 38, 39]. In order to understand the interplay of the photo-ionisation and Auger decay transitions that occur due to FEL interactions with an atom, we model these interactions using rate equations [34, 40]. This requires us to calculate the photo-ionisation cross-sections and Auger rates for all available transitions and the bound and continuum orbital wavefunctions in order to obtain these rates. We initially model the interactions of FELs with atoms, as opposed to molecules, as there are no dissociative transitions and the symmetry of the atom simplifies the calculations.

Using this rate equation model, we were able to calculate the ion yields produced by interactions with various FEL pulses. Further, by considering the series of states by which the population transitions to these final ion yields, we were able to compute the proportion of the population which accessed different MCH states. These pathways of states will contribute different amounts to the final ion yields and, by calculating the transition rates between different pathways, we determined the population that passes through all intermediate states. These pathway calculations also allowed us to identify sets of transitions that would preferentially populate atomic states with odd or even charge [1]. We were able to determine why certain ions were populated and identify the conditions that led to their population.

After working on atoms, we move to the molecular case in chapters 4, 5 and 6. Previous molecular studies with FEL radiation include models where the molecule is treated as a combination of independent atoms. Then, in these models, the Auger rates and the photo-ionisation cross sections are computed for atomic transitions [22, 23]. These atomic rates are then used to setup rate equations to describe molecular interactions with FEL radiation and dissociation is accounted for through additional terms in the rate equations. For high photon energy FEL pulses interacting with N_2, these models have been used to compute the yields of the final atomic ion fragments as well as the contribution of the DCH molecular states in the yields of the final atomic ions. Very recently, new methods have been developed to describe molecular states with multiple holes and to compute molecular transitions following interaction with FEL radiation [41, 42]. These models describe molecular orbitals as linear combinations of the appropriate atomic orbitals and utilise the Hartree-Fock-Slater approximation to calculate the continuum wavefunctions. These new methods have been employed to compute the yields of the final molecular ion states as well as the contribution of SCH and DCH states in water for fixed nuclei [43]. The calculations in these studies were performed with atomic continuum orbitals rather than molecular ones. The use of atomic continuum orbitals is a good approximation when these models are employed to study molecular interactions with high photon energy FEL pulses.

Previous studies [20, 44] have identified the time delay between subsequent PA steps, with PA consisting of a single-photon ionisation (P) and an Auger decay (A), as well as the inter-nuclear distance at the time these steps take place. It has been shown in experiments [20] that when comparing laser pulses of the same intensity but of different duration, PA events take place at smaller inter-nuclear distances for the smaller duration laser pulses. Similarly, when comparing laser pulses of the same duration but of different intensity, PA events take place at smaller inter-nuclear distances for the higher intensity laser pulses [20]. Thus, for laser pulses of small pulse duration and of high intensity the molecular transitions at small inter-nuclear distances are important rendering the effect of the nuclear motion less important. In addition, it follows that the use of molecular continuum orbitals versus atomic continuum orbitals will result in more accurate results mostly for small duration and high intensity FEL pulses.

We model the interaction of a molecule with an FEL pulse. In molecules, there are three important types of transitions that take place during the interaction; photo-ionisation, Auger decay and dissociation. As we remove electrons from the molecule, it will become unstable and break down due to the Coulomb repulsion. Due to this dissociation, it is necessary to construct atomic and molecular rate equations, to take into account the transitions that occur after dissociation. Because of our previous work on atoms, we already have the tools needed for the atomic rate equations. There is a large body of work on calculating Auger rates and photo-ionisation cross sections in molecules [45, 46, 47, 48, 49, 50, 51]. To calculate the Auger rates, cross-sections and continuum wavefunctions, we use the single-centre expansion formalism [52] to express our wavefunctions in terms of spherical harmonics. This allows us to perform these calculations semi-analytically and is less computationally intensive than a fully numeric procedure.

We use molecular bound and molecular continuum orbitals to compute single-photon ionisation and Auger rates. This is an advantage over previous calculations where the molecule is treated as a combination of atoms [23] and over computations where atomic rather than molecular continuum orbitals are employed to de-

scribe the interaction of molecules with FEL laser pulses [43]. The use of molecular continuum orbitals versus atomic continuum orbitals will yield more accurate results for low photon-energy FEL pulses as well as short duration and high intensity FEL pulses [20]. This is because molecular continuum wavefunctions will more accurately describe electrons emitted with low energy than atomic continuum wavefunctions, as these low-energy electrons will be more affected by the potential of the molecule. In addition, we compute the molecular continuum orbitals without approximating the exchange interaction using the Slater exchange potential, unlike existing work [41]. We then employ these orbitals to compute the Auger rates and the single-photon ionisation cross sections for all molecular transitions that are energetically accessible.

N_2 interacting with FEL pulses has been the subject of many experimental studies [19, 20, 53, 54, 55]. In these studies the yields of the final atomic ion states and the formation of molecular DCHs are investigated. We model the interaction of the N_2 diatomic molecule with FEL radiation using rate equations to understand the transitions that occur during this interaction. In particular, we investigate the interaction of a 525 eV and a 1100 eV FEL pulse with N_2. These photon energies are sufficient to create three inner-shell holes through sequential single-photon absorptions and multiple valence holes in the ground state of N_2. Moreover, for a 525 eV FEL pulse some of the electrons ionise with very small energies. These small energies necessitate the use of molecular continuum orbitals, for the reasons discussed above. We compute the Auger and the single-photon ionisation processes for the allowed molecular transitions, thus improving over previous studies that consider only atomic transitions [23]. We note that the use of molecular bound state orbitals is important for obtaining electron spectra. Indeed, it has been shown that with high-resolution electron spectroscopy one can observe the energy splitting of the molecular core hole states $1\sigma_g$ and $1\sigma_u$ [47, 56]. We account for the dissociative transitions phenomenologically, treating them as additional transitions in the rate equations with rates given by their experimental lifetimes.

We compare the atomic ion yields, produced by FEL interactions with N_2, to

experimental results [23, 55] and find very good agreement in all cases. We then investigate the dependence of the final molecular and atomic ion yields on the intensity and pulse duration of the FEL pulse. Moreover, we compute the population that transitions through all energetically accessible pathways of states. Using this we determine the contribution of the DCH molecular states in the final atomic ion states. Additionally, we calculate the electron spectra produced in these FEL interactions and its dependence on the pulse parameters. Using these electron spectra, we can determine whether photo-ionisation or Auger transitions in the electron spectra are more effective in detecting the formation of DCH molecular states.

In chapter 6, we investigate the formation of SSDCH, TSDCH and TCH states in FEL-driven N_2. We register the percentage of the final atomic ion yields that transitions through DCH or TCH molecular states. Moreover, at each time step of our computations, we project the occupied delocalized molecular orbitals of the DCH molecular states onto orbitals localized on an atomic site. Thus, we determine the percentage of DCH molecular states that correspond to TSDCH and to SSDCH molecular states. Finally, we compute the percentage of the total population that accesses TSDCH, SSDCH and TCH molecular states as a function of the intensity of the FEL pulse.

Chapter 2

Atomic interactions with a free-electron laser pulse

2.1 Theory

Since the creation of x-ray free-electron lasers (FELs) [4], it has been possible to create laser pulses with high intensity and short pulse length which provide x-ray photons. These pulse parameters mean that x-ray FELs are ideal for the production of multiple-core-hole (MCH) states. In order to understand the interaction between an FEL pulse and an atom, we model the interaction computationally. We use a system of rate equations to calculate the population in each atomic state. In addition, we also use rate equations to calculate the population transfer through each pathway of different states. In order to do this, we must understand the processes involved in the laser-matter interaction. For x-ray FEL interactions with atoms, the salient transitions are single-photon ionisation and Auger decay. Therefore, in order to model the interaction of an atom with an FEL pulse, we must first calculate the Auger decay rates and the photo-ionisation cross-sections. In this section, we explain how we calculate these rates and cross-sections and how we construct the rate equations.

2.2 Atomic Auger rates

2.2.1 The Auger process
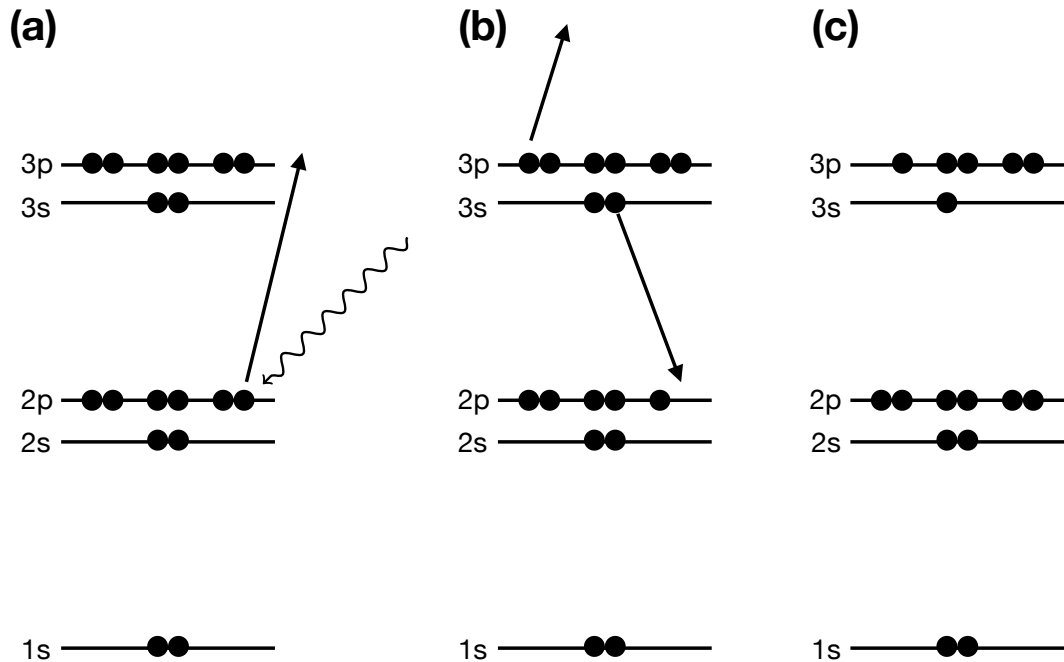
Figure 2.1: Diagram of an Auger decay. In (a), a core electron is photo-ionised from the
atom, creating an ion with a core hole. In (b), a valence electron drops to fill
this vacancy and the energy released is transferred to another valence electron,
which is ejected from the atom. In (c), we see the final state of the atom, with
a fully occupied core and two missing valence electrons.

An example of the Auger process is shown in Fig. 2.1. Here, we produce a core-
hole state via photo-ionisation of an inner-shell electron, which then decays via
an Auger transition. In the Auger process a, typically valence, electron transitions
to fill the core hole. This transition releases energy, due to the different binding
energies of the core and valence orbitals. This energy is transferred to another,
typically valence, electron, which is then ejected from the atom with kinetic energy,
$K = E_{V1} + E_{V2} - E_C$. Here, K is the kinetic energy of the electron escaping into the
continuum and E_C, E_{V1} and E_{V2} are the energies of the core and valence electrons,
respectively.

2.2.2 Coster-Kronig transitions
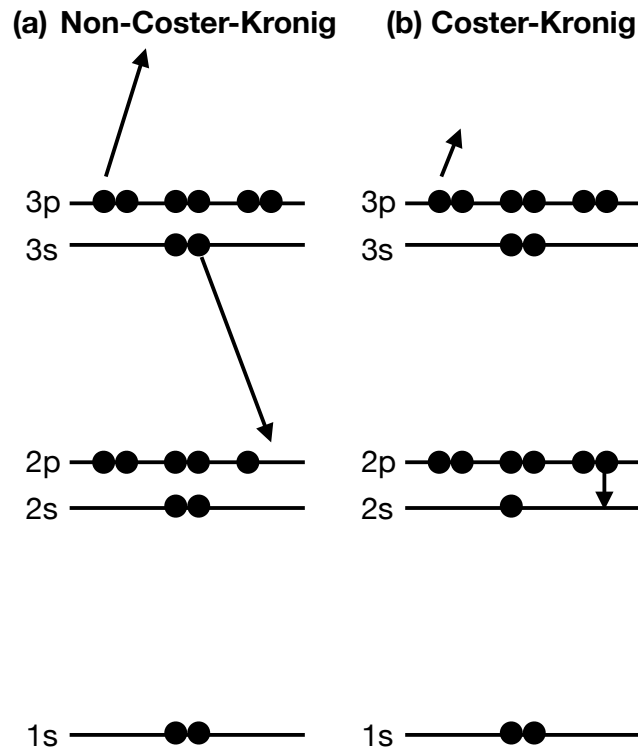
Figure 2.2: Energy level diagram of a Coster-Kronig transition compared to a non-Coster-Kronig Auger transition. In (a), an Auger transition occurs where a 2p hole is filled by a 3s electron and a 3p electron is ejected. In (b) a 2p electron fills in a 2s hole and a 3p electron is ejected. The transition in (b) is a Coster-Kronig transition and the kinetic energy of the emitted electron is smaller (represented by the shorter arrow).

Coster-Kronig transitions are a subset of Auger transitions in which the electron that fills in the hole comes from the same shell, but a different sub-shell, as the core hole [57]. This releases less energy than transitions where an electron from a higher shell fills in the hole. As a result, the ejected electron in a Coster-Kronig transition will have lower kinetic energy than in a typical Auger transition. These transitions tend to be more probable than other Auger transitions, as the electron filling in the core hole will have a similar radial distribution to the hole wavefunction. These transitions are of interest to us because there can be additional Auger decay after the Coster-Kronig transition. Super-Coster-Kronig transitions also exist [57], in which both the electron that fills the hole and the ejected electron come from the same shell as the hole, but these were not encountered in this work.

2.2.3 Derivation

The total Auger transition rate can be found from Fermi's Golden Rule [58], eqn (2.1), where the interaction Hamiltonian, H', for the Auger transition is the electron-electron interaction and is given by $\sum_{i>j} 1/r_{ij}$.

$$\Gamma_{i \to f} = 2\pi\rho \left| < f \left| H' \right| i > \right|^2.$$ (2.1)

Here, $|i\rangle$ and $|f\rangle$ are the initial and final states, respectively and $\rho = \delta(E_i - E_f)$ is the density of final states in energy space. Summing over the possible final energies removes this delta function. To calculate a particular Auger rate for two electrons in valence orbitals to fill a core hole, we compute the group rates. These rates describe the transitions involving two electrons, initially described by $n_1 l_1$ and $n_2 l_2$, filling a vacancy, $n_3 l_3$, and resulting in one continuum electron described by εl_4, where ε is the energy of the continuum electron. This is written as

$$T_A(n_3 l_3 \leftarrow n_1 l_1, n_2 l_2) = 2\pi N_{12} \overline{\sum} \left| < f \left| H' \right| i > \right|^2.$$ (2.2)

The symbol $\overline{\sum}$ refers to the sum and average over the final and initial states, respectively. N_{12} is the weighting factor that corresponds to the occupancy of the $n_1 l_1$ and $n_2 l_2$ orbitals, which are denoted by N_1 and N_2 respectively, N_{12} is given as follows:

$$\begin{aligned} N_{12} &= \frac{N_1 N_2}{(4l_1 + 2)(4l_2 + 2)} && (n_1 l_1 \neq n_2 l_2) \\ &= \frac{N_1(N_1 - 1)}{2(4l_1 + 2)(4l_1 + 2 - 1)} && (n_1 l_1 = n_2 l_2) \end{aligned}$$ (2.3)

Here, we have introduced an additional factor of $1/2$ to avoid double counting in

the case of identical initial electrons. Expanding out eqn (2.2) gives

$$T_A(n_3 l_3 \leftarrow n_1 l_1, n_2 l_2) = \frac{2\pi N_{12} N_h}{2(2l_3 + 1)} \sum_{\substack{LSJM \\ L'S'J'M'}} \sum_{l_4} |<f|H'|i>|^2. \tag{2.4}$$

Here, N_h is the number of core holes in the $n_3 l_3$ orbital. As we are working in the *LSJM* scheme, we sum over these quantum numbers to find the total Auger rate[59]. We divide by $2(2l_3 + 1)$ to average over the different core hole possibilities. To use this formula, we must first calculate the atomic orbital wavefunctions of both the bound and continuum electrons, this process is explained in section 2.3.

2.2.3.1 Matrix element

The matrix element, for a given two electron transition, is given by

$$\mathcal{M} = \left\langle f \left| \frac{1}{r_{12}} \right| i \right\rangle = \left\langle \Psi_f(1, 2, ..., N) \left| \frac{1}{r_{12}} \right| \Psi_i(1, 2, ..., N) \right\rangle. \tag{2.5}$$

Here, Ψ_i and Ψ_f are the anti-symmetrised wavefunctions of the initial and final states of the atom. The numbers $1, 2, ..., N$ refer to the electrons in the wavefunctions. As only two electrons are involved in this transition, this can be simplified to

$$\mathcal{M} = \left\langle \Psi_f(1, 2) \left| \frac{1}{r_{12}} \right| \Psi_i(1, 2) \right\rangle, \tag{2.6}$$

where $\Psi_i(1, 2)$ and $\Psi_f(1, 2)$ are the initial and final anti-symmetrised two-electron wavefunctions. Writing the anti-symmetrisation explicitly gives

$$\begin{aligned} \mathcal{M} &= \left(\frac{\langle \Psi(\gamma'|12)| - \langle \Psi(\gamma'|21)|}{\sqrt{2}} \right) \frac{1}{r_{12}} \left(\frac{|\Psi(\gamma|12)\rangle - |\Psi(\gamma|21)\rangle}{\sqrt{2}} \right) \\ &= \langle \Psi(\gamma'|12)| \frac{1}{r_{12}} |\Psi(\gamma|12)\rangle - \langle \Psi(\gamma'|12)| \frac{1}{r_{12}} |\Psi(\gamma|21)\rangle. \end{aligned} \tag{2.7}$$

Here $\Psi(\gamma|12)$ and $\Psi(\gamma'|12)$ correspond to the initial and final state of the system respectively, with electron 1 in the first orbital and electron 2 in the second orbital. γ is used to represent the various quantum numbers that define the wavefunction. In this case, we used the $n_1 l_1 n_2 l_2 LSJM$ scheme[60] was used following the work of Bhalla *et al.* [37]. In this scheme, the two electron wavefunctions are described in terms of the principle, n, and orbital, l, quantum numbers of each electron as well as the total orbital angular momentum, L, the total spin, S, and the total angular momentum, J, and its projection, M. The first part of the right hand of eqn (2.7) corresponds to the direct matrix element, where the electron order is preserved, while the second part corresponds to the exchange interaction, in which the electron order is switched.

2.2.3.2   Direct matrix element

The operator can be rewritten using the multipole expansion [60],

$$\frac{1}{r_{12}} = \sum_k \frac{r_<^k}{r_>^{k+1}} \mathbf{C}^{(k)}(\Omega_1) \cdot \mathbf{C}^{(k)}(\Omega_2), \tag{2.8}$$

where $r_< = \min(r_1, r_2)$ and $r_> = \max(r_1, r_2)$. $\mathbf{C}^{(k)}(\Omega_1)$ and $\mathbf{C}^{(k)}(\Omega_2)$ are spherical tensor operators [61] of order k, each with 2k+1 elements corresponding to spherical harmonics,

$$C_q^{(k)}(\Omega) = \sqrt{\frac{4\pi}{2k+1}} Y_{kq}(\Omega). \tag{2.9}$$

These terms depend on the angular coordinates, $\Omega_1 = (\theta_1, \phi_1)$, of electron 1 and 2, respectively. The tensor dot product [60] is defined as

$$\mathbf{C}^{(k)}(\Omega_1) \cdot \mathbf{C}^{(k)}(\Omega_2) = \sum_{q=-k}^{k} (-1)^q C_q^{(k)}(\Omega_1) C_{-q}^{(k)}(\Omega_2). \tag{2.10}$$

where Y_{kq} is a spherical harmonic with orbital angular momentum k and magnetic

quantum number q. We then use this to rewrite the direct matrix element in the $n_1l_1, n_2l_2, LSJM$ scheme. For a transition filling a hole in n_3l_3 and ejecting an electron to εl_4, where ε is the energy of the continuum electron, with two electrons originally in the n_1l_1 and n_2l_2 orbitals, this can be written as

$$
\begin{aligned}
\langle\Psi(\gamma'&|12)|\frac{1}{r_{12}}|\Psi(\gamma|12)\rangle \\
&= \sum_k \langle\Psi(n_3l_3, \varepsilon l_4, L'S'J'M'|12)|\frac{r_<^k}{r_>^{k+1}}\mathbf{C}^{(k)}(\Omega_1)\cdot\mathbf{C}^{(k)}(\Omega_2)|\Psi(n_1l_1, n_2l_2, LSJM|12)\rangle \\
&= \sum_k R^k(n_1l_1, n_2l_2, n_3l_3, \varepsilon l_4)\langle l_3l_4L'S'J'M'|\mathbf{C}^{(k)}(\Omega_1)\cdot\mathbf{C}^{(k)}(\Omega_2)|l_1l_2LSJM\rangle.
\end{aligned}
\tag{2.11}
$$

$\frac{r_<^k}{r_>^{k+1}}$ is purely a radial function, therefore we can separate it from the angular parts and rewrite it as $R^k(n_1l_1, n_2l_2, n_3l_3, \varepsilon l_4)$, defined as

$$
R^k(n_1l_1, n_2l_2, n_3l_3, \varepsilon l_4) = \int_0^\infty \int_0^\infty P_{n_1l_1}(r_1)P_{n_2l_2}(r_2)\frac{r_<^k}{r_>^{k+1}}P_{n_3l_3}(r_1)P_{n_4l_4}(r_2)dr_1dr_2.
\tag{2.12}
$$

$\frac{1}{r}P_{n_1l_1}(r)$ is the radial wavefunction of the orbital n_1l_1. The operator $\frac{1}{r_{12}}$ is independent of spin, which allows us to rewrite the angular component of the matrix element by splitting it into an element containing spin and an element with no spin dependence. First, we rewrite this operator into two parts:

$$
\mathbf{C}^{(k)}\cdot\mathbf{C}^{(k)} \equiv \mathbf{T}^{(0)} = \mathbf{T}^{(0)}\cdot\mathbf{I}^{(0)}
\tag{2.13}
$$

$\mathbf{T}^{(0)}$ is a tensor of rank 0, a scalar. It can equivalently be written as a scalar product of itself and the rank 0 identity, $\mathbf{I}^{(0)}$. The operator $\mathbf{T}^{(0)}$ concerns the angular dependence and $\mathbf{I}^{(0)}$ concerns the spin depedence. This fact can be used to simplify the matrix element by changing to the $l_1l_2LM_LSM_S$ scheme where spin and orbital

angular momentum are no longer coupled.

$$\langle l_3 l_4 L'S'J'M'|\mathbf{C}^{(k)}(\Omega_1) \cdot \mathbf{C}^{(k)}(\Omega_2)|l_1 l_2 LSJM\rangle = \langle l_3 l_4 L'S'J'M'|\mathbf{T}^{(0)} \cdot \mathbf{I}^{(0)}|l_1 l_2 LSJM\rangle$$

$$(2.14)$$

$|l_1 l_2 LSJM\rangle$ is rewritten in terms of $|l_1 l_2 LM_L SM_S\rangle$ in eqn (2.15) by using Clebsch-Gordan (CG) coefficients [60]. The CG coefficient is written as $(LM_L SM_S|JM) \equiv \langle l_1 l_2 LM_L SM_S|l_1 l_2 LSJM\rangle$.

$$\begin{aligned}|l_1 l_2 LSJM\rangle &= \sum_{M_L M_S} |l_1 l_2 LM_L SM_S\rangle\langle l_1 l_2 LM_L SM_S|l_1 l_2 LSJM\rangle \\ &\equiv \sum_{M_L M_S} (LM_L SM_S|JM)|l_1 l_2 LM_L SM_S\rangle\end{aligned}$$

$$(2.15)$$

Substituting this expression into both the bra and the ket in eqn (2.14) we obtain

$$\langle l_3 l_4 L'S'J'M'|\mathbf{T}^{(0)} \cdot \mathbf{I}^{(0)}|l_1 l_2 LSJM\rangle =$$
$$\sum_{M_L M_S M'_L M'_S} \langle l_3 l_4 L'M'_L S'M'_S|\mathbf{T}^{(0)} \cdot \mathbf{I}^{(0)}|l_1 l_2 LM_L SM_S\rangle(LM_L SM_S|JM)(J'M'|L'M'_L S'M'_S).$$

$$(2.16)$$

Because $\mathbf{T}^{(0)} \cdot \mathbf{I}^{(0)}$ is a scalar, there are restrictions on the quantum numbers in eqn (2.16) which will result in a non-zero matrix element (listed in eqn (2.17)). These selection rules are given in [60] and follow from the angular momentum addition selection rules.

$$L' = L \qquad M'_L = M_L \qquad S' = S \qquad M'_S = M_S \qquad (2.17)$$

These can be expressed as delta functions, allowing the expression to be simplified. Because of the $\delta_{LL'}$ and $\delta_{SS'}$ we can change all L' to L and S' to S and lose no

generality:

$$\langle l_3 l_4 L'S'J'M'|\mathbf{T}^{(0)}\cdot\mathbf{I}^{(0)}|l_1 l_2 LSJM\rangle =$$

$$\delta_{LL'}\delta_{SS'}\sum_{M_L M_S}\langle l_3 l_4 LM_L SM_S|\mathbf{T}^{(0)}\cdot\mathbf{I}^{(0)}|l_1 l_2 LM_L SM_S\rangle(LM_L SM_S|JM)(J'M'|LM_L SM_S)$$

$$(2.18)$$

Using the orthonormality of Clebsch-Gordan coefficients [62],

$$\sum_{M_L, M_S}(J'M'|LM_L SM_S)(LM_L SM_S|JM) = \delta_{JJ'}\delta_{MM'},\qquad(2.19)$$

this summation can be resolved into a simpler form, as shown in eqn (2.20). The matrix element $\langle l_3 l_4 LM_L SM_S|\mathbf{T}^{(0)}\cdot\mathbf{I}^{(0)}|l_1 l_2 LM_L SM_S\rangle$ is independent of M_L and M_S. This can be seen explicitly in eqn (2.23) and eqn (2.24) and can be understood physically as the Auger transition, which is an internal process, having no dependence on the orientation of the total system.

$$\langle l_3 l_4 L'S'J'M'|\mathbf{T}^{(0)}\cdot\mathbf{I}^{(0)}|l_1 l_2 LSJM\rangle =$$

$$\delta_{LL'}\delta_{SS'}\delta_{JJ'}\delta_{MM'}\langle l_3 l_4 LM_L SM_S|\mathbf{T}^{(0)}\cdot\mathbf{I}^{(0)}|l_1 l_2 LM_L SM_S\rangle$$

$$(2.20)$$

Because L and S are decoupled and independent, the matrix element can be written as the product of two matrix elements, as shown in eqn (2.21).

$$\langle l_3 l_4 L'S'J'M'|\mathbf{T}^{(0)}\cdot\mathbf{I}^{(0)}|l_1 l_2 LSJM\rangle =$$

$$\delta_{LL'}\delta_{SS'}\delta_{JJ'}\delta_{MM'}\langle l_3 l_4 LM_L|\mathbf{T}^{(0)}_0|l_1 l_2 LM_L\rangle\langle SM_S|\mathbf{I}^{(0)}_0|SM_S\rangle$$

$$(2.21)$$

The Wigner-Eckhart theorem [62] can be used to separate a matrix element into two parts, one of which depends on the projections of the angular momenta and a part which is independent of the orientations. It is given in eqn (2.22) where

$\langle \gamma' j' || \mathbf{T}^{(k)} || \gamma j \rangle$ is the reduced matrix element [60] and has no dependence on the projections of the angular momenta.

$$\langle \gamma' j' m' | \mathbf{T}_q^{(k)} | \gamma j m \rangle = (-1)^{k-j+j'} \frac{(kqjm|j'm')}{\sqrt{2j'+1}} \langle \gamma' j' || \mathbf{T}^{(k)} || \gamma j \rangle \tag{2.22}$$

By applying eqn (2.22) separately to the orbital angular momentum and the spin elements of the right hand side of eqn (2.21), we receive eqn (2.23) and eqn (2.24). Eqn (2.25) is given in [60] and follows from angular momentum addition rules.

$$\langle l_3 l_4 L M_L | \mathbf{T}_0^{(0)} | l_1 l_2 L M_L \rangle = (-1)^{L-L} \frac{(00LM_L|LM_L)}{\sqrt{2L+1}} \langle l_3 l_4 L || \mathbf{T}^{(0)} || l_1 l_2 L \rangle \tag{2.23}$$

$$\langle S M_S | \mathbf{I}_0^{(0)} | S M_S \rangle = (-1)^{S-S} \frac{(00SM_S|SM_S)}{\sqrt{2S+1}} \langle S || \mathbf{I}^{(0)} || S \rangle \tag{2.24}$$

$$(00SM_S|SM_S) = (00LM_L|LM_L) = 1 \tag{2.25}$$

Combining these equations, we obtain a new expression for the matrix element given in eqn (2.26):

$$\langle l_3 l_4 L' S' J' M' | \mathbf{T}^{(0)} \cdot \mathbf{I}^{(0)} | l_1 l_2 LSJM \rangle =$$
$$\delta_{LL'} \delta_{SS'} \delta_{JJ'} \delta_{MM'} \frac{\langle l_3 l_4 L || \mathbf{T}^{(0)} || l_1 l_2 L \rangle}{\sqrt{2L+1}} \frac{\langle S || \mathbf{I}^{(0)} || S \rangle}{\sqrt{2S+1}} \tag{2.26}$$

Using eqn (2.13), the orbital angular momentum element can be rewritten as shown

in eqn (2.27).

$$\langle l_3 l_4 L || \mathbf{T}^{(0)} || l_1 l_2 L \rangle = \langle l_3 l_4 L || \mathbf{C}^{(k)}(\Omega_1) \cdot \mathbf{C}^{(k)}(\Omega_2) || l_1 l_2 L \rangle \tag{2.27}$$

Using the Wigner-Eckhart theorem and eqn (2.23), this can be returned to the non-reduced form.

$$\langle l_3 l_4 L || \mathbf{T}^{(0)} || l_1 l_2 L \rangle = \sqrt{2L+1} \langle l_3 l_4 L M_L | \mathbf{C}^{(k)}(\Omega_1) \cdot \mathbf{C}^{(k)}(\Omega_2) | l_1 l_2 L M_L \rangle \tag{2.28}$$

Then, in the same manner as eqn (2.15), the individual orbital angular momentum can be decoupled from each other and we can move from the $l_1 l_2 L M_L$ scheme to the $l_1 m_1 l_2 m_2$ scheme in eqn (2.29).

$$\langle l_3 l_4 L M_L | \mathbf{C}^{(k)}(\Omega_1) \cdot \mathbf{C}^{(k)}(\Omega_2) | l_1 l_2 L M_L \rangle =$$
$$\sum_{m_1 m_2 m_3 m_4} (L M_L | l_3 m_3 l_4 m_4)(l_1 m_1 l_2 m_2 | L M_L) \tag{2.29}$$
$$\times \langle l_3 m_3 l_4 m_4 | \mathbf{C}^{(k)}(\Omega_1) \cdot \mathbf{C}^{(k)}(\Omega_2) | l_1 m_1 l_2 m_2 \rangle$$

The tensor dot product, eqn (2.10) can be used, with the fact that the first $\mathbf{C}^{(k)}$ only acts on the first electron and that the second $\mathbf{C}^{(k)}$ only acts on the second electron, to separate the equation into two parts:

$$\langle l_3 l_4 L M_L | \left[\mathbf{C}^{(k)}(\Omega_1) \cdot \mathbf{C}^{(k)}(\Omega_2) \right]_0^{(0)} | l_1 l_2 L M_L \rangle =$$
$$\sum_{\substack{m_1 m_2 \\ m_3 m_4 q}} (-1)^q (L M_L | l_3 m_3 l_4 m_4)(l_1 m_1 l_2 m_2 | L M_L) \langle l_3 m_3 | C_q^{(k)} | l_1 m_1 \rangle \langle l_4 m_4 | C_{-q}^{(k)} | l_2 m_2 \rangle$$
$$\tag{2.30}$$

Using the Wigner-Eckhart equation, eqn (2.22), we can express the terms $\langle l_3 m_3 | C_q^{(k)} | l_1 m_1 \rangle$ and $\langle l_4 m_4 | C_{-q}^{(k)} | l_2 m_2 \rangle$ in terms of their reduced matrix elements.

We then use the symmetry properties of the CG coefficients [60] to simplify these expressions.

$$\langle l_3 m_3 | C_q^{(k)} | l_1 m_1 \rangle = \frac{(l_1 m_1 kq | l_3 m_3)}{\sqrt{2l_3+1}} \langle l_3 || C^{(k)} || l_1 \rangle$$

$$\langle l_4 m_4 | C_{-q}^{(k)} | l_2 m_2 \rangle = \frac{(l_2 m_2 k(-q) | l_4 m_4)}{\sqrt{2l_4+1}} \langle l_4 || C^{(k)} || l_2 \rangle \tag{2.31}$$

$$= (-1)^{k+q} \frac{(kq l_4 m_4 | l_2 m_2)}{\sqrt{2l_2+1}} \langle l_4 || C^{(k)} || l_2 \rangle$$

Substituting expressions from eqn (2.31) into eqn (2.30) yields eqn (2.32), cancelling out the $(-1)^{2q}$ as q is an integer.

$$\langle l_3 l_4 L M_L | \mathbf{C}^{(k)}(\Omega_1) \cdot \mathbf{C}^{(k)}(\Omega_2) | l_1 l_2 L M_L \rangle =$$

$$\sum_{\substack{m_1 m_2 \\ m_3 m_4 q}} \frac{(-1)^k}{\sqrt{(2l_3+1)(2l_2+1)}} (L M_L | l_3 m_3 l_4 m_4)(l_1 m_1 l_2 m_2 | L M_L) \tag{2.32}$$

$$\times (l_1 m_1 kq | l_3 m_3)(kq l_4 m_4 | l_2 m_2) \langle l_3 || C^{(k)} || l_1 \rangle \langle l_4 || C^{(k)} || l_2 \rangle$$

Using the expression for the 6-j symbol [60],

$$\begin{Bmatrix} l_3 & l_4 & L \\ l_2 & l_1 & k \end{Bmatrix} = \frac{(-1)^{L+k+l_1+l_4}}{\sqrt{(2l_3+1)(2l_2+1)}} \tag{2.33}$$

$$\times \sum_{\substack{m_1 m_2 \\ m_3 m_4 q}} (l_1 m_1 kq | l_3 m_3)(l_3 m_3 l_4 m_4 | L M_L)(kq l_4 m_4 | l_2 m_2)(l_1 m_1 l_2 m_2 | L M_L),$$

we can rewrite eqn (2.32) as eqn (2.34) using the restriction that L, l_1 and l_4 always have integer values to change $(-1)^{-(L+l_1+l_4)}$ to $(-1)^{L+l_1+l_4}$.

$$\langle l_3 l_4 L M_L | \left[\mathbf{C}^{(k)}(\Omega_1) \cdot \mathbf{C}^{(k)}(\Omega_2) \right]_0^{(0)} | l_1 l_2 L M_L \rangle$$

$$= (-1)^{L+l_1+l_4} \begin{Bmatrix} l_3 & l_4 & L \\ l_2 & l_1 & k \end{Bmatrix} \langle l_3 || C^{(k)} || l_1 \rangle \langle l_4 || C^{(k)} || l_2 \rangle \tag{2.34}$$

This means the direct portion of the matrix element, from eqn (2.11), can be written in full as eqn (2.35), with $R^k(1,2,3,4)$ used as shorthand for $R^k(n_1l_1, n_2l_2, n_3l_3, \varepsilon l_4)$:

$$
\begin{aligned}
\mathcal{M}_{direct} = {} & \delta_{JJ'}\delta_{MM'}\delta_{LL'}\delta_{SS'}(-1)^{L+l_1+l_4} \\
& \times \sum_k R^k(1,2,3,4) \begin{Bmatrix} l_3 & l_4 & L \\ l_2 & l_1 & k \end{Bmatrix} \langle l_3||C^{(k)}||l_1\rangle\langle l_4||C^{(k)}||l_2\rangle.
\end{aligned}
\tag{2.35}
$$

The reduced matrix elements can be calculated using eqn (2.36) to write them in terms of CG coefficients [60].

$$
\langle l||C^{(k)}||l'\rangle = \sqrt{2l'+1}(l'0, k0|l0)
\tag{2.36}
$$

2.2.3.3 Exchange interaction

In the derivation above, we used the fact that the first $C^{(k)}$ acts only on the first orbital and the second $C^{(k)}$ acts only on the second orbital. This is the not the case for the exchange interaction in eqn (2.7). In the exchange interaction, we will need to rearrange the orbitals such that they are in the same order in both the bra and the ket. To do this, we first decouple L and S as follows:

$$
\Psi(n_1l_1n_2l_2LSJM|21) = \sum_{M_L M_S} (LM_L, SM_S|JM)\Psi(n_1l_1n_2l_2LM_LSM_S|21).
\tag{2.37}
$$

We then decouple the individual orbital angular momenta,

$$
\begin{aligned}
\Psi(n_1l_1n_2l_2LSJM|21) = {} & \sum_{M_L M_S m_1 m_2} (LM_L, SM_S|JM)(l_1m_1, l_2m_2|LM_L) \\
& \times \Psi(n_1l_1m_1n_2l_2m_2SM_S|21),
\end{aligned}
\tag{2.38}
$$

and the individual spins:

$$\Psi(n_1 l_1 n_2 l_2 LSJM | 21) = \sum_{M_L M_S m_1 m_2 \mu_1 \mu_2} (LM_L, SM_S | JM)(l_1 m_1, l_2 m_2 | LM_L)$$
$$\times (s_1 \mu_1, s_2 \mu_2 | SM_S) \Psi(n_1 l_1 m_1 s_1 \mu_1 n_2 l_2 m_2 s_2 \mu_2 | 21). \tag{2.39}$$

Here, s_1 and s_2 refer to the individual spins, which for electrons are equal to $\frac{1}{2}$, μ_1 and μ_2 refer to the projection of these spins.

$$\Psi(n_1 l_1 n_2 l_2 LSJM | 21) = \sum_{M_L M_S m_1 m_2 \mu_1 \mu_2} (LM_L, SM_S | JM)(l_1 m_1, l_2 m_2 | LM_L)$$
$$\times (s_1 \mu_1, s_2 \mu_2 | SM_S) \phi(n_1 l_1 m_1 s_1 \mu_1 | 2) \phi(n_2 l_2 m_2 s_2 \mu_2 | 1). \tag{2.40}$$

Following eqn (2.39), we have used the fact that the two orbitals are entirely decoupled to write the two electron wavefunction as the product of two one electron wavefunctions in eqn (2.40). We rewrite this using the interchange properties of the Clebsch-Gordan coefficients [63] in eqn (2.41):

$$\Psi(n_1 l_1 n_2 l_2 LSJM | 21) = (-1)^{L-l_1-l_2}(-1)^{S-1/2-1/2} \sum_{M_L M_S m_1 m_2 \mu_1 \mu_2} (LM_L, SM_S | JM)$$
$$\times (l_2 m_2, l_1 m_1 | LM_L)(\tfrac{1}{2}\mu_2, \tfrac{1}{2}\mu_1 | SM_S) \phi(n_1 l_1 m_1 s_1 \mu_1 | 2) \phi(n_2 l_2 m_2 s_2 \mu_2 | 1). \tag{2.41}$$

The electrons are still in the same orbitals, but the coupling ordering is swapped from $l_1 l_2$ to $l_2 l_1$. Following this, we swap the $n_1 l_1 m_1 s_1 \mu_1$ labels and the $n_2 l_2 m_2 s_2 \mu_2$ labels. This expression allows us to write Ψ in the reordered form:

$$\Psi(n_1 l_1 n_2 l_2 LSJM | 21) = (-1)^{L-l_1-l_2+S-1}\Psi(n_2 l_2 n_1 l_1 LSJM | 12) \tag{2.42}$$

We can now express the exchange interaction contribution:

$$
- \langle \Psi(\gamma|12)| \frac{1}{r_{12}} |\Psi(\gamma'|21)\rangle = (-1)^{L-l_1-l_2+S}
$$
$$
\times \sum_k \langle \Psi(n_3 l_3 n_4 l_4 L'S'J'M'|12)| \frac{r_<^k}{r_>^{k+1}} \mathbf{C}^{(k)}(\Omega_1) \cdot \mathbf{C}^{(k)}(\Omega_2) |\Psi(n_2 l_2 n_1 l_1 LSJM|12)\rangle
$$
$$(2.43)$$

As in eqn (2.11), the expression in eqn (2.43) can be split into radial and angular components as shown in eqn (2.44).

$$
- \langle \Psi(\gamma|12)| \frac{1}{r_{12}} |\Psi(\gamma'|21)\rangle
$$
$$
= (-1)^{L-l_1-l_2+S} \sum_k R^k(2,1,3,4) \langle l_3 l_4 L'S'J'M'| \mathbf{C}^{(k)}(\Omega_1) \cdot \mathbf{C}^{(k)}(\Omega_2) |l_2 l_1 LSJM\rangle
$$
$$(2.44)$$

Removing the spin dependence as in eqn (2.14) and eqn (2.28), we obtain

$$
- \langle \Psi(\gamma|12)| \frac{1}{r_{12}} |\Psi(\gamma'|21)\rangle
$$
$$
= (-1)^{L-l_1-l_2+S} \delta_{MM'} \delta_{JJ'} \delta_{LL'} \delta_{SS'}
$$
$$
\times \sum_k (-1)^{L+l_4+l_2} \begin{Bmatrix} l_3 & l_4 & L \\ l_1 & l_2 & k \end{Bmatrix} \langle l_3||C^{(k)}||l_2\rangle \langle l_4||C^{(k)}||l_1\rangle R^k(2,1,3,4).
$$
$$(2.45)$$

We add the direct and exchange interaction terms to obtain an expression for the

matrix element.

$$\mathcal{M} = (-1)^{L+l_1+l_4} \sum_k \left[R^k(1,2,3,4) \begin{Bmatrix} l_3 & l_4 & L \\ l_2 & l_1 & k \end{Bmatrix} \langle l_3 ||C^{(k)}||l_1\rangle \langle l_4 ||C^{(k)}||l_2\rangle \right.$$

$$\left. +(-1)^{L+S} R^k(2,1,3,4) \begin{Bmatrix} l_3 & l_4 & L \\ l_1 & l_2 & k \end{Bmatrix} \langle l_3 ||C^{(k)}||l_2\rangle \langle l_4 ||C^{(k)}||l_1\rangle \right] \delta_{MM'}\delta_{JJ'}\delta_{LL'}\delta_{SS'}$$

$$(2.46)$$

2.3 Atomic orbitals

2.3.1 Continuum atomic orbtials

2.3.1.1 Hartree-Fock-Slater equations

To calculate Auger rates, we must first obtain the continuum orbital wavefunction for the emitted electron in the Auger transition. To calculate this wavefunction, we solve the Hartree-Fock (HF) equation [64];

$$\underbrace{-\frac{1}{2}\nabla^2 \phi_\varepsilon(\mathbf{r})}_{\text{Kinetic energy}} - \underbrace{\frac{Z}{|\mathbf{r}|}\phi_\varepsilon(\mathbf{r})}_{\text{Electron-nuclei}} + \underbrace{\sum_i^{\text{orb.}} a_i \int d\mathbf{r}' \frac{\phi_i^*(\mathbf{r}')\phi_i(\mathbf{r}')}{|\mathbf{r}-\mathbf{r}'|}\phi_\varepsilon(\mathbf{r})}_{\text{Direct interaction}}$$

$$\underbrace{-\sum_i^{\text{orb.}} b_i \int d\mathbf{r}' \frac{\phi_i^*(\mathbf{r}')\phi_\varepsilon(\mathbf{r}')}{|\mathbf{r}-\mathbf{r}'|}\phi_i(\mathbf{r})}_{\text{Exchange interaction}} = \varepsilon\phi_\varepsilon(\mathbf{r}).$$

$$(2.47)$$

Here $\mathbf{r}$ is the position of the continuum electron relative to the nucleus, ϕ_ε is the continuum orbital wavefunction and ε is the energy of the electron in the continuum. Z is the charge of the nucleus and ϕ_i is the wavefunction of the bound orbital i. a_i and b_i are coefficients with a_i corresponding to the number of electrons in this orbital. b_i is the coefficient of the exchange interaction and its values are calculated

in Appendix B. The contribution of the direct interaction can be written as

$$\sum_i^{orb.} a_i \int d\mathbf{r}' \frac{\phi_i^*(\mathbf{r}')\phi_i(\mathbf{r}')}{|\mathbf{r}-\mathbf{r}'|}\phi_\varepsilon(\mathbf{r}) = \int \rho(\mathbf{r}')\frac{1}{|\mathbf{r}-\mathbf{r}'|}d\mathbf{r}', \tag{2.48}$$

where $\rho(\mathbf{r}') = \phi_i^*(\mathbf{r}')\phi_i(\mathbf{r}')$ is the electron density.

We can simplify the exchange term of eqn (2.47) using the Hartree-Fock-Slater (HFS) method [65]. In this method, we make the free-electron exchange approximation [66]; the average exchange potential of our non-uniform system at $\mathbf{r}$ is approximated to be equal to the exchange potential for a free-electron gas with equal charge density at point $\mathbf{r}$. This method provides a much simpler form of the exchange potential, given below.

$$V^{exch}(\mathbf{r}) = -3\left[\frac{3}{8\pi}|\rho(\mathbf{r})|\right]^{\frac{1}{3}}. \tag{2.49}$$

We also use the central field approximation, in which we assume that all orbital wavefunctions are solutions of a spherically-averaged potential. Using this, we obtain the radial Hartree-Fock-Slater (HFS) equation.

$$\left[-\frac{1}{2}\frac{d^2}{dr^2} + \frac{1}{2}\frac{l(l+1)}{r^2} + V^{HFS}(r)\right]P_{\varepsilon l}(r) = \varepsilon P_{\varepsilon l}(r). \tag{2.50}$$

Where $P_{\varepsilon l}$ is the radial component of the atomic continuum orbital, such that the continuum orbital $\phi_{\varepsilon lm}(r,\theta,\phi) = \frac{1}{r}P_{\varepsilon l}(r)Y_{lm}(\theta,\phi)$. V^{HFS} is the HFS one-electron potential and at small distances from the nucleus $V^{HFS}(r) = V_0^{HFS}(r)$.

$$V_0^{HFS}(r) = -\frac{Z}{r} - \frac{1}{r}\int_0^r \sigma(t)dt - \int_r^\infty \frac{\sigma(t)}{t}dt - 3\left[\frac{3}{8\pi}|\rho(\mathbf{r})|\right]^{\frac{1}{3}}. \tag{2.51}$$

Here, $\sigma(r) = 4\pi r^2\rho(r)$ is the spherically-averaged charge density at radius r. At

large distances, the free-electron exchange approximation is inaccurate. Therefore, we assume that the potential will asymptotically tend to the Coulomb potential of the total charge on the atom. This gives the following expression for V^{HFS}.

$$V(r) = \begin{cases} V_0^{HFS}(r) & r < r_0 \\ -(Z-N+1)/r & r \geq r_0 \end{cases} \tag{2.52}$$

Here N is the initial number of electrons, before the continuum electron is ejected. r_0 is defined as the radius such that $V_0^{HFS}(r_0) = -(Z-N+1)/r_0$. We obtain this potential, using the Herman-Skillman atomic structure code [67, 68]. Once we have the one-electron potential, we can calculate the radial component of the atomic continuum orbital using eqn (2.50), which we solve using the Numerov method.

2.3.1.2 Numerov method

To calculate the wavefunction using the Numerov method, we define an effective nuclear charge, Z^{HFS}, such that

$$V^{HFS}(r) = -\frac{Z^{HFS}(r)}{r}. \tag{2.53}$$

We can then write the radial HFS equation as

$$\left[\frac{d^2}{dr^2} - \frac{l(l+1)}{r^2} + \frac{2Z^{HFS}(r)}{r} + k^2 \right] P_{\varepsilon l}(r) = 0. \tag{2.54}$$

Here, $k = \sqrt{2E}$ corresponds to the momentum of the continuum electron. We find the continuum orbital wavefunction by propagating the solution from $r = 0$ into the asymptotic region and matching the solution to the asymptotic form of the wave-

function [69]

$$P_{\varepsilon l}(r) \xrightarrow[r \to \infty]{} \sqrt{\frac{2}{\pi k}} \sin\left(kr + \frac{(Z-N+1)}{k}\ln(2kr) - \frac{l\pi}{2} + \delta\right), \tag{2.55}$$

where δ is the scattering phase-shift and must be determined. This expression is found by neglecting terms which fall faster than $1/r$ as $r \to \infty$ and solving eqn (2.54). We perform the propagation following the modified Numerov method [70], which gives solutions to second-order differential equations of the form

$$\frac{d^2 P(r)}{dr^2} = W(r)P(r). \tag{2.56}$$

We work in terms of an auxiliary function $z(r)$, given by

$$P(r) = \left[1 - (h^2/12)W(r)\right]z(r). \tag{2.57}$$

This function is then propagated over a grid with step-size h, using a recursive relation obtained via Taylor's expansion

$$z_{i+1} = \left[2 + h^2 W_i\right]z_i - z_{i-1}. \tag{2.58}$$

At grid point r_i, $z_i = z(r_i)$ and $W_i = W(r_i)$, where $i \in \mathbb{Z} : i \in [0, I]$ and I is the total number of points. We set $z_0 = 0$ and $z_1 = 0.01h$ and propagate the wave-function across the grid to an effective asymptotic radius. We then normalise the propagated wavefunction by matching it to the asymptotic wavefunction calculated with eqn (2.55). To obtain the normalisation, we note that

$$\sqrt{A^2 + B^2}\sin(x + \delta) = A\sin(x) + B\cos(x), \qquad \tan(\delta) = B/A, \tag{2.59}$$

where $x = kr + (Z - N + 1)\ln(2kr)/k - l\pi/2$, and equate the final two grid points to $A\sin(x) + B\cos(x)$.

$$A\sin(x_{I-1}) + B\cos(x_{I-1}) = P(x_{I-1}),$$
$$A\sin(x_I) + B\cos(x_I) = P(x_I). \qquad (2.60)$$

Solving these equations simultaneously yields A and B.

$$A = \frac{P(x_{I-1})\cos(x_I) - P(x_I)\cos(x_{I-1})}{\sin(x_{I-1})\cos(x_I) - \sin(x_I)\cos(x_{I-1})}, \qquad (2.61)$$

$$B = \frac{P(x_I)\sin(x_{I-1}) - P(x_{I-1})\sin(x_I)}{\sin(x_{I-1})\cos(x_I) - \sin(x_I)\cos(x_{I-1})}, \qquad (2.62)$$

By matching eqn (2.55) to eqn (2.60), we obtain an expression for the normalisation $\sqrt{2/(\pi k(A^2 + B^2))}$. This gives us the normalised radial wavefunction at all grid points.

2.3.2 Bound atomic orbitals

To calculate Auger rates and the continuum electron wavefunctions, we must obtain the bound orbital wavefunctions. To calculate all of the Auger transition rates and the corresponding continuum wavefunctions, we need the wavefunction of each bound orbital for all electronic configurations of our atom, $(1s^a 2s^b 2p^c 3s^d 3p^e ...)$, and the energies of the configurations. These calculations were performed without accounting for fine structure. In our work, we calculated the atomic bound orbitals using the Hartree-Fock procedure, with Molpro [71], which is a quantum chemistry package.

2.4   Atomic photo-ionisation cross-sections

In order to model the reaction of an atom following an FEL pulse, we need to obtain the photo-ionisation cross-sections as well as the Auger rates. In our calculations, we only consider single-photon, single-electron photo-ionisations and calculate the photo-ionisation cross-section for each energetically accessible transition of this type. To calculate these cross-sections, we used the Los Alamos National Laboratory collection of atomic physics codes [72].

2.5   Rate equations

2.5.1   States

We are interested in the response of an atom to an FEL pulse and the interplay between photo-ionisation and Auger decay. To do this we must construct rate equations that calculate the population in each electronic configuration and how these populations change with time due to photo-ionisation and Auger decay. The Auger rates and photo-ionisation cross-sections are calculated as described in previous sections. We do not include fluorescent transitions as, for the ion states considered, they have much lower widths than the Auger decay and core photo-ionisations [73]. Similarly, for the large photon energies, we considered, multi-photon ionisations had much lower cross-sections than single-photon processes. With this information, we construct the rate equations listed as follows

$$\frac{d}{dt}\mathscr{I}_j^{(q)}(t) = \sum_i (\sigma_{i\to j}J(t) + \Gamma_{i\to j})\mathscr{I}_i^{(q-1)}(t) - \sum_{k'}(\sigma_{j\to k'}J(t) + \Gamma_{j\to k'})\mathscr{I}_j^{(q)}(t),$$

(2.63)

Here $\mathscr{I}_j^{(q)}$ is the population in state j, with charge q, $J(t)$ is the photon flux at time t, $\sigma_{i\to j}$ is the photo-ionisation cross-section for state i to state j and $\Gamma_{i\to j}$ is the Auger rate for state i to state j. States here refer to electronic configurations i.e. ($1s^a 2s^b 2p^c 3s^d 3p^e \dots$). Using these rate equations, we calculate the population of each electronic configuration during the pulse. We account for Auger processes

that occur after the pulse ends, to ensure that the configurations decay to stable states. By summing up all of the configurations of a specific charge, as shown in eqn (2.64), we find the ion yields $\mathscr{I}^{(q)}$ generated by the pulse.

$$\mathscr{I}^{(q)} = \sum_j \mathscr{I}_j^{(q)}(t) \tag{2.64}$$

2.5.2 Pathways

The rate equations give us information about the population in each state, however we are interested in MCH states. These states decay quickly via the Auger process and therefore there will be little population in them at any time. To better understand how these states are formed and decay, we calculate the population for each energetically allowed sequence of transitions, i.e. pathways, using a new set of rate equations. A pathway population is defined as the population that has passed through a series of states and is now in the final state of that series. For example, $\mathscr{I}_{i \to j \to k \to l}^{(q)}(t)$ is the population that has passed through state i, j and k and is now in state l, with charge q, at time t.

To find the all energetically allowed pathways, we start with the neutral atom and add new pathways for each allowed transition from that initial state. We then build up a set of pathways iteratively by taking each existing pathway and adding a new pathway for each allowed transition from the final state of this pathway. We repeat this process until there are no more allowed transitions available for any pathway.

To calculate the pathway populations, we use similar rate equations to those used in section 2.5.1. However, rather than calculating the population transition between different states, we instead consider the population moving between different pathways. These equations are given below:

$$\frac{d}{dt}\mathscr{I}_{i \to j \to k}^{(q)}(t) = (\sigma_{j \to k}J(t) + \Gamma_{j \to k})\mathscr{I}_{i \to j}^{(q-1)}(t) - \sum_l (\sigma_{k \to l}J(t) + \Gamma_{k \to l})\mathscr{I}_{i \to j \to k}^{(q)}(t)$$

$$(2.65)$$

Here $\mathscr{I}^{(q)}_{i \to j \to k}$ is the population in the pathway $i \to j \to k$, where state k has charge q and $\mathscr{I}^{(q-1)}_{i \to j}$ is the population in the pathway $i \to j$, where state j has charge $q - 1$.

Chapter 3

Argon interacting with a free-electron laser

In this section, we explore the interplay of photo-ionisations and Auger transitions in argon interacting with an FEL pulse. Argon was chosen due to the high level of experimental interest in this atom. There have been measurements of the Auger spectra of $2p$ holes [35, 36], $2s$ holes [74] and $1s$ holes [75, 76, 77].

We use the techniques outlined in the previous section to model the interaction of an FEL pulse with atomic argon. We calculate the ion yields and the contribution of different pathways to the ion yields. We explore the effects of combinations of core photo-ionisations (P_C) and Auger decay transitions (A_{VV}) and how the accessibility of core-hole states affects ion yields. We also investigate the impact of Coster-Kronig Auger transitions [57] (A_{CV}) on the ion yields.

3.1 Calculation details

3.1.1 Bound orbital wavefunctions

We investigate the interplay between photo-ionisation and Auger transitions that occur in argon interacting with an FEL pulse. In order to calculate the Auger decay rates for this interaction, we must first obtain the orbital wavefunctions involved. We consider electronic configurations up to Ar^{8+} of the form $(1s^a 2s^b 2p^c 3s^d 3p^e)$, where a,b,c,d and e are integers between 0 and their occupancy in the neutral state $(1s^2 2s^2 2p^6 3s^2 3p^6)$.

As we want to represent a variety of different electronic configurations of argon, we use an expanded [78] basis set. As we will be performing two-electron integrals in eqn (2.12), we choose to use gaussian-type orbitals (GTOs) where wavefunctions are expressed as a combination of gaussians. More GTOs than Slater-type orbitals are required to achieve the same accuracy as Slater-type orbitals, which are of the form $Nr^{n-1}e^{-\zeta r}$ where n is the principal quantum number, N is a normalising factor and ζ is a constant related to the effective charge of the nucleus. However, GTOs are easier to perform integrals with, due to the properties of gaussians [79]. With these basis sets, the orbital wavefunctions are given in terms of contracted gaussian functions, which are formed of primitive gaussian-type orbitals (GTOs). We used Cartesian primitive GTOs [80] centred on the atom, defined as

$$g_i = N x^{l_x} y^{l_y} z^{l_z} e^{-\alpha_i \left(x^2 + y^2 + z^2 \right)} \tag{3.1}$$

where x, y and z are the cartesian coordinates relative to the atom, α is an orbital exponent and l_x, l_y and l_z are non-negative integers. N is the normalisation factor, given by

$$N = \left(\frac{2\alpha}{\pi} \right)^{3/4} \left[\frac{(8\alpha)^{l_x+l_y+l_z} l_x! l_y! l_z!}{(2l_x)!(2l_y)!(2l_z)!} \right]^{1/2}. \tag{3.2}$$

The sum of the l_x, l_y and l_z values determine the type of the GTO. If $l_x + l_y + l_z = 0$, the GTO is an s-type GTO, $l_x + l_y + l_z = 1$ indicates a p-type GTO and $l_x + l_y + l_z = 2$ indicates a d-type GTO. We combine these primitive GTOs to form contracted gaussian functions

$$\xi_j = \sum_i d_{ji} g_i. \tag{3.3}$$

Here, d_{ji} are the contraction coefficients for the contribution of the ith primitive

GTO to the contracted gaussian function ξ_j. These contracted gaussians make up the basis set with which we describe all of the orbital wavefunctions. Using these contracted gaussians, we can express orbital wavefunctions in the form;

$$\Phi_k = \sum_j c_{jk} \xi_j. \tag{3.4}$$

Φ_k is the wavefunction of the kth orbital and c_{jk} is the coefficient for the contribution of the jth contracted gaussian function to this wavefunction.

We used a 6-311G triple-zeta Pople basis set [81] for these calculations. In this basis set [82], the *s* orbital wavefunctions of argon are represented by 6 contracted gaussian functions, formed of 6, 3,1,1,1 and 1 primitive gaussians, respectively. The *p* orbital wavefunctions are represented by 5 contracted gaussian functions, formed of 5,2,1,1 and 1 primitive gaussians, respectively.

3.1.2   Pulse parameters

The photo-ionisation rates, at time t, will depend on the photon flux, $J(t)$. We consider a monochromatic pulse and express the temporal form of the FEL flux with a Gaussian function, which is given, in atomic units, by

$$J(t) = 1.554 \times 10^{-16} \frac{I_0 [\text{W cm}^{-2}]}{\hbar \omega [\text{Hartree}]} \exp\left\{ -4\ln 2 \left(\frac{t}{\tau} \right)^2 \right\}, \tag{3.5}$$

where I_0 is the intensity at $t = 0$, τ is the full-width at half-maximum (FWHM) of the pulse and $\hbar \omega$ is the photon energy. For argon, we choose 4 different photon energies, to allow the creation of 0, 1, 2 or 3 2p inner-shell holes by single-photon ionisations respectively. For argon, these energies are 200 eV, 260 eV, 315 eV and 360 eV, respectively. The pulse duration was chosen to be 10 fs, as a short pulse duration favours the production of DCH states. We also consider a variety of intensities, in order to investigate the dependence of the ion yields on the intensity.

Method	Auger group rates (10^{-4}a.u.)			
	3s3s	3s3p	3p3p	Total
HFS [83]	0.77	12.85	47.90	61.52
HF [84]	0.28	15.74	56.97	72.99
CI [84]	0.47	9.54	54.74	64.75
This Code [33]	0.45	15.60	51.67	67.72

Table 3.1: Auger transitions rates from initial state $1s^2 2s^2 2p^5 3s^2 3p^6$ where the electron filling in the 2p hole in the initial state and the electron escaping to the continuum occupy the nl and $n'l'$ orbitals, denoted as $nln'l'$ in the table, respectively. We list the Auger rates obtained in [83] using the Hartree-Fock-Slater (HFS) method, in [84] using a Hartree-Fock (HF) method, and in [84] using a CI calculation. The rates are given in 10^{-4} a.u.

3.1.3 Auger rates

To test the validity of our Auger rate calculations, we compared them with a variety of existing theoretical calculations [33]. These comparisons are shown in table 3.1. We see that our Auger rates lie between the values calculated with HFS and HF for all transitions. This is expected as we employ the HF method for the bound orbitals and the HFS method for the continuum orbitals. We also compare with Auger rates calculated using a configuration interaction (CI) method. We expect this to be the most accurate, as the configuration interaction method is a post-Hartree-Fock technique, which takes into account the mixing of different electronic configurations.

3.2 Rate Equations

In order to understand the interplay between the single-photon ionisations and Auger transitions that take place during FEL interactions with argon, we use rate equations to model the population change between different electronic configurations. We run these rate equations in the range, $-3\tau \leq t \leq 40\tau$ where the pulse is centred at $t = 0$. The time after the pulse has finished ensures that states decay to stable states, via the Auger process. This allows us to calculate the ion yields produced by an FEL interaction with argon. The ion yields populated by argon interacting with FEL pulses with various intensities, 10 fs duration and 360 eV photons are given below:

As expected, we can see that high intensity pulses produce more higher-
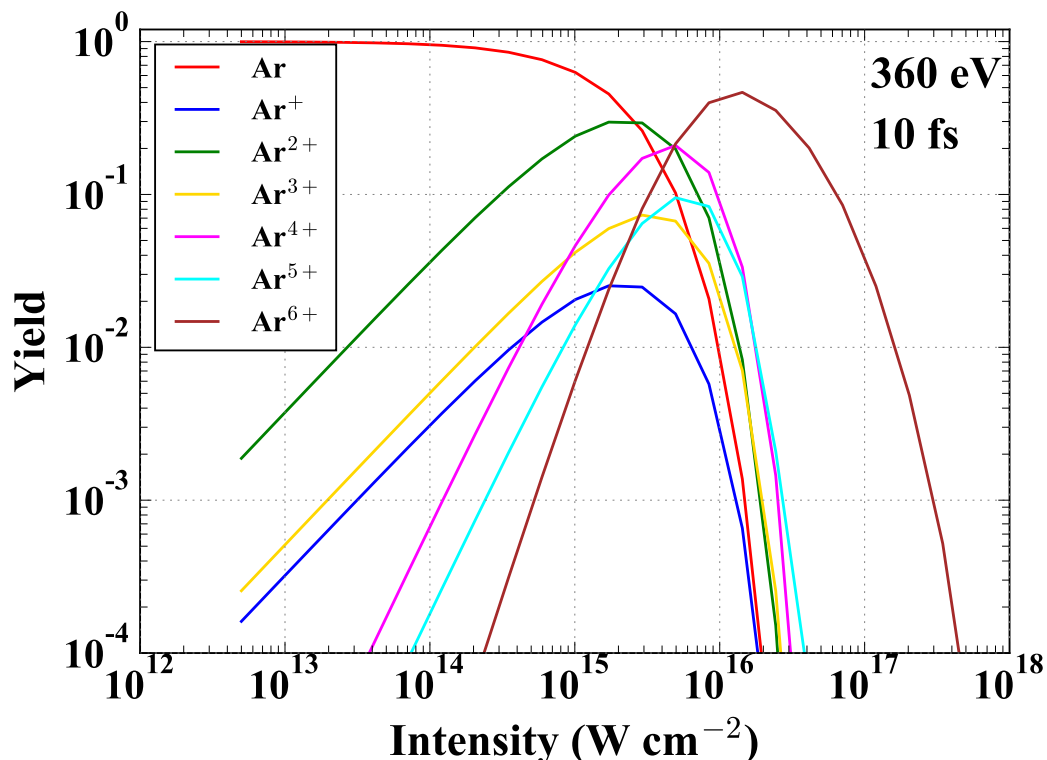
Figure 3.1: Ion yields of Ar^{n+} produced by pulses of different intensity, 10 fs duration and 360 eV photons.

charged ions than low intensity pulses. This is the result of the increased number of photo-ionisation transitions, which will in turn increase the number of Auger transitions. We can also see that the peak yields of the even-charged ions are much higher than the peaks of the odd-charged ions. In order to investigate this difference in yields, we look at the transition pathways that populate these ion yields.

3.3 Pathways

The pathways available in our model depend on the energy of the photons in our pulse, as this energy determines which photo-ionisation transitions can take place. Once we have determined which transitions are allowed, we build up our set of available pathways, as discussed in section 2.5.2. A diagram of the possible transitions for pulses with 315 eV or 360 eV photons is shown below:

We can see, in Fig. 3.2, that the energy level diagram with higher-energy photons has additional accessible states. In Fig 3.2a, we can see two different path-
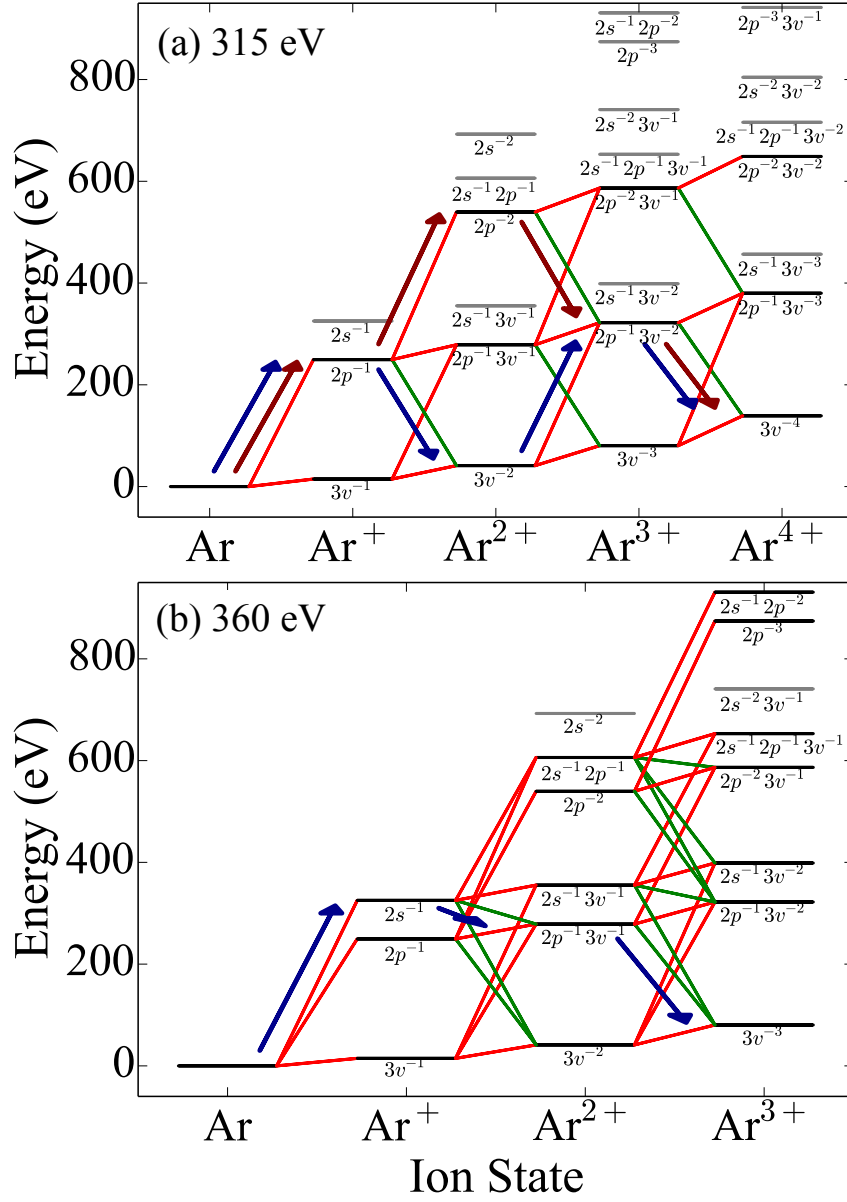
Figure 3.2: Ionisation pathways between different electronic configurations of Ar accessible with *P* (red lines) and *A* (green lines) events (a) up to Ar^{4+} for $\hbar\omega = 315$ eV and (b) up to Ar^{3+} for $\hbar\omega = 360$ eV. Accessible configurations are coloured black, while inaccessible configurations are grey. The labels $2s^{-a}2p^{-b}3v^{-c}$ stand for the electronic configuration ($2s^{2-a}2p^{6-b}3s^{2-d}3p^{6-e}$), with $d + e = c$ the number of valence holes. In (a) $P_C A_{VV} P_C A_{VV}$ (blue arrows) and $P_C P_C A_{VV} A_{VV}$ (brown arrows) are the pathways which contribute the most to the ion yield of Ar^{4+}. In (b) the blue arrows indicate the pathway $P_C A_C A_{VV}$ that involves a Coster-Kronig A_C transition and populates Ar^{3+}.

ways have been illustrated. These are the two pathways which contribute the most population to the Ar^{4+} ion yield. Both of these states involve two P_C transitions and two A_{VV} transitions, these transitions are much more common than valence photo-ionisation (P_V) transitions, so it's expected that these transition pathways will dominate the Ar^{4+} ion yield. However, only the brown pathway, $P_C P_C A_{VV} A_{VV}$, will produce a double-core-hole (DCH) state as the two photo-ionisations occur before an Auger transition fills in the core hole.

In Fig 3.2b, the 360 eV photons allows the photo-ionisation of a $2s$ electron. This introduces Coster-Kronig transitions, which we see in the pathway $P_C A_{CV} A_{VV}$. In the Coster-Kronig transition, a core hole is filled in by an electron from the same shell and a valence electron is ejected. Therefore, these transitions remove a valence electron, while retaining the same number of core holes. This means that there can be a further Auger decay, as we see in the pathway $P_C A_{CV} A_{VV}$. To further investigate the effects of increasing energetically-accessible core photo-ionisations, we calculate the ion yields at a variety of photon energies.
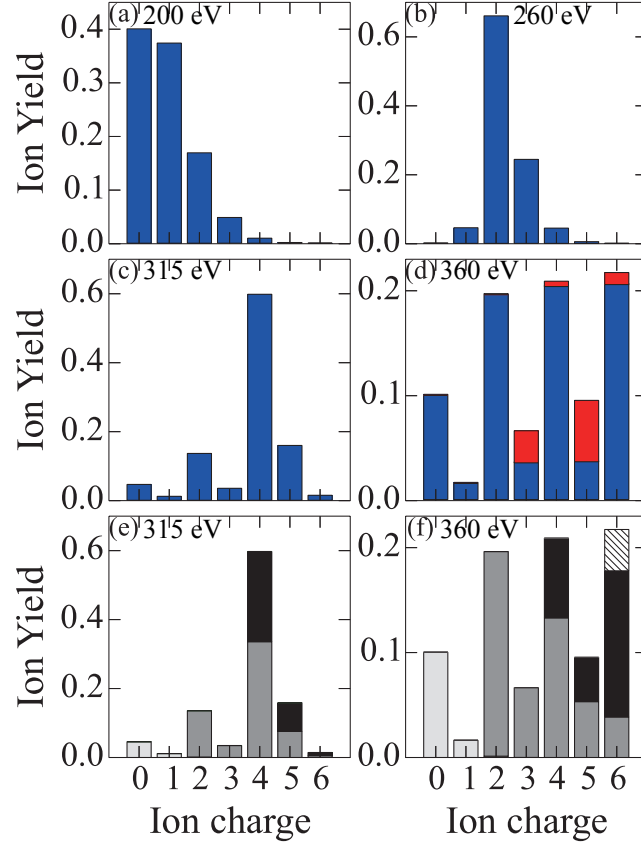
Figure 3.3: Ion yields of Ar^{n+} for a pulse of 5×10^{15} W cm^{-2} intensity, 10 fs duration and different photon energies. For each photon energy, the number of accessible inner-shell holes is different: (a) 200 eV, no inner-shell holes; (b) 260 eV, a single $2p$ inner-shell hole; (c) 315 eV, two $2p$ inner-shell holes. (d) 360 eV, three $2p$ and a combination of two $2p$ and one $2s$ inner-shell holes. Highlighted in red is the contribution of Coster-Kronig Auger transitions. (e) for 315 eV and (f) for 360 eV show the contribution of pathways that are differentiated by the maximum number of core holes in any state along each pathway: light grey corresponds to zero maximum number of core holes, grey to one, black to two and striped black lines to three.

3.4 Ion yields

In Fig. 3.3, we compare the ion yields generated by a 5×10^{15} W cm^{-2} pulse with a duration of 10 fs for a variety of different photon energies. The photon energies were chosen so as to vary the number of energetically accessible core holes.

In Fig. 3.3a, no core holes are available and the ion yields fall with increasing charge. For Fig. 3.3b, the ion yield of Ar^{2+} is the highest. The P_C transition is much more likely than the P_V transition and it is followed by an Auger decay, populating

the Ar^{2+} states. In Fig. 3.3c, two P_C transitions are energetically accessible, as seen in Fig. 3.2a. This leads to a large ion yield of Ar^{4+} due to $P_C P_C A_{VV} V A_{VV}$ and $P_C A_{VV} P_C A_{VV}$ pathways. The ion yield of Ar^{2+} is also higher than the ion yield of Ar^+ for the same reasons as for the 260 eV case. For 360 eV (Fig. 3.3d), there are three accessible P_C transitions, see Fig. 3.2b. The ion yields of Ar^{4+} and Ar^{2+} are higher than Ar^{3+} and Ar^+ as for the lower energies. The ion yields of Ar^{6+} are also higher than Ar^{5+}, due to the contribution of pathways involving three P_C transitions and three A_{VV} transitions.

It can be seen that the ion yields of Ar^{2n+} states are higher than the ion yields of $Ar^{(2n-1)+}$ states where n=1,2,..,h and h is the number of accessible core holes. This is due to the $P_C A_{VV}$ pairs, as the P_C and A_{VV} transitions are much more probable than P_V transitions and P_C transitions create core holes which will decay via A_{VV} transitions. The relation holds at the 360eV photon energy, but the difference between the odd and even charged yields is smaller than in the 315eV case. This is due to the Coster-Kronig transitions which replace a $P_C A_{VV}$ pair with a $P_C A_{CV} A_{VV}$ series of transitions, as shown in Fig. 3.2b. This replacement shifts the pathway from populating even-charged states to populating odd-charged states. Another effect that we notice is that, after core photo-ionisations become energetically accessible (Fig. 3.3 b-d), increasing the photon energy increases the proportion of argon which remains unionised. This effect is due to the increase in photon energy decreasing the photon flux for a given intensity, as shown in eqn (3.5).

While the ion yields in Fig. (3.3a-d) give a lot of information about the transitions that dominate the ion yields and the effects of Coster-Kronig, we are primarily interested in the production of a double core hole state.

The ion yields data doesn't allow us to determine whether a double core hole state was produced as there are multiple pathways that result in Ar^{4+}, as shown in Fig. 3.2a. By calculating the pathway populations we show, in Fig. 3.3e and Fig. 3.3f, the proportion of pathways that pass through multiple-core-hole (MCH) states. We show that less than half of the yield in Ar^{4+} came via a DCH state. To investigate how to maximise the proportion of the population which accesses MCH
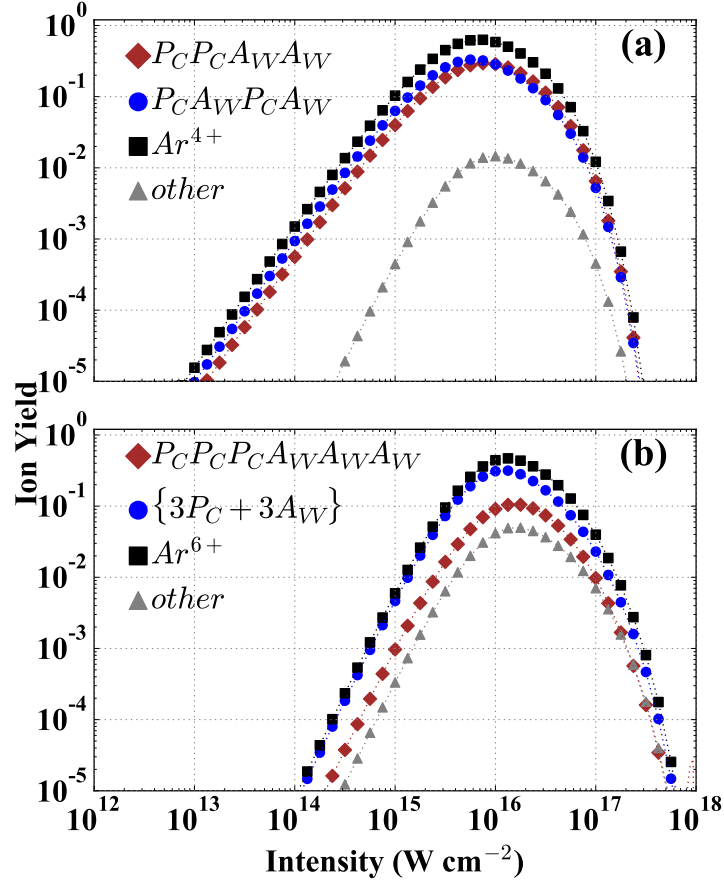
Figure 3.4: As a function of pulse intensity: (a) for 315 eV and 10 fs, the ion yields of Ar^{4+} (black squares), of $P_C A_{VV} P_C A_{VV}$ (blue circles), of $P_C P_C A_{VV} A_{VV}$ (brown diamonds) and of all the other pathways contributing to Ar^{4+} (grey triangles); (b) for 360 eV and 10 fs, the ion yield of Ar^{6+} (black squares), of $P_C P_C P_C A_{VV} A_{VV} A_{VV}$ (brown diamonds), of $\{3P_C + 3A_{VV}\}$ (blue circles) and of all the other pathways contributing to Ar^{6+} (grey triangles).

states, we calculate the pathway populations at a variety of intensities

If we use a pulse with 315 eV photon energy, which can only photo-ionise two $2p$ electrons, see Fig. 3.2a, the only MCH state that can be produced is a DCH state. We are interested in the population of the $P_C P_C A_{VV} A_{VV}$ pathway as it provides evidence of a double core hole state. To see the population that accessed MCH states, the contribution to the ion yields can be split by pathway as shown in Fig. 3.4. In the 315 eV case, Fig. 3.4a, the contribution from the $P_C P_C A_{VV} A_{VV}$ pathway is lower than the contribution from the $P_C A_{VV} P_C A_{VV}$ pathway at low intensity and higher at high intensity. This is to be expected as a high intensity is required for the

second photo-ionisation to be more probable than the Auger decay. In the triple-core-hole (TCH) case, Fig. 3.4b, the $P_C P_C P_C A_{VV} A_{VV} A_{VV}$ pathway corresponds to the formation of a TCH state. This pathway contributes a smaller proportion of the ion yield, compared to the $P_C P_C A_{VV} A_{VV}$ transition in the DCH case. This is due to the increase in the number of different pathways available for the route to Ar^{6+} compared to Ar^{4+}.

These calculations show the proportion of the Ar^{4+} and Ar^{6+} ion yields that access DCH or TCH states, respectively. However, they do not offer any observable quantity that would indicate the formation of a MCH state. In order to show the formation of an MCH state, it would be necessary to calculate the electron spectra produced in an FEL interaction.

3.5 Conclusion

We have explored the interaction of x-ray FELs with atomic argon. The ion yields showed a preferential population of states with even charge for the pulse parameters we considered. We investigated how this preferential population varied with different photon energies. As we allowed the creation of more inner-shell holes, we found that the Ar^{2n} yield was higher than the Ar^{2n-1} yield for $n = 1, ..., h$, where h is the number of core holes available. This effect is evidence of the dominance of core photo-ionisation and Auger decay transitions, as the combination of these two transition types will predominately populate even-charged argon ions. However, if the photon energy is increased, new transitions will become available and the ion yields may no longer follow this pattern.

When the $2s$ electrons become energetically accessibly by the FEL pulse, we find that the difference between odd and even-charged ion yields is reduced. By calculating the pathways by which the ion yields are populated, we obtain information about the the types of transitions that are more likely to populate even-charged or odd-charged ionic states. We note the emergence of the Coster-Kronig Auger transitions when $2s$ electrons become energetically accessible. These A_{CV} transitions add an additional ionisation to the pairs of P_C and A_{VV} and pathways involving these

transitions will predominately populate odd-charged states of argon.

The pathway calculations also allow us to determine the proportion of argon which accesses a MCH state. By calculating the pathways at various intensities, we can see how individual sets of transitions depend on intensity and choose pulse parameters that maximise the production of MCH states. The pathway model we developed was also used to interpret experimental data and understand the dominant pathways at varying intensities [85].

Further investigation could involve whether the preferential population of even-charged ion states continues at higher photon energy, where additional $2s$ photo-ionisations are energetically accessible. It would also be interesting to see if the dependence on the availability of core holes breaks down at longer durations. As the pulse length increases, there is less contribution from MCH states and a single core hole could allow for multiple $P_C A_{VV}$ transitions, if the pulse length is longer than the Auger lifetime.

Chapter 4

Interaction of free-electron laser with molecules

4.1 Introduction

The interaction of molecules with free-electron laser (FEL) radiation is an area of much interest for imaging [9, 10, 11, 12] as well as spectroscopy [13, 14]. As such, there have been several theoretical models which seek to explain experimental observations [23, 41, 42]. Some of these studies have treated the molecule as a combination of independent atoms [23], while others use molecular transition rates calculated with continuum orbitals obtained using Hartree-Fock-Slater methods [41, 42].

In this chapter, we present the theoretical basis behind our model. To investigate molecular FEL interactions, we must consider the interplay of single photon ionisations with Auger transitions and dissociation. We explain how we calculate the photo-ionisation cross-sections and Auger rates in our model and describe how we obtain the molecular continuum wavefunctions without using the Slater exchange potential. This should produce more accurate results, particularly at low energies, where the continuum electron spends more time in the molecular potential.

4.2 Single-centre expansion

In the method we used to calculate the Auger decay rates in atoms, the angular integrals are solved analytically [37]. However, the molecular orbitals do not have

well-defined orbital angular momentum since they are not spherically symmetric. We express the wavefunction in terms of functions with well-defined orbital angular momentum, by performing a single-centre expansion (SCE) [52]. Expressing our wavefunctions in terms of components with well-defined orbital angular momentum allows us to calculate the angular integrals analytically, reducing the computation time. This allows for faster calculations of the continuum wavefunctions, photo-ionisation cross-sections [86, 87] and Auger rates. In the SCE method multi-centred molecular orbitals, $\phi_i(\mathbf{r})$, are expressed as an expansion over spherical harmonics $Y_{lm}(\theta, \phi)$:

$$\phi_i(\mathbf{r}) = \sum_{lm} \frac{P_{i,lm}(r)}{r} Y_{lm}(\theta, \phi), \tag{4.1}$$

where $P_{i,lm}(r)$ is the single-centre coefficient (SCC) of the Y_{lm} component of orbital i. If we project the angular part out of any system of equations describing the single centre wavefunction, we are left with an equation in terms of only $P_{i,lm}(r)$ and one spatial variable, r. We have then reduced a multi-centred problem in three dimensions to that of a single centred problem in a single dimension; the resulting equations describing the single centre coefficients, $P_{i,lm}(r)$, present a much simpler problem to solve.

4.2.1 Molecular Bound Orbitals

To account for Auger and photo-ionisation transitions, we must calculate the Auger rates and photo-ionisation cross-sections. To obtain these values, we must first obtain the molecular orbital wavefunctions. We use Molpro [71] to calculate the wavefunctions of all bound orbitals in each accessible electronic configuration of molecular nitrogen, of the form $1\sigma_g^\alpha 1\sigma_u^\beta 2\sigma_g^\gamma 2\sigma_u^\delta 1\pi_{ux}^\varepsilon 1\pi_{uy}^\zeta 3\sigma_g^\eta$, where $\alpha, \beta, \gamma, \delta, \varepsilon, \zeta, \eta$ are the orbital occupations and have values between 0 and 2.

To calculate the single-centre coefficients of the bound orbitals, $P_{i,lm}(r)$, we multiply the orbital wavefunction $\phi_i(\mathbf{r})$ by $Y_{l'm'}^*(\theta, \phi)$ and integrate over the solid

angle $d\Omega = \sin(\theta)d\theta d\phi$. From eqn (4.1) we obtain

$$\int Y_{l'm'}^*(\theta,\phi)\phi_i(\mathbf{r})d\Omega = \sum_{lm} \frac{P_{i,lm}(r)}{r} \int Y_{l'm'}^*(\theta,\phi)Y_{lm}(\theta,\phi)d\Omega. \tag{4.2}$$

Using the orthonormality of spherical harmonics [60], this can be written as

$$\int Y_{l'm'}^*(\theta,\phi)\phi_i(\mathbf{r})d\Omega = \sum_{lm} \frac{P_{i,lm}(r)}{r} \delta_{ll'} \delta_{mm'}. \tag{4.3}$$

Summing over the delta functions gives us the single-centre coefficients

$$P_{i,l'm'}(r) = r \int Y_{l'm'}^*(\theta,\phi)\phi_i(\mathbf{r})d\Omega. \tag{4.4}$$

4.3   Molecular continuum orbitals

As photo-ionisations and Auger transitions emit electrons, it is necessary to obtain the continuum orbital wavefunctions to calculate the photo-ionisation cross-sections and Auger rates. This is more difficult than the atomic case, as there is no spherical symmetry in the molecular case. The wavefunction of a continuum electron in the presence of a molecular potential can by found by solving the corresponding Hartree-Fock equation [64]:

$$\underbrace{-\frac{1}{2}\nabla^2\phi_\varepsilon(\mathbf{r})}_{\text{Kinetic energy}} + \underbrace{\sum_n^{nuc.} \frac{-Z_n}{|\mathbf{r}-\mathbf{R}_n|}\phi_\varepsilon(\mathbf{r})}_{\text{Electron-nuclei}} + \underbrace{\sum_i^{orb.} a_i \int d\mathbf{r}' \frac{\phi_i^*(\mathbf{r}')\phi_i(\mathbf{r}')}{|\mathbf{r}-\mathbf{r}'|}\phi_\varepsilon(\mathbf{r})}_{\text{Direct interaction}}$$
$$\underbrace{-\sum_i^{orb.} b_i \int d\mathbf{r}' \frac{\phi_i^*(\mathbf{r}')\phi_\varepsilon(\mathbf{r}')}{|\mathbf{r}-\mathbf{r}'|}\phi_i(\mathbf{r})}_{\text{Exchange interaction}} = \varepsilon\phi_\varepsilon(\mathbf{r}). \tag{4.5}$$

ϕ_ε refers to the continuum wavefunction with energy ε, and ϕ_i refers to the wave-

function of the bound orbital *i*. Z_n and $\mathbf{R_n}$ are the charge and position of nucleus n, respectively. a_i and b_i are coefficients associated with the bound orbital *i*, based on the symmetries of the state. These values are derived in Appendix B. The different terms correspond to different interactions between charged particles. The electron-nuclei term is the potential experienced by the continuum electron due to the Coulomb interaction with each of the nuclei. The direct and exchange terms are due to the Coulomb interaction between the continuum electron and the bound electrons. To solve the angular integrals analytically, we express the bound and continuum orbital wavefunctions using a SCE. We then project onto a spherical harmonic, $Y^*_{lm}(\theta, \phi)$, and use the orthonormality of spherical harmonics to obtain:

$$\sum_{l'm'} \left[\left(-\frac{d^2}{dr^2} + \frac{l(l+1)}{r^2} - 2\varepsilon \right) \delta_{ll'}\delta_{mm'} + 2V^{ne}_{lm,l'm'}(r) + 2J^{ee}_{lm,l'm'}(r) \right] P_{\varepsilon,l'm'}(r)$$

$$+ 2X_{lm}[\bar{P}_\varepsilon](r) = 0.$$
$$(4.6)$$

The electron-nuclei interaction $V^{ne}_{lm,l'm'}(r)$ is given by

$$V^{ne}_{lm,l'm'}(r) = \sum_n^{nuc.} -Z_n(-1)^m \sqrt{(2l+1)(2l'+1)}$$

$$\times \sum_{kq} \begin{pmatrix} l & k & l' \\ 0 & 0 & 0 \end{pmatrix} \begin{pmatrix} l & k & l' \\ -m & q & m' \end{pmatrix} \sqrt{\frac{4\pi}{2k+1}} Y^*_{kq}(\theta_n, \phi_n) \frac{r^k_<}{r^{k+1}_>},$$
$$(4.7)$$

where Wigner 3j-symbols [60] have been used to express the angular integrals,

$r_< = \min(r, R_n)$ and $r_> = \max(r, R_n)$. The direct interaction $J_{lm,l'm'}(r)$ is given by

$$
\begin{aligned}
J_{lm,l'm'}(r) = \sum_i a_i \sum_{\substack{l_2 m_2 l_3 m_3 \\ kq}} & \sqrt{(2l+1)(2l'+1)(2l_2+1)(2l_3+1)} \\
\times \begin{pmatrix} l_2 & k & l_3 \\ 0 & 0 & 0 \end{pmatrix} & \begin{pmatrix} l_2 & k & l_3 \\ -m_2 & q & m_3 \end{pmatrix} \begin{pmatrix} l' & k & l \\ 0 & 0 & 0 \end{pmatrix} \begin{pmatrix} l' & k & l \\ -m' & q & m \end{pmatrix} \\
\times (-1)^{m_2+m'} \int_0^\infty & \frac{r_<^k}{r_>^{k+1}} P^*_{i,l_2 m_2}(r') P_{i,l_3 m_3}(r') dr',
\end{aligned}
\tag{4.8}
$$

where $r_< = \min(r, r')$ and $r_> = \max(r, r')$ and, l_2, m_2 and l_3, m_3 refer to the angular momentum components of the orbital i. There are two sets of angular quantum numbers for a single orbital i as it appears in the equation twice and both terms are expressed using the SCE. We are interested in molecular nitrogen, which is a diatomic molecule and therefore has rotational symmetry about the internuclear axis. This rotational symmetry means that the magnetic quantum number, m, is a good quantum number. Therefore, for a given bound orbital i, m_2 and m_3 are equal and have a fixed value determined by the σ or π symmetry of the orbital. This also applies to the continuum orbital and m and m' are equal and determined by the symmetry of the continuum orbital. The exchange interaction can be cast as a functional of the SCE coefficients of the continuum electron orbital as follows

$$
\begin{aligned}
X_{lm}[\bar{P}_\varepsilon](r) = \sum_{l'm'} \sum_i^{orb.} b_i \sum_{\substack{l_2 m_2 l_3 m_3 \\ kq}} & \sqrt{(2l+1)(2l'+1)(2l_2+1)(2l_3+1)} \\
\times \begin{pmatrix} l_2 & k & l' \\ 0 & 0 & 0 \end{pmatrix} & \begin{pmatrix} l_2 & k & l' \\ -m_2 & q & m' \end{pmatrix} \begin{pmatrix} l_3 & k & l \\ 0 & 0 & 0 \end{pmatrix} \begin{pmatrix} l_3 & k & l \\ -m_3 & q & m \end{pmatrix} \\
\times (-1)^{m_2+m_3} \int_0^\infty & \frac{r_<^k}{r_>^{k+1}} P^*_{i,l_2 m_2}(r') P_{\varepsilon l'm'}(r') dr' P_{i,l_3,m_3}(r).
\end{aligned}
\tag{4.9}
$$

These terms are derived and discussed in greater detail in appendix A. To obtain the SCE coefficients of the continuum orbital, we solve eqn (4.6) using a non-iterative

technique [52].

4.4 Non-iterative solution to the Hartree-Fock equation for continuum electrons

The Hartree-Fock equation for continuum electrons can be solved either iteratively or non-iteratively [52]. The iterative method is significantly more computationally intensive, as the integrals which depend on the solution, $P_{\varepsilon,lm}$, must be recalculated for each iteration. The non-iterative technique involves coupling two separate second order differential equations into a single system of second order differential equations. This new system of equations no longer involves a functional of the solution (the exchange term in eqn (4.6)). This means that we no longer have to solve the HF equations iteratively. The method is described below. Initially we define a new function $Y_k(P_1, P_2)$ as,

$$Y_k(P_1, P_2) = r \int \frac{r_<^k}{r_>^{k+1}} P_1^*(r') P_2(r') dr' \qquad (4.10)$$

where P_1 and P_2 can refer to a SCC of a bound or continuum wavefunction. By calculating the second derivative of $Y_k(P_1, P_2)$, we find it satisfies the second order differential equation,

$$\frac{d^2 Y_k(P_1, P_2)}{dr^2} = \frac{k(k+1)}{r^2} Y_k(P_1, P_2) - \frac{(2k+1)}{r} P_1(r) P_2(r). \qquad (4.11)$$

Now consider the exchange term in eqn (4.6), given by eqn (A.14) in section A.3.

Using eqn (4.10), this can now be rewritten,

$$
2X_{lm}[\hat{P}_\varepsilon](r) = 2 \sum_{l'm'} \sum_i^{orb.} b_i \sum_{\substack{l_2 m_2 l_3 m_3 \\ kq}} (-1)^{m_2+m_3} \sqrt{(2l+1)(2l'+1)(2l_2+1)(2l_3+1)}
$$

$$
\times \begin{pmatrix} l_2 & k & l' \\ 0 & 0 & 0 \end{pmatrix} \begin{pmatrix} l_2 & k & l' \\ -m_2 & q & m' \end{pmatrix} \begin{pmatrix} l_3 & k & l \\ 0 & 0 & 0 \end{pmatrix} \begin{pmatrix} l_3 & k & l \\ -m_3 & q & m \end{pmatrix}
$$

$$
\times \frac{Y_k(P_{i,l_2 m_2}, P_{\varepsilon,l'm'})}{r} P_{i,l_3,m_3}(r).
$$

$$(4.12)$$

Defining a new function of the vectors of the bound and continuum SCCs, $\overline{P}_i$ and $\overline{P}_\varepsilon$;

$$
Y_k(\overline{P}_i, \overline{P}_\varepsilon) = \sum_{l'm'} \sum_{l_2 m_2} (-1)^{m_2} \sqrt{(2l'+1)(2l_2+1)}
$$

$$
\times \begin{pmatrix} l_2 & k & l' \\ 0 & 0 & 0 \end{pmatrix} \begin{pmatrix} l_2 & k & l' \\ -m_2 & q & m' \end{pmatrix} Y_k(P_{i,l_2 m_2}, P_{\varepsilon,l'm'}),
$$

$$(4.13)$$

we can now express the exchange term as,

$$
2X_{lm}[\hat{P}_\varepsilon](r) = 2 \sum_i^{orb.} b_i \sum_k \sum_{l_3 m_3} (-1)^{m_3} \sqrt{(2l+1)(2l_3+1)}
$$

$$
\times \begin{pmatrix} l_3 & k & l \\ 0 & 0 & 0 \end{pmatrix} \begin{pmatrix} l_3 & k & l \\ -m_3 & q & m \end{pmatrix} \frac{Y_k(\overline{P}_i, \overline{P}_\varepsilon)}{r} P_{i,l_3,m_3}(r).
$$

$$(4.14)$$

$Y_k(\overline{P}_i, \overline{P}_\varepsilon)$ satisfies the following second order differential equation,

$$\frac{d^2 Y_k(\overline{P}_i, \overline{P}_\varepsilon)}{dr^2} = \frac{k(k+1)}{r^2} Y_k(\overline{P}_i, \overline{P}_\varepsilon) - \frac{(2k+1)}{r} \sum_{l'm'} \sum_{l_2 m_2} \sqrt{(2l_2+1)(2l'+1)}$$
$$\times \begin{pmatrix} l_2 & k & l' \\ 0 & 0 & 0 \end{pmatrix} \begin{pmatrix} l_2 & k & l' \\ -m_2 & q & m' \end{pmatrix} P_{i,l_2 m_2}(r) P_{\varepsilon,l'm'}(r). \tag{4.15}$$

We now couple the original second order differential equation for the continuum wavefunction eqn (4.6) with the second order differential equation for $Y_k(\overline{P}_i, \overline{P}_\varepsilon)$ in a matrix equation,

$$\frac{d^2 \overline{P}}{dr^2} = \hat{M} \overline{P} \tag{4.16}$$

where $\overline{P}$ is the solution vector,

$$\overline{P} = \begin{pmatrix} \{P_{lm}\} \\ \{Y_k(\overline{P}_i, \overline{P}_\varepsilon)\} \end{pmatrix} \tag{4.17}$$

and $\hat{M}$ is block matrix,

$$\hat{M} = \begin{pmatrix} \{M_{lm,l'm'}\} & \{M_{lm,ik}\} \\ \{M_{ik,l'm'}\} & \{M_{ik,i'k'}\} \end{pmatrix}. \tag{4.18}$$

The top-left components of this block matrix, $\{M_{lm,l'm'}\}$, correspond to the non-exchange terms from eqn (4.6)

$$\{M_{lm,l'm'}\} = \left(\frac{l(l+1)}{r^2} - 2\varepsilon \right) \delta_{ll'} \delta_{mm'} + 2V^{ne}_{lm,l'm'}(r) + 2J^{ee}_{lm,l'm'}(r). \tag{4.19}$$

The top-right elements are the multiplicative factors of $Y_k(\bar{P}_i, \bar{P}_\varepsilon)$ from eqn (4.14),

$$
\begin{aligned}
\{M_{lm,ik}\} = \frac{2b_i}{r} \sum_{l_3 m_3} &(-1)^{m_3'} \sqrt{(2l+1)(2l_3+1)} \\
&\times \begin{pmatrix} l_3 & k & l \\ 0 & 0 & 0 \end{pmatrix} \begin{pmatrix} l_3 & k & l \\ -m_3 & q & m \end{pmatrix} P_{i,l_3,m_3}(r).
\end{aligned}
\tag{4.20}
$$

The bottom-left components correspond to the multiplicative factors of $P_{\varepsilon,l'm'}$ from eqn (4.15),

$$
\begin{aligned}
\{M_{ik,l'm'}\} = -\frac{(2k+1)}{r} \sum_{l_2 m_2} &(-1)^{m_2} \sqrt{(2l_2+1)(2l'+1)} \\
&\times \begin{pmatrix} l_2 & k & l' \\ 0 & 0 & 0 \end{pmatrix} \begin{pmatrix} l_2 & k & l' \\ -m_2 & q & m' \end{pmatrix} P_{i,l_2,m_2}(r).
\end{aligned}
\tag{4.21}
$$

Finally, the bottom-right terms are the multiplicative factors of $Y_k(\bar{P}_i, \bar{P}_\varepsilon)$ from eqn (4.15),

$$
\{M_{ik,i'k'}\} = \frac{k(k+1)}{r^2} \delta_{kk'} \delta_{ii'}.
\tag{4.22}
$$

By writing out the matrix equation, eqn (4.16), in full it is clear that we now have a coupled set of equations which we can solve to find $\bar{P}$.

4.4.1 Integration grid

There are two situations in which the Hartree-Fock equation, eqn (4.6), becomes singular; when $r = 0$ for $l \neq 0$, and at the positions of the nuclei, where the electron-nuclei attraction term becomes singular eqn (A.1). Thus, an equidistant grid of r could result in numerical errors at these points. Therefore, as suggested by De-

mekhin [52], the grid of r is mapped on to a new variable ρ by the transformation,

$$\rho(r) = \alpha r + \beta \ln r + \sum_{i}^{\text{nuc.}} \arctan \frac{R_i - r}{\gamma_i}, \tag{4.23}$$

where α, β and γ_i are positive constants which are determined by trial and error on a case-by-case basis. For this work on molecular nitrogen, the values, $\alpha = 0.2$, $\beta = 0.88$ and $\gamma_i = -0.58$ were used. The grid of ρ results in a higher density of points r when $r \to 0$ and at the positions of the nuclei. The grid of $\rho(r)$ is discretised as,

$$\rho_n = \rho_0 + nh, \tag{4.24}$$

where h is the step size. The transformation from r to $\rho(r)$ results in a new solution normalised in space $F_{lm}(\rho)$ [52, 88] which is given by

$$F_{lm}(\rho) = \sqrt{\frac{d\rho(r)}{dr}} P_{lm}(r) = \sqrt{\rho'} P_{lm}(r). \tag{4.25}$$

Introducing this transformation into eqn (4.6) results in the following expression,

$$\frac{d^2 F_{\varepsilon,lm}(\rho)}{d\rho^2} = \frac{1}{(\rho')^2} \sum_{l'm'} \left[\left(\frac{l(l+1)}{r^2(\rho)} - 2\varepsilon \right) \delta_{ll'} \delta_{mm'} + 2V_{lm,l'm'}^{ne}(r(\rho)) \right.$$
$$\left. + 2J_{lm,l'm'}^{ee}(r(\rho)) + \left\{ \frac{1}{2} \frac{\rho'''}{\rho'} - \frac{3}{4} \frac{(\rho'')^2}{(\rho')^2} \right\} \delta_{ll'} \delta_{mm'} \right] F_{\varepsilon,l'm'}(\rho) + \frac{1}{(\rho')^2} 2X_{lm}[\bar{F}_{\varepsilon}](\rho). \tag{4.26}$$

We define the function $Y_k(\bar{P}_i, \bar{F}_{\varepsilon})$ as

$$Y_k(\bar{P}_i, \bar{F}_{\varepsilon}) = \sqrt{\rho'} Y_k(\bar{P}_i, \bar{P}_{\varepsilon}). \tag{4.27}$$

Differentiating this twice and using eqn (4.15) results in

$$
\begin{aligned}
\frac{d^2 Y_k(\overline{P}_i, \overline{F}_\varepsilon)}{d\rho^2} = \frac{1}{(\rho')^2} \Bigg[& Y_k(\overline{P}_i, \overline{F}_\varepsilon) \left\{ \frac{k(k+1)}{r^2(\rho)} + \frac{1}{2} \frac{\rho'''}{\rho'} - \frac{3}{4} \frac{(\rho'')^2}{(\rho')^2} \right\} \\
& - \frac{(2k+1)}{r(\rho)} \sum_{l'm'} \sum_{l_2 m_2} (-1)^{m_2} \sqrt{(2l_2+1)(2l'+1)} \\
& \begin{pmatrix} l_2 & k & l' \\ 0 & 0 & 0 \end{pmatrix} \begin{pmatrix} l_2 & k & l' \\ -m_2 & q & m' \end{pmatrix} P_{i,l_2 m_2}(r(\rho)) F_{\varepsilon,l'm'}(\rho) \Bigg].
\end{aligned}
\tag{4.28}
$$

We can now write an equivalent second-order differential matrix equation to eqn (4.17) on the ρ-grid,

$$
\frac{d^2 \overline{F}}{d\rho^2} = \hat{M}^\rho \overline{F}.
\tag{4.29}
$$

Here $\overline{F}$ is the solution vector of length $N_{lm} + N_{ik}$, where N_{lm} is the number of l and m combinations in the SCE and N_{ik} is the number of bound orbitals multiplied by the number of k values included in the expansion of the $1/|\mathbf{r} - \mathbf{r}'|$ term. $\overline{F}$ is given by

$$
\overline{F} = \begin{pmatrix} \{F_{lm}\} \\ \{Y_k(\overline{P}_i, \overline{F}_\varepsilon)\} \end{pmatrix},
\tag{4.30}
$$

and $\hat{M}^\rho$ is the block matrix of size $N_{lm} + N_{ik}$

$$
\hat{M}^\rho = \begin{pmatrix} \{M^\rho_{lm,l'm'}\} & \{M^\rho_{lm,ik}\} \\ \{M^\rho_{ik,l'm'}\} & \{M^\rho_{ik,i'k'}\} \end{pmatrix}.
\tag{4.31}
$$

The block matrix elements heights and widths are given by either N_{lm} or N_{ik} for the

indices *lm* and *ik*, respectively. These block matrix elements are:

$$
\begin{aligned}
\{M^{\rho}_{lm,l'm'}\} = \frac{1}{(\rho')^2} &\left[\left(\frac{l(l+1)}{r^2(\rho)} - 2\varepsilon \right) \delta_{ll'} \delta_{mm'} + 2V^{ne}_{lm,l'm'}(r(\rho)) \right. \\
&\left. + 2J^{ee}_{lm,l'm'}(r(\rho)) + \left\{ \frac{1}{2} \frac{\rho'''}{\rho'} - \frac{3}{4} \frac{(\rho'')^2}{(\rho')^2} \right\} \delta_{ll'} \delta_{mm'} \right],
\end{aligned}
\tag{4.32}
$$

$$
\begin{aligned}
\{M^{\rho}_{lm,ik}\} = \frac{1}{(\rho')^2} \frac{2b_i}{r(\rho)} &\sum_{l_3 m_3} (-1)^{m_3{}'} \sqrt{(2l+1)(2l_3+1)} \\
&\times \begin{pmatrix} l_3 & k & l \\ 0 & 0 & 0 \end{pmatrix} \begin{pmatrix} l_3 & k & l \\ -m_3 & q & m \end{pmatrix} P_{i,l_3,m_3}(r),
\end{aligned}
\tag{4.33}
$$

$$
\begin{aligned}
\{M^{\rho}_{ik,l'm'}\} = -\frac{1}{(\rho')^2} \frac{(2k+1)}{r(\rho)} &\sum_{l_2 m_2} (-1)^{m_2} \sqrt{(2l_2+1)(2l'+1)} \\
&\times \begin{pmatrix} l_2 & k & l' \\ 0 & 0 & 0 \end{pmatrix} \begin{pmatrix} l_2 & k & l' \\ -m_2 & q & m' \end{pmatrix} P_{i,l_2,m_2}(r),
\end{aligned}
\tag{4.34}
$$

and

$$
\{M^{\rho}_{ik,i'k'}\} = \frac{1}{(\rho')^2} \left\{ \frac{k(k+1)}{r^2(\rho)} + \frac{1}{2} \frac{\rho'''}{\rho'} - \frac{3}{4} \frac{(\rho'')^2}{(\rho')^2} \right\} \delta_{kk'} \delta_{ii'}.
\tag{4.35}
$$

Eqn (4.29) can then be solved for $F_{\varepsilon,l'm'}(\rho)$ on the grid ρ via the Numerov method.

4.4.2 Finding $\bar{F}$ using the Numerov method and Thomas algorithm

The Numerov method can be used to efficiently solve a second-order differential equation such as eqn (4.29) which does not include the first derivative of the desired

function. For an inhomogeneous equation with the form

$$y''(r) = f(r)y(r), \tag{4.36}$$

the solution can be found by propagation of the equation [89],

$$\left(1 - \frac{h^2}{12}f_{n+1}\right)y_{n+1} - \left(2 + \frac{10h^2}{12}f_n\right)y_n + \left(1 - \frac{h^2}{12}f_{n-1}\right)y_{n-1} = 0, \tag{4.37}$$

with appropriate boundary conditions, where $f_n = f(nh)$ for a grid of size N, with $n = 1, \ldots, N-1, N$ and h the radial step size. Applying this to eqn (4.29) we get the following expression,

$$\hat{a}_{n-1}\hat{F}_{n-1} - \hat{b}_n\hat{F}_n + \hat{a}_{n+1}\bar{F}_{n+1} = 0. \tag{4.38}$$

where matrices $\hat{a}$ and $\hat{b}$ are given by,

$$\hat{a}_n = \mathbb{1} - \frac{h^2}{12}\hat{M}_n^\rho \tag{4.39}$$

$$\hat{b}_n = 2\mathbb{1} + \frac{10h^2}{12}\hat{M}_n^\rho \tag{4.40}$$

where $\mathbb{1}$ is the identity matrix of size $N_{lm} + N_{ik}$. This can be written in the form of

a tridiagonal matrix:

$$
\begin{pmatrix}
-\hat{b}_1 & \hat{a}_2 & & & \\
\hat{a}_1 & -\hat{b}_2 & \hat{a}_3 & & \\
& & \ddots & & \\
& & \hat{a}_{n-1} & -\hat{b}_n & \hat{a}_{n+1} \\
& & & & \ddots
\end{pmatrix}
\begin{pmatrix}
\bar{F}_1 \\
\bar{F}_2 \\
\vdots \\
\vdots \\
\vdots
\end{pmatrix}
=
\begin{pmatrix}
0 \\
0 \\
\vdots \\
\vdots \\
0
\end{pmatrix}.
\tag{4.41}
$$

The length of the vectors is the size of the grid, N. To solve this equation, we use the Thomas Algorithm [90]. This method involves an outwards sweep from 1 to N, which removes the lower diagonal components, followed by an inwards sweep from N to 1, which gives the solution. We first, define a matrix $\hat{V}_n$ in terms of it's relation between two sequential values of our wavefunction.

$$
\bar{F}_n = \hat{V}_n \bar{F}_{n+1}
\tag{4.42}
$$

This will allow us to calculate $\bar{F}_n$ for all n given an asymptotic value. We can substitute this expression into eqn (4.38) to determine the value of $\hat{V}_n$:

$$
\hat{a}_{n-1}\hat{V}_{n-1}\bar{F}_n - \hat{b}_n\hat{F}_n + \hat{a}_{n+1}\bar{F}_{n+1} = 0,
\tag{4.43}
$$

rearranging this expressions gives

$$
\bar{F}_n = (\hat{b}_n - \hat{a}_{n-1}\hat{V}_{n-1})^{-1}\hat{a}_{n+1}\bar{F}_{n+1},
\tag{4.44}
$$

using eqn (4.42), we obtain an expression for $\hat{V}_n$

$$\hat{V}_n = (\hat{b}_n - \hat{a}_{n-1} \hat{V}_{n-1})^{-1} \hat{a}_{n+1}. \tag{4.45}$$

Using this expression, we can do an outwards sweep from $n = 1$ to find $\hat{V}_n$ at all points in the grid. We can then do an inwards sweep from $n = N$ using eqn (4.42) to find $\bar{F}_n$ at all grid points. However, we first need to find the value of $\hat{V}_1$ in order to use eqn (4.45).

4.4.3 Boundary conditions

There are two sets of boundary conditions, the inner boundary conditions, which describe the behaviour of the system as $r \to 0$, and the outer asymptotic boundary conditions, which describe the behaviour of the solution as $r \to \infty$. The inner boundary conditions give the values of $\hat{V}_1$ and $\hat{V}_2$, such that we can then iterate for all other points on the grid. These boundary conditions are given below [52].

$$\hat{V}_1 = \hat{V}_2 = \hat{V} = (\hat{b}_2 - \hat{a}_1 \hat{V})^{-1} \hat{a}_3. \tag{4.46}$$

This equation is solved recursively, until it converges to a value for $\hat{V}$. Once we have obtained these initial conditions, we can iterate through all points in the grid and find $\hat{V}_n$ at all points on the grid. We then need to find the asymptotic values of $\bar{F}$, such that we can sweep backwards to obtain $\bar{F}$ at all points. The asymptotic values of the wavefunction, on an r-grid are given below [52].

$$P_{lm}^{LM}(r) = \delta_l^L \delta_m^M J_l(r) + R_{lm}^{LM} H_l(r) \ (r \to \infty). \tag{4.47}$$

The superscripts L and M denote the different energy-degenerate solutions, each of which is formed by a combination of P_{lm} functions. J_l and H_l are the energy-normalised regular and irregular Coulomb wavefunctions, respectively [91]. The

regular Coulomb function represents the solution of a point charge. R_{lm}^{LM} is the interaction matrix, which we compute, it expresses the deviation from a point charge solution [87]. R_{lm}^{LM} is generally a Hermitian matrix, however, as we use real spherical harmonics in our SCE, it is a real symmetric matrix. As the solution vector contains $Y_k(\overline{P}_i, \overline{P}_\varepsilon)$ terms, we also include the asymptotic values of these terms [52]

$$Y_k(\overline{P}_i, \overline{P}_\varepsilon) = B_{ik} r^{-k} \ (r \to \infty), \tag{4.48}$$

where B_{ik} is a constant. Thus, the combined asymptotic boundary conditions for a given L, M channel, which represents an energy-degenerate continuum wavefunction, are:

$$\overline{P} = \begin{pmatrix} \{\delta_l^L \delta_m^M J_l(r) + R_{lm}^{LM} H_l(r)\} \\ \{B_{ik} r^{-k}\} \end{pmatrix} \ (r \to \infty). \tag{4.49}$$

To consider all L, M channels simultaneously, we use a solution vector of matrices.

$$\hat{P} = \begin{pmatrix} \hat{J}(r) + \hat{R}\hat{H}(r) \\ \hat{r}(r)\hat{B} \end{pmatrix} \ (r \to \infty), \tag{4.50}$$

here the $\hat{J}(r)$ and $\hat{H}(r)$ are diagonal matrices with dimensions $N_{lm} \times N_{LM}$, $N_{lm} = N_{LM}$ and N_{lm} is the number of different l, m combinations included in the SCE, the diagonal components are $J_l(r)$ and $H_l(r)$, respectively. $\hat{B} = \{B_{ik,LM}\}$ is a matrix of the constants B_{ik}, as defined in eqn (4.48), for each channel L, M with dimension $N_{ik} \times N_{LM}$, where N_{ik} is the number of different i, k combinations included in the calculation. $\hat{r}(r)$ is a diagonal matrix with r^{-k} as the diagonal elements for each bound orbital i, such that the matrix has dimensions $N_{ik} \times N_{ik}$.

Using eqn (4.50) for the Nth and $(N-1)$th points of the ρ grid, we calculate

$\hat{F}$ using eqn (4.25) and use eqn (4.42) to obtain

$$
\sqrt{\rho'_{N-1}} \begin{pmatrix} \hat{J}_{N-1} + \hat{H}_{N-1}\hat{R} \\ \hat{r}_{N-1}\hat{B} \end{pmatrix} = \begin{pmatrix} \{V_{lm,l'm'}\}_{N-1} & \{V_{lm,ik}\}_{N-1} \\ \{V_{ik,l'm'}\}_{N-1} & \{V_{ik,i'k'}\}_{N-1} \end{pmatrix} \sqrt{\rho'_N} \begin{pmatrix} \hat{J}_N + \hat{H}_N\hat{R} \\ \hat{r}_N\hat{B} \end{pmatrix}
$$

$$(4.51)$$

where the block structure of the $\hat{V}$ matrix has been made explicit. The above matrix equation can be written as two separate boundary conditions which are dependent on each other;

$$
\sqrt{\rho'_{N-1}} \left(\hat{J}_{N-1} + \hat{H}_{N-1}\hat{R} \right) = \sqrt{\rho'_N} \left(\{V_{lm,l'm'}\}_{N-1}(\hat{J}_N + \hat{H}_N\hat{R}) + \{V_{lm,ik}\}_{N-1}\hat{r}_N\hat{B} \right),
$$

$$(4.52)$$

$$
\sqrt{\rho'_{N-1}}\hat{r}_{N-1}\hat{B} = \sqrt{\rho'_N} \left(\{V_{ik,l'm'}\}_{N-1}(\hat{J}_N + \hat{H}_N\hat{R}) + \{V_{ik,i'k'}\}_{N-1}\hat{r}_N\hat{B} \right). \quad (4.53)
$$

Rearranging these equations for $\hat{R}$ and $\hat{B}$, we obtain

$$
\hat{R} = \left(\sqrt{\rho'_{N-1}}\hat{H}_{N-1} - \sqrt{\rho'_N}\{V_{lm,l'm'}\}_{N-1}\hat{H}_N \right)^{-1}
$$
$$
\times \left(\sqrt{\rho'_N}\{V_{lm,ik}\}_{N-1}\hat{r}_N\hat{B} + \sqrt{\rho'_N}\{V_{lm,l'm'}\}_{N-1}\hat{J}_N - \sqrt{\rho'_{N-1}}\hat{J}_{N-1} \right),
$$

$$(4.54)$$

$$
\hat{B} = \left(\sqrt{\rho'_{N-1}}\hat{r}_{N-1} - \sqrt{\rho'_N}\{V_{ik,i'k'}\}_{N-1}\hat{r}_N \right)^{-1} \left(\sqrt{\rho'_N}\{V_{ik,l'm'}\}_{N-1} \left(\hat{J}_N + \hat{H}_N\hat{R} \right) \right).
$$

$$(4.55)$$

Substituting 4.55 into 4.54 we find an expression for $\hat{R}$

$$
\hat{R} = \left[\sqrt{\frac{\rho'_{N-1}}{\rho'_N}} \hat{H}_{N-1} - \{V_{lm,l'm'}\}_{N-1}\hat{H}_N \right.
$$
$$
\left. - \{V_{lm,ik}\}_{N-1}\hat{r}_N \left(\sqrt{\frac{\rho'_{N-1}}{\rho'_N}} \hat{r}_{N-1} - \{V_{ik,i'k'}\}_{N-1}\hat{r}_N \right)^{-1} \{V_{ik,l'm'}\}_{N-1}\hat{H}_N \right]^{-1}
$$
$$
\times \left[\{V_{lm,l'm'}\}_{N-1}\hat{J}_N - \sqrt{\frac{\rho'_{N-1}}{\rho'_N}} \hat{J}_{N-1} \right.
$$
$$
\left. + \{V_{lm,ik}\}_{N-1}\hat{r}_N \left(\sqrt{\frac{\rho'_{N-1}}{\rho'_N}} \hat{r}_{N-1} - \{V_{ik,i'k'}\}_{N-1}\hat{r}_N \right)^{-1} \{V_{ik,l'm'}\}_{N-1}\hat{J}_N \right],
$$

(4.56)

and an expression for $\hat{B}$ can be obtained by substituting 4.54 into 4.55,

$$
\hat{B} = \left[\sqrt{\frac{\rho'_{N-1}}{\rho'_N}} \hat{r}_{N-1} - \{V_{ik,i'k'}\}_{N-1}\hat{r}_N \right.
$$
$$
\left. - \{V_{ik,l'm'}\}_{N-1}\hat{H}_N \left(\sqrt{\frac{\rho'_{N-1}}{\rho'_N}} \hat{H}_{N-1} - \{V_{lm,l'm'}\}_{N-1}H_N \right)^{-1} \{V_{lm,ik}\}_{N-1}\hat{r}_N \right]^{-1}
$$
$$
\times \left[\{V_{ik,l'm'}\}_{N-1}\bar{J}_N + \{V_{ik,l'm'}\}_{N-1}\hat{H}_N \left(\sqrt{\frac{\rho'_{N-1}}{\rho'_N}} \hat{H}_{N-1} - \{V_{lm,l'm'}\}_{N-1}\hat{H}_N \right)^{-1} \right.
$$
$$
\left. \times \left(\{V_{lm,l'm'}\}_{N-1}\hat{J}_N - \sqrt{\frac{\rho'_{N-1}}{\rho'_N}} \hat{J}_{N-1} \right) \right].
$$

(4.57)

4.4.4 Back propagation of solution

After $\hat{R}$ and $\hat{B}$ have been found $\overline{F}_N$ can be found by applying the boundary conditions (eqn (4.50)),

$$
\overline{F}_N = \sqrt{\rho'} \begin{pmatrix} \hat{J}_N + \hat{R}\hat{H}_N \\ \hat{r}_N \hat{B} \end{pmatrix}
\tag{4.58}
$$

the solution vector at all other grid points, $\overline{F}_n$, is then found by back substitution from $n = N$ to $n = 0$ using the relation,

$$
\begin{pmatrix} \overline{F}_n \\ \hat{Y}_n \end{pmatrix} = \begin{pmatrix} \{V_{lm,l'm'}\}_n & \{V_{lm,ik}\}_n \\ \{V_{ik,l'm'}\}_n & \{V_{ik,i'k'}\}_n \end{pmatrix} \begin{pmatrix} \overline{F}_{n+1} \\ \hat{Y}_{n+1} \end{pmatrix}.
\tag{4.59}
$$

Once found, $\overline{F}_n$ is transformed to $\hat{P}_n$ using eqn (4.25). In the above equations $\hat{F}_n$ and $\hat{Y}_n$ are matrices; as in subsection 4.4.2, $\hat{P} = P_{lm,LM}$ where the columns correspond to different channels, L, M, and the rows are the individual components, l, m, of these channels. $\hat{Y} = Y_{ik,LM}$, where again the columns correspond to different channels L, M and the rows correspond to the set of values of $Y_k(\overline{P}_i, \overline{F}_\varepsilon)$ for bound orbital i and multipole expansion angular momenta k.

4.4.5 Normalisation

The continuum electron wavefunction is well-defined, which requires that

$$
P_{\varepsilon,lm}(r \rightarrow 0) \rightarrow 0 \quad \text{for all } l, m.
\tag{4.60}
$$

In addition, the continuum wavefunctions are energy normalised such that,

$$
\langle P_\varepsilon^{LM} | P_{\varepsilon'}^{LM} \rangle = \int_0^\infty dr \sum_{lm} P_{\varepsilon,lm}^*(r) P_{\varepsilon',lm}(r) = \delta(\varepsilon - \varepsilon').
\tag{4.61}
$$

We then insert our expression for the asymptotic form of the radial continuum wave-function, eqn (4.49). Generally, $\hat{R}$ is a Hermitian matrix [52]. In our calculations, $\hat{R}$ is a symmetric matrix, as we use real spherical harmonics [87].

$$
\begin{aligned}
\langle P_\varepsilon^{LM}|P_{\varepsilon'}^{L'M'}\rangle &= \int_0^\infty dr \sum_{lm} P_{\varepsilon,lm}^{*LM}(r) P_{\varepsilon',lm}^{L'M'}(r) \\
&= \int_0^\infty dr \sum_{lm} \left(J_{\varepsilon,l}^*(r)\delta_l^L\delta_m^M + H_{\varepsilon,l}^*(r)R_{lm}^{LM} \right) \\
&\quad \times \left(J_{\varepsilon',l}(r)\delta_l^{L'}\delta_m^{M'} + H_{\varepsilon',l}(r)R_{lm}^{L'M'} \right).
\end{aligned}
\tag{4.62}
$$

Due to the orthogonality of the Coulomb functions,

$$
\int_0^\infty dr J_{\varepsilon,l}^*(r) J(r)_{\varepsilon',l} = \delta(\varepsilon - \varepsilon'),
\tag{4.63}
$$

with a similar expression for $H_{\varepsilon,l}(r)$ and

$$
\int_0^\infty dr J_{\varepsilon,l}^*(r) H_{\varepsilon',l}(r) = 0,
\tag{4.64}
$$

one can write eqn (4.62) as,

$$
\langle P_\varepsilon^{LM}|P_{\varepsilon'}^{L'M'}\rangle = \delta(\varepsilon - \varepsilon') \left(\delta_{L'}^L \delta_{M'}^M + \sum_{lm} R_{lm}^{LM} R_{lm}^{L'M'} \right).
\tag{4.65}
$$

Using this equation, we can show that energy-normalised solutions are given by [87]:

$$
\tilde{P}_{\varepsilon,lm}^{LM}(r) = \langle r,l,m|P_\varepsilon^{LM}\rangle = \frac{1}{\sqrt{1+\lambda_{LM}^2}} \sum_{L'M'} U_{L'M'}^{LM} P_{\varepsilon,lm}^{L'M'}(r)
\tag{4.66}
$$

Where $\bar{U}^{LM}$ is an eigenvector of $\hat{R}$ and λ_{LM} is an eigenvalue, such that:

$$\hat{R}\bar{U}^{LM} = \lambda_{LM}\bar{U}^{LM} \tag{4.67}$$

4.5 Molecular photo-ionisation cross-sections

We calculate the molecular photo-ionisation cross-sections for an electron transitioning from a bound molecular orbital ϕ_i to a final continuum molecular orbital ϕ_ε as follows [61].

$$\sigma_{i \to \varepsilon} = \frac{4}{3}\alpha\pi^2\omega N_i \sum_{M=-1,0,1} |D_{i\varepsilon}^M|^2, \tag{4.68}$$

where α is the fine structure constant, N_i is the occupation number of the initial molecular orbital i, ω is the photon energy, and M is the polarization of the photon. In the length gauge, the matrix element $D_{i\varepsilon}^M$ is given by

$$D_{i\varepsilon}^M = \int \phi_i(\mathbf{r})\phi_\varepsilon(\mathbf{r})\sqrt{\frac{4\pi}{3}}rY_{1M}(\theta,\phi)d\mathbf{r}. \tag{4.69}$$

In the single centre expansion formalism eqn (4.69) takes the form

$$D_{i\varepsilon}^M = \sqrt{\frac{4\pi}{3}} \sum_{lm,l'm'} \int_0^\infty dr P_{i,lm}^*(r) r P_{\varepsilon,l'm'}(r) \int d\Omega Y_{lm}^*(\theta,\phi)Y_{l'm'}(\theta,\phi)Y_{1M}(\theta,\phi)$$

$$= \sum_{lm,l'm'} (-1)^m \sqrt{(2l+1)(2l'+1)} \begin{pmatrix} l & l' & 1 \\ 0 & 0 & 0 \end{pmatrix} \begin{pmatrix} l & l' & 1 \\ -m & m' & M \end{pmatrix} \int_0^\infty dr P_{i,lm}^*(r) r P_{\varepsilon,l'm'}(r).$$

$$\tag{4.70}$$

4.6 Molecular Auger rate calculations

To account for the molecular Auger transitions in our model, we must calculate the Auger rates for all accessible electronic configurations. In this section, we outline the equations that we solved and the method by which we derived these equations.

4.6.1 Derivation

In order to find the Auger rate, we start from the expression for the matrix element, given in eqn (2.7). For molecular Auger rates, we choose to work in the $abSM_S$ scheme. In this scheme, two electron wavefunctions are expressed in terms of their orbitals, a and b and their total spin, S and its projection, M_S. Expressing the matrix element, $\mathscr{M}$, in this scheme results in

$$
\begin{aligned}
\mathscr{M} = &\langle \zeta c S' M_S' | 12 | \frac{1}{r_{12}} | baSM_S | 12 \rangle \\
&- \langle \zeta c S' M_S' | 12 | \frac{1}{r_{12}} | baSM_S | 21 \rangle.
\end{aligned}
\tag{4.71}
$$

Here, ζ refers to the emitted continuum electron, c denotes the core hole being filled in and a and b refer to the valence electron orbitals. S and S' are the total spin of the initial and final electrons, respectively, M_S and M_S' are their projections. $|(baSM_S|12)\rangle$ corresponds to a two-electron wavefunction, with the first electron in spatial orbital b and the second electron in spatial orbital a, with magnetic quantum numbers m_b and m_a, respectively and total spin S and spin projection M_S. The first term of eqn (4.71) refers to the direct term, in which the order of the electrons is consistent. The second term refers to the exchange term, in which the order of the electrons has been switched.

We now use the multipole expansion to express the operator $\frac{1}{r_{12}}$ in terms of spherical harmonics about the molecular centre [61],

$$
\frac{1}{r_{12}} = \sum_{kq} \frac{4\pi}{2k+1} \frac{r_<^k}{r_>^{k+1}} Y_{kq}^*(\theta_1, \phi_1) Y_{kq}(\theta_2, \phi_2),
\tag{4.72}
$$

where $r_< = \min(r_1, r_2)$ and $r_> = \max(r_1, r_2)$. Substituting this into eqn (4.71) gives

$$
\mathcal{M} = \sum_{kq} \frac{4\pi}{2k+1} \left(\langle \zeta c S' M'_S | 12 | \frac{r_<^k}{r_>^{k+1}} Y^*_{kq}(\theta_1, \phi_1) Y_{kq}(\theta_2, \phi_2) | ba S M_S | 12 \rangle \right.
$$
$$
\left. - \langle \zeta c S' M'_S | 12 | \frac{r_<^k}{r_>^{k+1}} Y^*_{kq}(\theta_1, \phi_1) Y_{kq}(\theta_2, \phi_2) | ba S M_S | 21 \rangle \right).
$$
(4.73)

The operator acts on each electron individually, we reorder the electrons in the exchange term so that we can separate the two-electron wavefunction into its one-electron components. In order to reorder the wavefunction $|baSM_S|21\rangle$, we first rewrite it in terms of individual spins, with projections μ_a and μ_b, respectively, using eqn (2.15)

$$
|baSM_S|21\rangle = \sum_{\mu_b \mu_a} (\tfrac{1}{2}\mu_b \tfrac{1}{2}\mu_a | SM_S) |ba\mu_b\mu_a|21\rangle.
$$
(4.74)

We then express this as a product of two one-electron wavefunctions,

$$
|baSM_S|21\rangle = \sum_{\mu_b \mu_a} (\tfrac{1}{2}\mu_b \tfrac{1}{2}\mu_a | SM_S) |b\mu_b|2\rangle |a\mu_a|1\rangle,
$$
(4.75)

and use the interchange properties of the Clebsch-Gordan coefficients [60] to obtain

$$
|baSM_S|21\rangle = \sum_{\mu_b \mu_a} (-1)^{S - \frac{1}{2} - \frac{1}{2}} (\tfrac{1}{2}\mu_a \tfrac{1}{2}\mu_b | SM_S) |a\mu_a|1\rangle |b\mu_b|2\rangle.
$$
(4.76)

Comparing this with the expansion of $|abSM_S|12\rangle$,

$$
|abSM_S|12\rangle = \sum_{\mu_a \mu_b} (\tfrac{1}{2}\mu_a \tfrac{1}{2}\mu_b | SM_S) |a\mu_a|1\rangle |b\mu_b|2\rangle,
$$
(4.77)

we obtain

$$|baSM_S|21\rangle = (-1)^{S-\frac{1}{2}-\frac{1}{2}}|abSM_S|12\rangle. \tag{4.78}$$

We can now substitute eqn (4.78) into eqn (4.73) to obtain

$$\mathcal{M} = \sum_{kq} \frac{4\pi}{2k+1} \left(\langle \zeta c S' M_S'|12| \frac{r_<^k}{r_>^{k+1}} Y_{kq}^*(\theta_1, \phi_1) Y_{kq}(\theta_2, \phi_2)|baSM_S|12\rangle \right.$$
$$\left. + (-1)^S \langle \zeta c S' M_S'|12| \frac{r_<^k}{r_>^{k+1}} Y_{kq}^*(\theta_1, \phi_1) Y_{kq}(\theta_2, \phi_2)|abSM_S|12\rangle \right), \tag{4.79}$$

As the operator is independent of spin, we can separate the spin and spatial components to obtain

$$\mathcal{M} = \langle S' M_S'|SM_S\rangle \sum_{kq} \frac{4\pi}{2k+1} \left(\langle \zeta c|12| \frac{r_<^k}{r_>^{k+1}} Y_{kq}^*(\theta_1, \phi_1) Y_{kq}(\theta_2, \phi_2)|ba|12\rangle \right.$$
$$\left. + (-1)^S \langle \zeta c|12| \frac{r_<^k}{r_>^{k+1}} Y_{kq}^*(\theta_1, \phi_1) Y_{kq}(\theta_2, \phi_2)|ab|12\rangle \right). \tag{4.80}$$

We use the orthonormality of the spin wavefunctions to express $\langle S' M_S'|SM_S\rangle$ as $\delta_S^{S'} \delta_M^{M'}$.

$$\mathcal{M} = \delta_S^{S'} \delta_M^{M'} \sum_{kq} \frac{4\pi}{2k+1} \left(\langle \zeta c|12| \frac{r_<^k}{r_>^{k+1}} Y_{kq}^*(\theta_1, \phi_1) Y_{kq}(\theta_2, \phi_2)|ba|12\rangle \right.$$
$$\left. + (-1)^S \langle \zeta c|12| \frac{r_<^k}{r_>^{k+1}} Y_{kq}^*(\theta_1, \phi_1) Y_{kq}(\theta_2, \phi_2)|ab|12\rangle \right). \tag{4.81}$$

This can be expressed as

$$
\begin{aligned}
\mathcal{M} = \delta_S^{S'} \delta_M^{M'} \sum_{kq} \frac{4\pi}{2k+1} \int d^3\mathbf{r}_1 \int d^3\mathbf{r}_2 \\
\left(\phi_\zeta^*(\mathbf{r}_1)\phi_c^*(\mathbf{r}_2) \frac{r_<^k}{r_>^{k+1}} Y_{kq}^*(\theta_1,\phi_1) Y_{kq}(\theta_2,\phi_2) \phi_b(\mathbf{r}_1)\phi_a(\mathbf{r}_2) \right. \\
\left. + (-1)^S \, \phi_\zeta^*(\mathbf{r}_1)\phi_c^*(\mathbf{r}_2) \frac{r_<^k}{r_>^{k+1}} Y_{kq}^*(\theta_1,\phi_1) Y_{kq}(\theta_2,\phi_2) \phi_a(\mathbf{r}_1)\phi_b(\mathbf{r}_2) \right).
\end{aligned}
\tag{4.82}
$$

We use the SCE, eqn (4.1), to split this expression into radial and angular components.

$$
\begin{aligned}
\mathcal{M} = \delta_S^{S'} \delta_M^{M'} \sum_{\substack{l_\zeta m_\zeta l_c m_c kq \\ l_a m_a l_b m_b}} \frac{4\pi}{2k+1} \int d^3\mathbf{r}_1 \int d^3\mathbf{r}_2 \frac{1}{r_1^2 r_2^2} \\
\left[\left(P_{\zeta,l_\zeta m_\zeta}(r_1) P_{c,l_c m_c}(r_2) \frac{r_<^k}{r_>^{k+1}} P_{b,l_b m_b}(r_1) P_{a,l_a m_a}(r_2) \right. \right. \\
\left. Y_{l_\zeta m_\zeta}^*(\Omega_1) Y_{l_c m_c}^*(\Omega_2) Y_{kq}^*(\Omega_1) Y_{kq}(\Omega_2) Y_{l_b m_b}(\Omega_1) Y_{l_a m_a}(\Omega_2) \right) \\
+ (-1)^S \left(P_{\zeta,l_\zeta m_\zeta}(r_1) P_{c,l_c m_c}(r_2) \frac{r_<^k}{r_>^{k+1}} P_{a,l_a m_a}(r_1) P_{b,l_b m_b}(r_2) \right. \\
\left. \left. Y_{l_\zeta m_\zeta}^*(\Omega_1) Y_{l_c m_c}^*(\Omega_2) Y_{kq}^*(\Omega_1) Y_{kq}(\Omega_2) Y_{l_a m_a}(\Omega_1) Y_{l_b m_b}(\Omega_2) \right) \right].
\end{aligned}
\tag{4.83}
$$

where $\Omega_i = (\theta_i, \phi_i)$ is the angular coordinates of the ith electron. The angular integrals over the triplets of spherical harmonics can be written in terms of Wigner-3j symbols [92] as

$$
\begin{aligned}
\int d\Omega Y_{LM}^*(\Omega) Y_{kq}(\Omega) Y_{l'm'}(\Omega) \\
= (-1)^M \sqrt{\frac{(2L+1)(2k+1)(2l'+1)}{4\pi}} \begin{pmatrix} L & k & l' \\ 0 & 0 & 0 \end{pmatrix} \begin{pmatrix} L & k & l' \\ -M & q & m' \end{pmatrix}
\end{aligned}
\tag{4.84}
$$

Expanding the integrals in eqn (4.85) and substituting in eqn (4.84), we obtain

$$
\mathcal{M} = \delta_S^{S'} \delta_M^{M'} \sum_{\substack{l_\zeta m_\zeta l_c m_c kq \\ l_a m_a l_b m_b}} \int dr_1 \int dr_2
$$

$$
(-1)^{m_\zeta + m_c + q} \sqrt{(2l_\zeta + 1)(2l_c + 1)(2l_b + 1)(2l_a + 1)}
$$

$$
\left[\left(P_{\zeta, l_\zeta m_\zeta}(r_1) P_{c, l_c m_c}(r_2) \frac{r_<^k}{r_>^{k+1}} P_{b, l_b m_b}(r_1) P_{a, l_a m_a}(r_2) \right.\right.
$$

$$
\left. \begin{pmatrix} l_\zeta & k & l_b \\ 0 & 0 & 0 \end{pmatrix} \begin{pmatrix} l_\zeta & k & l_b \\ -m_\zeta & -q & m_b \end{pmatrix} \begin{pmatrix} l_c & k & l_a \\ 0 & 0 & 0 \end{pmatrix} \begin{pmatrix} l_c & k & l_a \\ -m_c & q & m_a \end{pmatrix} \right) \tag{4.85}
$$

$$
+ (-1)^S \left(P_{\zeta, l_\zeta m_\zeta}(r_1) P_{c, l_c m_c}(r_2) \frac{r_<^k}{r_>^{k+1}} P_{a, l_a m_a}(r_1) P_{b, l_b m_b}(r_2) \right.
$$

$$
\left.\left. \begin{pmatrix} l_\zeta & k & l_a \\ 0 & 0 & 0 \end{pmatrix} \begin{pmatrix} l_\zeta & k & l_a \\ -m_\zeta & -q & m_a \end{pmatrix} \begin{pmatrix} l_c & k & l_b \\ 0 & 0 & 0 \end{pmatrix} \begin{pmatrix} l_c & k & l_b \\ -m_c & q & m_b \end{pmatrix} \right) \right].
$$

4.6.2 Summation

To find the total Auger rate of a transition, we must sum over the final states and average over the initial states [59]. The summation over the final states is due to the possible pathways from a single initial state, the average over the initial state is because that state is not explicitly defined. In this case, the initial state has a core hole in a specific orbital with either up or down spin. To average over these possibilities, we introduce a factor of a half. In general, the Auger rate is given by

$$
\Gamma = \overline{\sum} 2\pi N_{12} N_h |\mathcal{M}|^2, \tag{4.86}
$$

where $\overline{\sum}$ denotes a sum over final states and average over initial states [37], N_h is

the number of holes in the specified orbital, and N_{12} is defined as

$$
\begin{aligned}
N_{12} &= \frac{N_1 N_2}{2 \times 2} && \text{for electrons in different orbitals} \\
&= \frac{N_1 (N_1 - 1)}{2 \times 2 \times 1} && \text{for electrons in same orbital.}
\end{aligned}
\tag{4.87}
$$

This is equivalent to eqn (2.3) where the maximum occupancy of the molecular orbitals is 2. In this general case, $\mathcal{M}$ could be in any scheme and the summation would be over the quantum numbers of the scheme. In the SM_S scheme, we sum over S, M_S, S' and M_S' and use a matrix element with well-defined $SM_S S' M_S'$, given in eqn (4.85). In this case, the initial state has a core hole in a specific orbital with either up or down spin. To average over these possibilities, we introduce a factor of a half. We also sum over ζ because we aren't interested in the state of the continuum electron. This expression gives the total Auger transition rate from valence electrons in spatial orbitals a and b which fill a core hole in the spatial orbital c.

$$
\Gamma_{b,a \to c} = \sum_{SM_S S' M_S'} \pi N_{12} N_h \sum_{\zeta} |\langle \phi(\zeta c S' M_S')| \frac{1}{r_{12}} |\phi(baSM_S)\rangle|^2
\tag{4.88}
$$

The advantage of using the $m_1 m_2 SM_S$ scheme is that we can obtain the contribution from the singlet and triplet states separately. To do this, we use eqn (4.88), but rather than summing over S, we instead pick one specific S.

Chapter 5

Free-electron laser interactions with molecular nitrogen

There is a large body of existing work concerning free-electron laser (FEL) interactions with molecular nitrogen. Experimental studies [19, 20, 53, 54, 55] have measured the ion yields produced by an FEL pulse and the formation of double-core-hole (DCH) states. Theoretical works [22, 23] have calculated the ion yields produced in these interactions and determined the contribution of DCH states, using models which treat the molecule as a combination of independent atoms. In our work, we treat the molecule using molecular bound and continuum wavefunctions.

In this chapter, we investigate the interplay between single-photon ionisation, Auger decay and dissociation that occurs during the interaction of molecular nitrogen with an FEL pulse. We use a rate equation model, with transitions rates calculated using the methods described in the previous chapter, to calculate the atomic and molecular ion yields produced by an FEL interaction with N_2. Further, we obtain the population that travels through the different pathways of transitions to arrive at these final ionic states and the electron spectra produced during these interactions.

5.1 Calculation details

5.1.1 Pulse parameters

As in section 3.1.2, we treat the pulse as monochromatic and express the photon flux using eqn (3.5). For molecular nitrogen, we choose two different photon energies, we use 1100 eV to compare with experimental data and 525 eV to make best use of our model. Previous work using atomic continuum orbitals are least accurate at low energies, where the effects of the molecular potential are more profound. As we use fully molecular bound and continuum orbitals, this regime can be treated more accurately by our model. Three pulse durations were chosen, 4 fs, 7 fs and 80 fs. These values were chosen to compare with experiment and to see the effect of varying pulse duration on the ion yields and pathways. We also considered a variety of intensities, in order to determine how the intensity changed the ion populations and the pathways leading to these ions.

5.1.2 Bound molecular orbitals

We used the Molpro [71] quantum chemistry package to compute each bound molecular orbital of every electronic configuration of molecular nitrogen of the form $1\sigma_g^\alpha 1\sigma_u^\beta 2\sigma_g^\gamma 2\sigma_u^\delta 1\pi_{ux}^\varepsilon 1\pi_{uy}^\zeta 3\sigma_g^\eta$, where $\alpha, \beta, \gamma, \delta, \varepsilon, \zeta, \eta$ are the orbital occupations and have values between 0 and 2. The *g* and *u* subscripts denote the gerade or ungerade symmetry of the orbitals, ungerade wavefunctions change sign following inversion through the molecular centre, gerade wavefunctions do not. Using Molpro, we compute each molecular orbital as a combination of atomic orbitals and assume the nuclei are fixed at the equilibrium internuclear distance of N_2, 2.08 a.u.. We used the Hartree-Fock method and a correlation-consistent polarised valence triple-zeta basis set (cc-pVTZ) [93]. This basis set is less computationally intensive than higher-zeta basis sets, while still providing good accuracy. In this basis set, nitrogen orbitals are expressed in terms of four *s*, three *p*, two *d* and one *f* contracted gaussians, which are constructed from ten *s*, five *p*, two *d* and one *f* primitive gaussians, respectively. For molecular nitrogen, N_2, there will be twice as many basis functions, corresponding to the two atomic sites.

5.1.2.1 Single-centre expansion

For the single-centre expansion of the bound molecular orbitals of N_2, we express the wavefunctions in terms of spherical harmonics with $l <= 30$. As N_2 is a di-atomic molecule, there is rotational symmetry about the internuclear axis and orbitals have well-defined m. This means that, while we express each orbital in terms of multiple spherical harmonics, all of the spherical harmonics for a given orbital will have the same m values. In addition each orbital is either gerade or ungerade. The gerade and ungerade status of the orbitals means that only the even or odd spherical harmonics will contribute.

5.1.3 Molecular continuum orbitals

To calculate the molecular continuum orbitals of N_2, we solve eqn (4.6) as discussed in section 4.4. We find that convergence of the continuum orbital is achieved when expressed in terms of spherical harmonics with $l \leq 19$. This means that, for each continuum energy, ε, we consider degenerate solutions with $L \leq 19$. Note that this L does not correspond to angular momentum, it simply labels the different solutions referred to in eqn (4.49). The gerade (ungerade) nature of the continuum orbital means that only the even (odd) spherical harmonics will contribute to the orbital. This also reduces the number of degenerate solutions.

For our calculations of N_2 continuum orbitals, we assume the nuclei are fixed at the equilibrium distance of N_2, 2.08 a.u.. In addition, when we use the Laplace multipole expansion [94] to express $1/|\mathbf{r} - \mathbf{r}'|$ in eqn (A.2), we expand up to $k = 30$, as this value gave good convergence. We use an integration grid from $r = 10^{-10}$ a.u. to $r = 40$ a.u. with a step size of $r = 0.01$ a.u. and determine the a and b coefficients for each calculation as discussed in Appendix B.

5.1.4 Dissociation

As we ionise nitrogen, we will produce charged ions. Some of these molecular ions, particularly the higher-charged ions, are unstable and will dissociate. In the dissociation process, the molecule splits into two atomic nitrogen fragments. In our work, we assume that the nuclei are fixed at the equilibrium distance of N_2, 2.08

a.u. and account for the dissociation with additional terms in the rate equations. We assume that all configurations of N_2^{4+} and configurations of N_2^{3+} without core holes dissociate instantaneously into $N^{2+} + N^{2+}$ and $N^{2+} + N^+$, respectively [23, 55]. We use a very large transition rate for the dissociation to approximate the instantaneous dissociation. Following previous work [23, 55], we also assume that all electronic configurations of N_2^{2+} dissociate, with a lifetime of 100 fs based on experimental work [95]. N_2^{2+} fragments into $N^+ + N^+$ in 74% of cases and $N^{2+} + N$ in 26% of cases [95].

5.2 Rate comparisons

5.2.1 Photo-ionisation cross-sections

E_{photon}(eV)	$2\sigma_g \to \varepsilon\sigma_u$		$2\sigma_g \to \varepsilon\pi_u$	
	Ref. [96]	This Work	Ref. [96]	This Work
40	0.035	0.038	0.073	0.20
45	0.58	0.55	0.22	0.38
50	2.6	2.5	0.41	0.52
55	1.9	2.0	0.59	0.63
60	1.1	1.2	0.71	0.69
65	0.74	0.80	0.75	0.73
70	0.54	0.58	0.74	0.73
75	0.40	0.44	0.70	0.72
80	0.31	0.33	0.65	0.69

Table 5.1: Photo-ionization cross-sections for N_2 transitions: columns 3 and 5 correspond to our results and columns 2 and 4 correspond to previous calculations [96]

Using eqn. 4.70, we calculated the photo-ionisation cross-sections for several transitions in N_2 and compared them with previous calculations [96]. We find a good agreement, as can be seen for the two cases considered in Table 5.1. Differences between our results and the results in ref. [96] might be due to the fact that in ref. [96] the Hartee-Fock equations are solved with $a_i = 2$ and $b_i = 1$ for all orbitals which is not the case in our calculations, see Appendix B.

5.2.2 Auger rates

Next, we compare our results for the Auger rates of N_2^+ with a 1s core-hole, which are computed using eqn (4.88), with the Auger rates calculated using a Green's

Final State	Valence 1	Valence 2	This Work	Ref. [97]
$^3\Sigma_u^+$	$2\sigma_u$	$3\sigma_g$	0.01	0.01
$^1\Sigma_u^+$	$2\sigma_u$	$3\sigma_g$	0.05	0.11
$^3\Pi_u$	$3\sigma_g$	$1\pi_{ux}(1\pi_{uy})$	0.01	0.01
$^1\Pi_u$	$3\sigma_g$	$1\pi_{ux}(1\pi_{uy})$	0.11	0.13
$^3\Pi_g$	$2\sigma_u$	$1\pi_{ux}(1\pi_{uy})$	0.02	0.03
$^1\Pi_g$	$2\sigma_u$	$1\pi_{ux}(1\pi_{uy})$	0.08	0.13
$^3\Pi_u$	$2\sigma_g$	$1\pi_{ux}(1\pi_{uy})$	0.03	0.01
$^1\Pi_u$	$2\sigma_g$	$1\pi_{ux}(1\pi_{uy})$	0.09	0.06
$^3\Sigma_u^+$	$2\sigma_g$	$2\sigma_u$	0.01	0.01
$^1\Sigma_u^+$	$2\sigma_g$	$2\sigma_u$	0.20	0.11
$^3\Sigma_g^+$	$2\sigma_g$	$3\sigma_g$	0.02	0.02
$^1\Sigma_g^+$	$2\sigma_g$	$3\sigma_g$	0.08	0.07
$^1\Sigma_g^+$	$3\sigma_g$	$3\sigma_g$	0.05	0.04
$^1\Delta_g$	$1\pi_{ux}(1\pi_{uy})$	$1\pi_{ux}(1\pi_{uy})$	0.09	0.12
$^1\Sigma_g^+$	$1\pi_{ux}(1\pi_{uy})$	$1\pi_{uy}(1\pi_{ux})$	0.03	0.01
$^1\Sigma_g^+$	$2\sigma_u$	$2\sigma_u$	0.05	0.13
$^1\Sigma_g^+$	$2\sigma_g$	$2\sigma_g$	0.07	0.02

Table 5.2: Ratio of each Auger transition for a 1s core-hole divided by the sum of all Auger transitions for a 1s core-hole for N_2

function method [97]. The 1s state corresponds to $\phi_{1s} = \frac{1}{\sqrt{2}}\left(\phi_{1\sigma_g} + \phi_{1\sigma_u}\right)$. Using the orthonormality of the molecular states, it follows that the 1s Auger rates are obtained by averaging the $1\sigma_g$ and $1\sigma_u$ Auger rates. In the work in ref. [97], only relative values of the Auger rates are given. Specifically, the ratio of each Auger rate is given with respect to the the Auger rate for the transition to the $^1\Sigma_g^+$ state with $3\sigma_g$ electrons filling in the core hole and being ejected to the continuum; we denote this transition by $^1\Sigma_g^+(3\sigma_g3\sigma_g)$. To compare the results in ref. [97] with our values we divide each Auger transition by the sum of all Auger transitions for a 1s core-hole state. The resulting values are shown in Table 5.2 and the overall agreement is shown to be good. The agreement between some of the Auger rates we compute in the current work and the Auger rates in ref. [97] is not as good. We believe this is due to the different techniques employed to compute the Auger rates. This is supported by further comparing Auger rates computed in the current work with results for Auger rates given in ref. [97] and ref. [98]. In the latter work, the author employs a configuration interaction calculation to compute the Auger rates

Final State	Valence 1	Valence 2	This Work	Ref. [97]	Ref. [98]
$^1\Sigma_g^+$	$3\sigma_g$	$3\sigma_g$	1.00	1.00	1.00
$^3\Sigma_u^+$	$2\sigma_u$	$3\sigma_g$	0.16	0.17	0.43
$^1\Pi_u$	$3\sigma_g$	$1\pi_{ux}(1\pi_{uy})$	2.39	3.37	1.57
$^1\Delta_g$	$1\pi_{ux}(1\pi_{uy})$	$1\pi_{ux}(1\pi_{uy})$	2.02	3.00	2.70
$^1\Sigma_g^+$	$1\pi_{ux}(1\pi_{uy})$	$1\pi_{uy}(1\pi_{ux})$	0.58	0.34	1.59
$^1\Sigma_u^+$	$2\sigma_u$	$3\sigma_g$	1.06	2.93	1.97

Table 5.3: Ratio of some of the Auger transitions for a 1s core-hole or N_2 divided by the Auger transition to the $^1\Sigma_g^+(3\sigma_g3\sigma_g)$ state

Auger Rate	$^1\Sigma_g^+(3\sigma_g3\sigma_g)$	$^1\Sigma_u^+(2\sigma_u3\sigma_g)$
Ref. [47]	1	1.17
Ref. [98]	1	1.97
Ref. [97]	1	2.93
This work	1	1.53
Experimental [47]	1	1.55(8)

Table 5.4: Combined Auger rates of transitions from the $1\sigma_g$ and the $1\sigma_u$ core hole molecular states of N_2^+ to the $^1\Sigma_g^+(3\sigma_g3\sigma_g)$ and $^1\Sigma_u^+(2\sigma_u3\sigma_g)$ states, respectively. The rates are given relative to the $^1\Sigma_g^+(3\sigma_g3\sigma_g)$ transition rate.

of N_2^+ with a 1s core hole. As in ref. [97], in ref. [98] only relative values of the Auger rates are given.

In Table 5.3 we compare the ratio of some 1s Auger rates with the Auger rate for the $^1\Sigma_g^+(3\sigma_g3\sigma_g)$ transition. We find that any two techniques agree for only some of the transitions shown in Table 5.3. In these calculations for Table 5.2 and Table 5.3 the Auger rates are split by the total spin of the final state, however, the Auger rates used in the rate equations are summed over all allowed spin configurations. This is because spin is not specified in the electronic configurations of the molecular states.

In addition, in Table 5.4 we compare our values with the experimental and theoretical results in ref. [47] for the Auger transitions from the $1\sigma_g$ and the $1\sigma_u$ core hole molecular states of N_2^+ to the $^1\Sigma_g^+(3\sigma_g3\sigma_g)$ and $^1\Sigma_u^+(2\sigma_u3\sigma_g)$ states. We find a very good agreement with the experimental values, while the agreement between the results in ref. [97] and ref. [98] with ref. [47] is not as good. In Table 5.5, we also compare the ratio of the transition rates from the $1\sigma_g$ and the $1\sigma_u$ core hole

Γ^g/Γ^u	$^1\Sigma_g^+(3\sigma_g 3\sigma_g)$	$^1\Sigma_u^+(2\sigma_u 3\sigma_g)$
Ref. [47]	1.98	1.00
(This work)	2.02	0.97
Experimental [47]	2.15(11)	0.80(4)

Table 5.5: Relative Auger rates of transitions from the $1\sigma_g$ and the $1\sigma_u$ core hole molecular states of N_2^+, labelled Γ^g and Γ^u, respectively, to the $^1\Sigma_g^+(3\sigma_g 3\sigma_g)$ and $^1\Sigma_u^+(2\sigma_u 3\sigma_g)$ states

molecular states of N_2^+. Again, we find a very good agreement with the experimental values. Moreover, we find that the sum of all Auger rates corresponding to a 1s core-hole is equal to 2.87×10^{-3} a.u.. This value compares well with the experimental value of 3.77×10^{-3} a.u. obtained in ref. [19].

5.3 Rate equations

In order to model the interplay of single-photon ionisations, Auger decays and dissociative transitions, we use a system of rate equations. We have one rate equation for each accessible state of atomic and molecular nitrogen. To account for the transitions between atomic states, we must also calculate the atomic photo-ionisation cross-sections and Auger rates, following the procedures explained in chapter 2. With the atomic and molecular photo-ionisation cross-sections and Auger rates, in addition to the dissociation rates, we can now run rate equation calculations. We do not include fluorescence transitions in the rate equations as they are negligible compared to photo-ionisation and Auger decay rates [99]. Similarly, at x-ray energies, multi-photon processes will not contribute significantly. The rate equations describing the percentage of the population $\mathscr{I}_j(t)$ in a molecular ion state j take the form

$$\frac{d}{dt}\mathscr{I}_j(t) = \sum_i \left(\sigma_{i\to j}J(t) + \Gamma_{i\to j}\right)\mathscr{I}_i(t) \tag{5.1}$$

$$- \sum_k \left(\sigma_{j\to k}J(t) + \Gamma_{j\to k}\right)\mathscr{I}_j(t) - \sum_n \kappa_{j\to n,p}\mathscr{I}_j(t),$$

$$\frac{d}{dt}\mathscr{A}_{i\to j} = \Gamma_{i\to j}\mathscr{I}_i(t),$$

$$\frac{d}{dt}\mathscr{P}_{i\to j} = \sigma_{i\to j}J(t)\mathscr{I}_i(t).$$

$\sigma_{i\to j}$ and $\Gamma_{i\to j}$ are the molecular single-photon absorption cross section and Auger decay rate, respectively, from the initial molecular state i to the final molecular state j. The molecular states i, j and k have charges q-1, q and q+1, respectively. $\kappa_{j\to n,p}$ denotes the dissociation rate from the initial molecular state j with charge q to the final atomic states n and p. The atomic states n and p have total charge equal to q. For the dissociation cases currently considered, for each atomic final fragment n there is only one atomic final fragment p. The first term in eqn (5.1) accounts for the formation of the molecular state j through the single-photon ionization and Auger decay of the molecular state i. The second term in eqn (5.1) accounts for the depletion of the molecular state j by transitioning to a molecular state k through single-photon ionization and Auger decay. The third term accounts for the depopulation of the molecular state j through dissociation to the atomic states n and p. These rate equations, eqn (5.1), are used to calculate the molecular ion yields. In addition, in eqn (5.1), we solve for the Auger $\mathscr{A}_{i\to j}$ and the photo-ionization $\mathscr{P}_{i\to j}$ yield from an initial molecular state i with charge q-1 to a final molecular state j with charge q. The rate equations describing the populations of an atomic state n

take the form

$$\frac{d}{dt}\mathscr{I}_n(t) = \sum_m \left(\sigma_{m \to n} J(t) + \Gamma_{m \to n} \right) \mathscr{I}_m(t) \tag{5.2}$$

$$- \sum_o \left(\sigma_{n \to o} J(t) + \Gamma_{n \to o} \right) \mathscr{I}_n(t) + \sum_j \frac{\kappa_{j \to n,p}}{2 - \delta_{n,p}} \mathscr{I}_j(t),$$

$$\frac{d}{dt}\mathscr{A}_{m \to n} = 2\Gamma_{m \to n} \mathscr{I}_m(t),$$

$$\frac{d}{dt}\mathscr{P}_{m \to n} = 2\sigma_{m \to n} J(t) \mathscr{I}_m(t),$$

where the indices n, m and o refer to atomic states with charges, q, q-1 and q+1, respectively, while j refers to molecular states. The first term in eqn (5.2) accounts for the formation of the atomic state n through the single-photon ionization and Auger decay of the atomic state m. The second term in eqn (5.2) accounts for the depletion of the atomic state n by transitioning to an atomic state o through single-photon ionization and Auger decay. The third term in eqn (5.2) accounts for the population of state n as a result of dissociative transitions from a molecular state j. The factor $\frac{1}{2-\delta_{n,p}}$ conserves the the total probability. Namely, if the molecular state results in the same two atomic fragments the factor is equal to 1. If fragmentation results in two different atomic fragments the factor is equal to $\frac{1}{2}$, since a rate equation is formulated for each atomic fragment separately. This means that the actual atomic populations are given by $2\mathscr{I}_n$. As in the molecular rate equations, in eqn (5.2), we solve for the Auger $\mathscr{A}_{m \to n}$ and the photo-ionization $\mathscr{P}_{m \to n}$ yields from an initial atomic state i with charge q-1 to a final atomic state j with charge q. Here, we have factors of two to account for the actual atomic populations being $2\mathscr{I}_n$. We note that eqn (5.1) and eqn (5.2) are solved simultaneously. We obtain the molecular and atomic ion yields long after the end of the laser pulse.

The three types of rate equations used to compute the population through a specific pathway $i \to j \to k$ are given by eqns (5.3-5.5)

$$\frac{d}{dt}\mathscr{I}_{i\to j\to k}(t) = (\sigma_{j\to k}J(t) + \Gamma_{j\to k})\mathscr{I}_{i\to j}(t) \tag{5.3}$$

$$-\sum_{l}(\sigma_{k\to l}J(t) + \Gamma_{k\to l})\mathscr{I}_{i\to j\to k}(t) - \sum_{n}\kappa_{k\to n,p}\mathscr{I}_{i\to j\to k}(t),$$

$$\frac{d}{dt}\mathscr{I}_{i\to j\to n}(t) = \frac{\kappa_{j\to n,p}}{2 - \delta_{n,p}}\mathscr{I}_{i\to j}(t) \tag{5.4}$$

$$-\sum_{o}(\sigma_{n\to o}J(t) + \Gamma_{n\to o})\mathscr{I}_{i\to j\to n}(t),$$

$$\frac{d}{dt}\mathscr{I}_{i\to m\to n}(t) = (\sigma_{m\to n}J(t) + \Gamma_{m\to n})\mathscr{I}_{i\to m}(t) \tag{5.5}$$

$$-\sum_{o}(\sigma_{n\to o}J(t) + \Gamma_{n\to o})\mathscr{I}_{i\to m\to n}(t).$$

The indices *i*, *j*, *k* and *l* refer to molecular states whereas the indices *m*, *n* and *o* refer to atomic states. Eqn (5.3) computes molecular pathway populations, eqn (5.4) computes pathway populations where the final state is an atomic one, but the previous states were molecular. Pathway populations where the final and the previous states are atomic ones are computed using eqn (5.5). Solving eqns (5.3-5.5), allows us to register all energetically-allowed pathways.

5.3.1 Rate equation parameters

For our model, we constructed rate equations for each electronic state of molecular or atomic nitrogen that is accessible by a 525 eV or 1100 eV photon energy FEL pulse. There are 309 states that are accessible by a pulse with 1100 eV photons, therefore we must solve 309 simultaneous rate equations to model the interaction of N_2 with an FEL pulse. For most calculations, we assume that the sample is localised at a single point, such that there is no spatial variation in intensity. We compute the rate equations between -200 fs and 1000 fs, this ensures that the entirety of the pulse is included and gives all states additional time after the pulse ends to decay via the Auger process or dissociate. We then measure the ion yields that are present 1000 fs
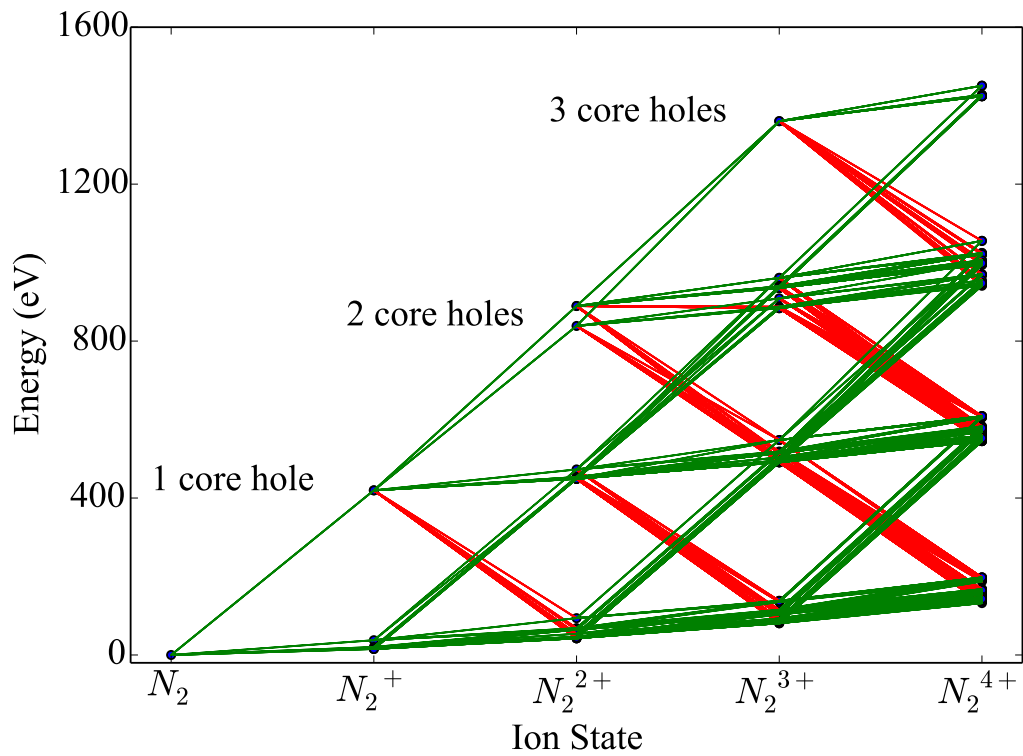
Figure 5.1: Ionization pathways between the different electronic states of N_2 up to N_2^{4+} that are accessible with sequential single-photon ($\hbar\omega = 525\,eV$) absorptions and Auger decays. The green and red lines indicate photo-ionization and Auger transitions, respectively.

after the pulse maximum. The possible molecular transitions, up to N_2^{4+}, available for a pulse with 525 eV photons interacting with N_2 are shown below:

5.4 Comparison of atomic ion yields with experiment

Now that we have constructed our model, it is important to verify the results we obtain compare well with experiment. In our model, we have assumed that the molecular nitrogen is located at the highest intensity point of the beam. To compare with experimental data [55], we consider that N_2 is spread over an area of varying intensity. To replicate the conditions of the experiment, we take the FEL flux to be given by

$$J(x,y,t) = \rho(x,y)\Gamma_{ph}(t),$$
(5.6)

where $\Gamma_{ph}(t)$ is the total rate of photons at time t and $\rho(x,y)$ is the transverse beam profile given by

$$\rho(x,y) = \frac{4ln2}{\pi\rho_x\rho_y}e^{-4ln2[(\frac{x}{\rho_x})^2+(\frac{y}{\rho_y})^2]},$$
(5.7)

with $\rho_x = 2.2\mu$m and $\rho_y = 1.2\mu$m being the FWHM in the x and y dimensions, respectively. These values are chosen to match the parameters used in the experiments we compare with [55]. The total rate of photons across the cross-section, $\Gamma_{ph}(t)$, is given by

$$\Gamma_{ph}(t) = \Gamma_{ph,0}e^{-4ln2(\frac{t}{\tau})^2},$$
(5.8)

where τ is the FWHM of the pulse in time and $\Gamma_{ph,0}$ is the peak rate of photons given by

$$\Gamma_{ph,0} = 2\sqrt{\frac{ln2}{\pi}}\frac{n_{ph}}{\tau}.$$
(5.9)

$n_{ph} = E_p/\omega$ is the number of photons, each with energy ω, in a pulse with energy
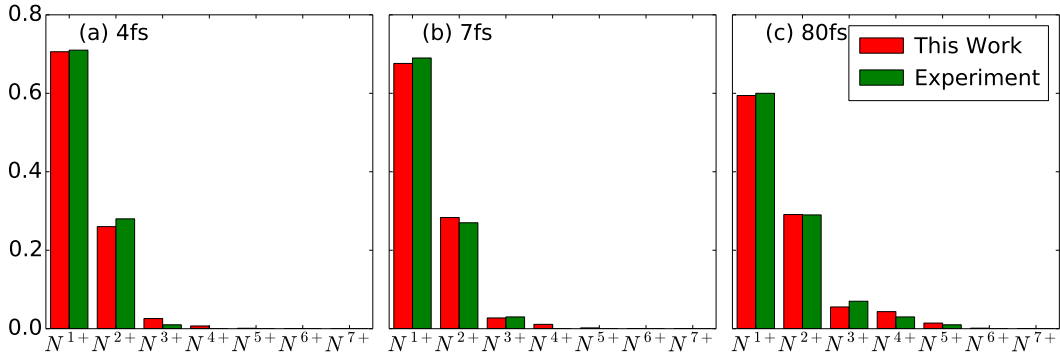
Figure 5.2: Charged atomic ion yields produced by various FEL pulses interacting with N_2 integrated over a 10 μm by 10 μm area. The pulse parameters used for each plot were a) pulse energy 0.15 mJ with 4 fs FWHM and 77% loss b) pulse energy 0.26 mJ with 7 fs FWHM and 84% loss c) pulse energy 0.26 mJ with 80 fs FWHM and 70% loss. Our results are displayed with experimental results [23, 55] for comparison.

E_p. To compare with this experiment, we must include the effects of photon beam transport losses. To incorporate this, we multiply the pulse energy by a factor corresponding to the losses reported in the experimental work [55]. We calculate the ion yields on a grid of area 10 μm by 10 μm consisting of 31 points in x and 31 points in y. To compute this, we find the intensity at each of these points and calculate the ion yields generated by a pulse of that intensity. We then integrate the ion yields over the area and normalise the values such that the sum of the charged atomic ion yields is equal to 1. We perform this calculation for 4 fs, 7 fs and 80 fs pulses, so as to compare with the experimental values used. The comparisons are displayed in Fig. 5.2. We find that the ion yields calculated with our method are in agreement with the experimental data for all pulse durations.

Having established that our model can reproduce experimental ion yields, we can use it to investigate the dependence of the ion yields on the pulse parameters.

5.5 Ion yields

We calculated the atomic and molecular ion yields of nitrogen for four different FEL pulses, assuming that initially only neutral N_2 is populated. We considered FEL pulses with either 525 eV or 1100 eV photons. For each energy, we calculated the yields produced by a 4 fs or 80 fs FWHM pulse. The molecular yields are
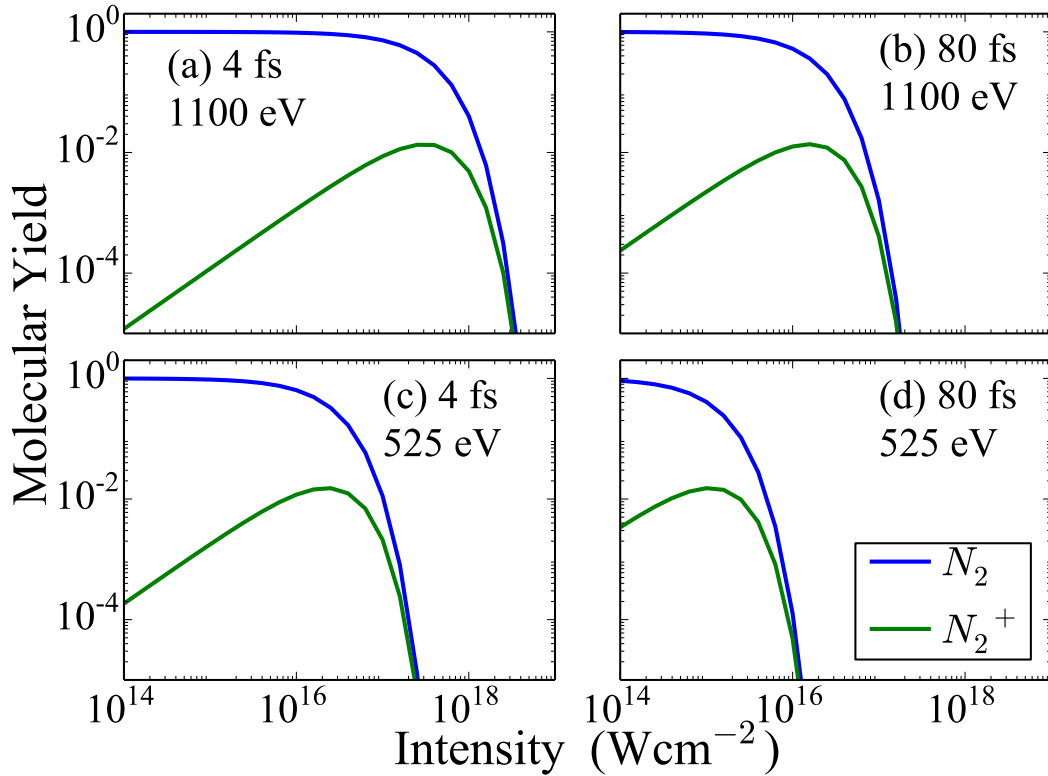
Figure 5.3: Molecular ion yields of N_2 following one of four FEL pulses as a function of the intensity of the laser pulse. The yield is given as a proportion of the total population, a portion of which populates atomic states of nitrogen.

displayed in Fig. 5.3. There are only N_2 and N_2^+ molecular states present in the ion yields as higher-charged states dissociate. We find that at low intensity, almost all of the population is in neutral N_2, as all transitions that depopulate this configuration are dependent on the photon flux. As the intensity rises, the yield of N_2 and N_2^+ fall off dramatically, the intensity where this happens depends on the FWHM and photon energy of the pulses. Comparing (a) and (b), we find that the longer pulse causes the molecular ion yields to fall at a lower intensity than the short pulse. This is due to the increased total photon flux which results in an increased number of photo-ionisation transitions. The effect of the photon energy is seen by comparing (a) and (c). For a photon energy of 525 eV the molecular ion yields drop at a lower intensity than for a 1100 eV photon energy. There are two reasons for this, one is that a lower photon energy, for a fixed intensity, gives a higher photon flux, the other reason is that the lower energies are closer to the ionisation energies and therefore give larger photo-ionisation cross-sections. Both of these effects lead to
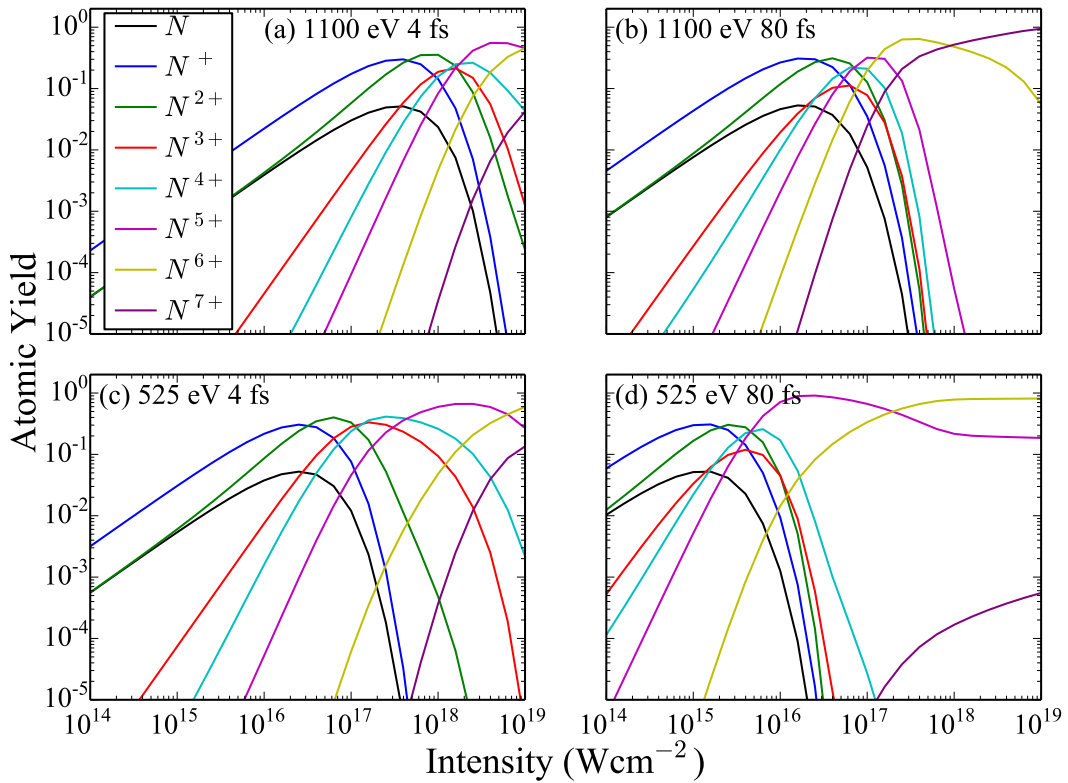
Figure 5.4: Atomic ion yields of N_2 following one of four FEL pulses as a function of the
intensity of the laser pulse. The yield is given as a percentage of the total atomic
and molecular population.

higher photo-ionisation transition rates and increase the rate at which the N_2 and
N_2^+ configurations are depopulated.

The atomic ion yields are displayed in Fig. 5.4 for the same set of pulses
as in Fig. 5.3. We see that more population reaches the higher-charged states as
we increase intensity. However, the intensity at which the peak yields are reached
varies between pulses, as the pulses give different photo-ionisation transition rates.
Comparing (b) and (d), we can see the effect of photon energy on the ion yields. The
pulse with 1100 eV photon energy requires a larger intensity than the pulse with 525
eV photon energy for similar ion yields. This is due to a larger photon flux, given by
intensity divided by the photon energy, and a large photo-ionisation cross-section,
as the lower energies are closer to the ionisation energies. If we compare (c) and (d),
we see the effect of the pulse duration on the atomic ion yields. The longer pulse
will produce larger yields of higher-charged atomic ions than the shorter pulse. This

is due to the increased total photon flux during the 80 fs pulse, compared to the 4 fs pulse. There are other interesting features in this figure that we do not find in the molecular ion yields. At low intensity, most obviously in (a) and (c), we see that the N and N^{2+} yields are nearly identical. This is because the only way to produce neutral atomic nitrogen is via the dissociation of $N_2^{2+} \rightarrow N + N^{2+}$ and, for short, low intensity pulses, there will be few atomic transitions as dissociation typically occurs after the pulse ends. We also see that the gradients of the N, N^+ and N^{2+} ion yields are very similar at low intensities, as they are primarily populated by the dissociation of N_2^{2+}.

We also find that the N^{7+} yields of Fig. 5.3(d), where N^{6+} is the dominant yield at high intensity, as opposed to (b) where N^{7+} is the dominant yield at the highest intensities. This is due to a subset of the core photo-ionisation transitions in atomic nitrogen, which are energetically accessible with 1100 eV photons, but not with 525 eV photons. This means that if the only remaining electron in N^{6+} is a core electron, it can't be ionised by 525 eV photons.

5.6 Pathways

We now focus on the DCH states of molecular nitrogen, which have interesting properties for chemical analysis. However, these states decay rapidly, so the resultant ion yields at the end of the pulse will not have any DCH states present. This means that we have to identify other observables that indicate DCH formation. To do this, we calculate the pathways that populate different configurations and the population involved in each pathway. This gives us the percentage of the population in each ion yield that has accessed a DCH state during the interaction with the FEL pulse.
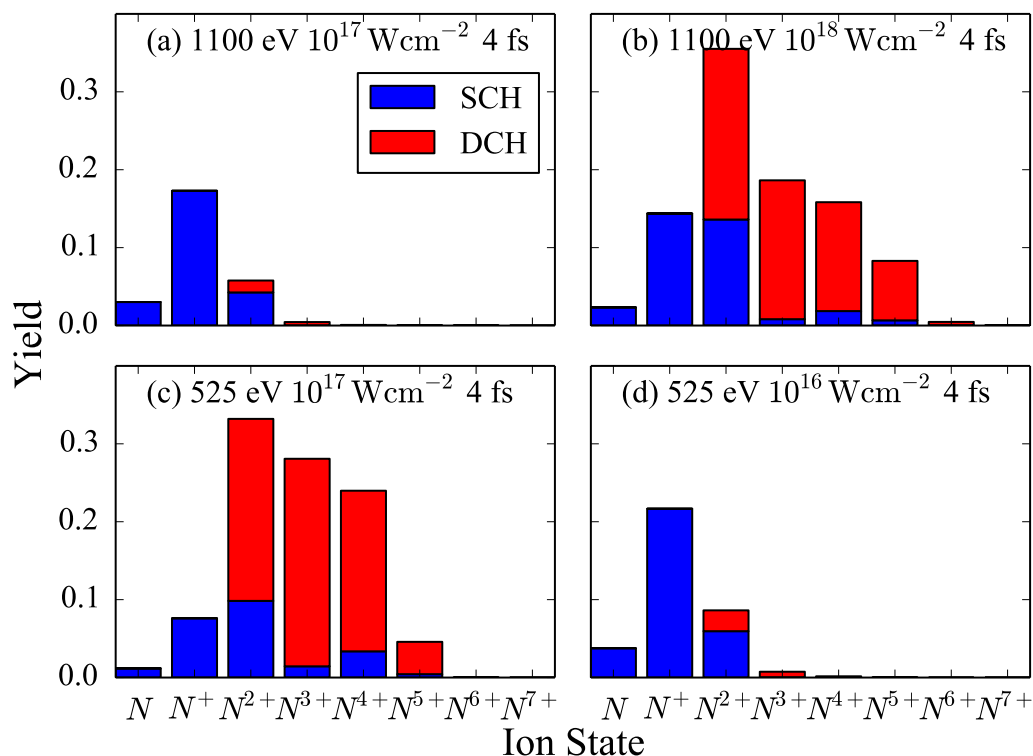
Figure 5.5: Atomic ion yields produced by N_2 interacting with FEL pulses with various pulse parameters. The ion yields are divided into two types, the red portion is the contribution of pathways that involve at least one DCH state of molecular nitrogen. The blue portion is the contribution of pathways that don't include any molecular states with more than one core hole.

In Fig. 5.5 we have plotted the atomic ion yields produced by four different FEL pulses. Further, we have identified the contributions of pathways involving molecular DCH states and those involving only a molecular SCH state. By comparing (a) and (b) or (c) and (d), we find that the higher intensity pulses produce higher atomic ion yields. We also find that pathways involving molecular DCH states contribute significantly more to these ion yields. This is due to the high intensity requirement to photo-ionise a second core electron, before Auger decay can take place. This means that, at low intensity, it is very difficult to produce DCH states. Comparing (a) and (c), we also find that, for a given intensity, reducing the photon energy leads to higher DCH state contributions and higher overall ion yields. This is due to higher photon flux and photo-ionisation cross-sections for 525 eV photon energy.

Calculating the pathway contributions also allows us to determine the dominant pathways that populate different ionic states. This reveals important information about the transitions that take place during the FEL pulse, which may not be obvious from experimental measurements. We identify the dominant pathways and determine which ones involve DCH states. We calculated the contributions of each type of pathway to the N, N^+, N^{2+}, N^{3+} and N^{4+} atomic ion yields for a $10^{17}\,\mathrm{Wcm}^{-2}$, 4 fs pulse with 525 eV photon energy. These contributions are displayed in Table 5.6, where core and valence photo-ionisations are denoted as P_C and P_V, respectively. A_{VV} refers to Auger transitions in which a valence electron fills in the core hole and another valence electron is ejected, A_{CV} refers to Auger transitions in which one of these electrons is a core electron. These A_{CV} are known as Coster-Kronig transitions [57] and they are a type of Auger transition that preserves the number of core holes, leading to further Auger decay. D denotes the dissociation of molecular states of nitrogen into atomic states.

N	$P_C A_{VV} D$	94%
N^+	$P_C A_{VV} D$	85%
N^{2+}	$\{P_C P_C + A_{VV} + A_{CV}/A_{VV}/P_C\}\,D$	62%
N^{2+}	$P_C A_{VV} P_C A_{VV} D$	21%
N^{3+}	$\{P_C P_C + A_{VV} + A_{CV}/A_{VV}/P_C\}\,D A_{VV}$	79%
N^{4+}	$\{P_C P_C + A_{VV} + A_{CV}/A_{VV}/P_C\}\,D\,\{P_C/A_{VV} + A_{VV}\}$	73%
N^{4+}	$P_C A_{VV} P_C A_{VV} D P_C A_{VV}$	9%

Table 5.6: The percentage contributions to the atomic ion yields up to N^{4+} of the dominant pathways of ionisation for a 4 fs FWHM, 525 eV photon energy and an intensity of $10^{17}\,\mathrm{Wcm}^{-2}$ FEL pulse. The pathway before the dissociation, D, is the molecular pathway of ionisation

We can see from this table that the primary contributions to the N and N^+ ion yields are from $P_C A_{VV} D$ pathway. In this pathway, a core hole is created by the P_C transition and this hole is then filled in via Auger decay. The resultant N_2^{2+} state then dissociates into either $N^+ + N^+$ or $N^{2+} + N$ with no core holes. As only one core hole is created in this pathway, no DCH states are accessed. This is consistent with what we see in Fig. 5.5 where there are negligible contributions to these ion yields

from DCH states. Conversely, the N^{2+}, N^{3+} and N^{4+} are all dominated by pathways that feature a DCH state, as evidenced by the $P_C P_C$ sequence of transitions. There are also significant contributions to N^{2+} and N^{4+} from pathways that don't involve a DCH state. Indeed, with no DCH states, the pathway $P_C A_{VV} P_C A_{VV} D$ contributes 21% of the population in the N^{2+} yield and the $P_C A_{VV} P_C A_{VV} D P_C A_{VV}$ pathway contributes 9% of the population in the N^{4+} ion yield.

5.7 Electron spectra

While the pathway contributions give us interesting information, they can't be measured experimentally. Instead, we look at the electron spectra for evidence of the transitions that have taken place. In Fig. 5.6, we plot the electron spectra generated by molecular nitrogen interacting with four different FEL pulses at an intensity of 10^{17}Wcm^{-2}. We consider pulses with either 525 eV or 1100 eV photon energy and we consider 4 fs and 80 fs pulse durations for each pulse energy. In (c), the 525 eV 4 fs case, we find a substantial spectral line at 55 eV from photo-ionisations involving DCH states (yellow line), which provides measurable evidence of the formation of a DCH state. There is a larger electron yield at 105 eV from DCH transitions (yellow line), however the overlap with other transitions (green lines) means that this would be difficult to measure experimentally. Comparing (a) and (c), we see that the 525 eV photon energy pulse ionises a lot more electrons than the 1100 eV photon energy pulse. This is due to the higher photon flux and photo-ionisation cross-sections, leading to more photo-ionisations. This creates core holes, which lead to Auger decays and higher-charged molecular states that then dissociate.

Comparing (a) and (b) or (c) and (d), reveals the effect of increasing the pulse duration. The longer pulse duration increases the overall number of transitions. It also causes a large increase in atomic photo-ionisation and Auger transitions, as the longer pulse duration allows transitions to continue after the dissociation has taken place. An additional effect that we note, when comparing (c) and (d), is the reduced DCH photo-electron yield for the longer pulse. This effect is due to the slow build up of intensity in the 80 fs case, which allows the SCH states to Auger decay before
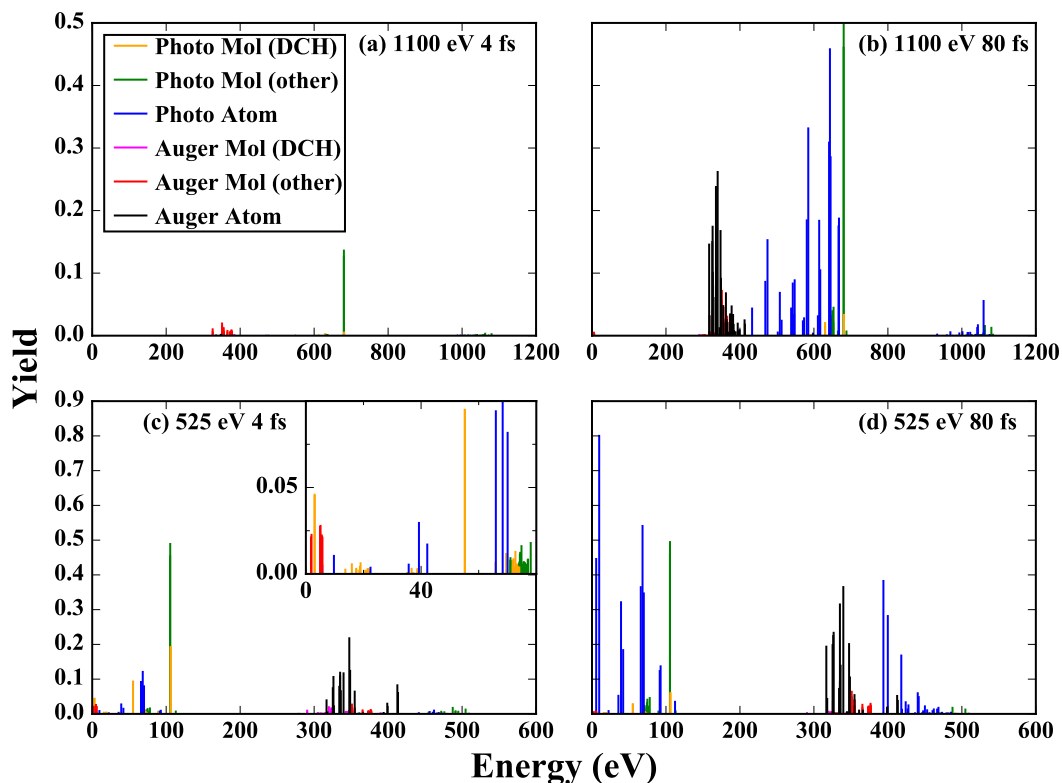
Figure 5.6: Electron spectra produced by the interaction of N_2 with FEL pulses at an intensity of 10^{17} Wcm^{-2} with various pulse parameters.

the necessary intensity for DCH states is reached. Conversely, if we compare (a) and (b), there is a larger contribution to DCH photo-electron yield in the 80 fs case (yellow lines). In this case, the effects of increasing the total photon flux are much larger than the effects of the depopulation during the intensity build up.

5.8 Summary

In this chapter, we investigated the interaction of molecular nitrogen with FEL radiation. We computed molecular continuum orbitals in the single-centre expansion scheme and used these orbitals to compute the Auger rates and single-photon ionization cross-sections for molecular nitrogen. Formulating rate equations for all energetically accessible molecular and atomic transitions, we investigated the dependence of the final ion yields on the parameters of the FEL pulse. Moreover, we studied the contribution of the DCH molecular states to the final atomic ion yields. We found that for a relatively small photon energy of 525 eV, DCH molecular states

contribute significantly to the formation of the final atomic ion fragments at intermediate intensities. For an FEL pulse with 1100 eV photon energy, we find that a much higher intensity is needed in order for the DCH molecular states to significantly contribute to the final atomic ion fragments. Finally, we computed the contribution of Auger electrons and photo-electrons in the electron spectra. Our results show that the electrons removed by single-photon core ionization processes allow us to detect the formation of DCH molecular states in the electron spectra.

Chapter 6

Double and triple-core-hole states in molecular nitrogen

In the previous chapter, we calculated the contribution of pathways involving double-core-hole (DCH) states to the final atomic ion yields generated by molecular nitrogen interacting with an FEL pulse. However, there are two types of DCH states in molecules. Single-site double-core-hole states (SSDCH), with both core holes on the same site and two-site double-core-hole states (TSDCH), with the core holes on different sites. TSDCH states are of particular interest as they are very sensitive to their chemical environment [13, 14, 15, 16]. These states have been the subject of a significant amount of experimental work [17, 18, 19, 20, 21]. There have also been theoretical studies which calculate the contribution of TSDCH states to the final ion yields by treating each atom in the molecule independently [22, 23].

To understand the production and detection of these states, we again model the interaction of molecular nitrogen with an FEL pulse using molecular orbitals. In this chapter, we determine the percentage of the population of each DCH state that is in either a TSDCH or a SSDCH state. We also calculate the percentage of the population which accesses triple-core-hole (TCH) states, which, in molecular nitrogen, will always contain core holes on both atomic sites.

6.1 Projection of delocalized molecular orbitals onto orbitals localized on atomic sites

As in section 5, we use molecular orbitals to obtain the final atomic ion yields and the populations of the pathways from the rate equations. We note that the use of molecular bound state orbitals is important for obtaining electron spectra. Indeed, it has been shown that with high-resolution electron spectroscopy one can observe the energy splitting of the molecular core-hole states $1\sigma_g$ and $1\sigma_u$ [54, 56, 100, 101]. In order to determine whether a pathway accesses a TSDCH molecular state or a SSDCH molecular state during the interaction of N_2 with an FEL pulse, it is necessary at each time step of the propagation to project the delocalized inner-shell molecular orbitals onto inner-shell orbitals localized on atomic sites. We denote the DCH molecular states that involve the inner-shell molecular orbitals $1\sigma_g$ and $1\sigma_u$ by $|1\sigma_g 1\sigma_g\rangle$, $|1\sigma_g 1\sigma_u\rangle$, $|1\sigma_u 1\sigma_g\rangle$ and $|1\sigma_u 1\sigma_u\rangle$.

The delocalized molecular orbitals are expressed in terms of orbitals localized on atomic sites by $|1\sigma_g\rangle = \frac{1}{\sqrt{2}}(|1s_a\rangle + |1s_b\rangle)$ and $|1\sigma_u\rangle = \frac{1}{\sqrt{2}}(|1s_a\rangle - |1s_b\rangle)$ where $|1s_a\rangle$ and $|1s_b\rangle$ are $|1s\rangle$ orbitals localized on the atomic sites a and b of N_2, respectively. At every time step, we check whether a DCH molecular state $|1\sigma_g 1\sigma_g\rangle$, $|1\sigma_g 1\sigma_u\rangle$ or $|1\sigma_u 1\sigma_u\rangle$ has been accessed. Expressing the DCH molecular state $|1\sigma_g 1\sigma_g\rangle$ in terms of orbitals localized on atomic sites, we obtain the following:

$$|1\sigma_g 1\sigma_g\rangle = \frac{1}{2}\left[|1s_a\rangle|1s_a\rangle + |1s_a\rangle|1s_b\rangle + |1s_b\rangle|1s_a\rangle + |1s_b\rangle|1s_b\rangle\right], \qquad (6.1)$$

$$|\langle 1s_a 1s_a|1\sigma_g 1\sigma_g\rangle|^2 = |\langle 1s_a 1s_b|1\sigma_g 1\sigma_g\rangle|^2$$
$$= |\langle 1s_b 1s_a|1\sigma_g 1\sigma_g\rangle|^2 = |\langle 1s_b 1s_b|1\sigma_g 1\sigma_g\rangle|^2 = \frac{1}{4}. \qquad (6.2)$$

Thus, the formation of a DCH molecular state $|1\sigma_g 1\sigma_g\rangle$ corresponds to 50% probability of accessing a SSDCH molecular state, i.e. the $|1s_a 1s_a\rangle$ or the $|1s_b 1s_b\rangle$ state, and 50% probability of accessing a TSDCH molecular state, i.e. the $|1s_a 1s_b\rangle$ or the

$|1s_b 1s_a\rangle$ state. One can show that the same probabilities are obtained for the DCH molecular state $|1\sigma_u 1\sigma_u\rangle$.

Next, we show that the DCH molecular state $|1\sigma_g 1\sigma_u\rangle$ corresponds to different probabilities of accessing a SSDCH molecular state versus a TSDCH molecular state depending on the spin of the state. Denoting by S and T the spatial part of a singlet or triplet DCH molecular state, respectively, we obtain

$$|1\sigma_g 1\sigma_u\rangle^{S/T} = \frac{1}{\sqrt{2}} \left(|1\sigma_g\rangle |1\sigma_u\rangle \pm |1\sigma_u\rangle |1\sigma_g\rangle \right). \tag{6.3}$$

Expressing the spatial part of the DCH molecular state $|1\sigma_g 1\sigma_u\rangle^T$ in terms of orbitals localized on the atomic sites, we obtain

$$|1\sigma_g 1\sigma_u\rangle^T = \frac{1}{\sqrt{2}} \left(|1s_b\rangle |1s_a\rangle - |1s_a\rangle |1s_b\rangle \right), \tag{6.4}$$

and

$$|\langle 1s_a 1s_b|^T |1\sigma_g 1\sigma_u\rangle^T|^2 = 1. \tag{6.5}$$

and, thus, this state corresponds to 100% probability of occupying a TSDCH molecular state. Similarly, expressing the DCH molecular state $|1\sigma_g 1\sigma_u\rangle^S$ in terms of orbitals localized on the atomic sites, we obtain:

$$|1\sigma_g 1\sigma_u\rangle^S = \frac{1}{\sqrt{2}} \left(|1s_a\rangle |1s_a\rangle - |1s_b\rangle |1s_b\rangle \right), \tag{6.6}$$

$$|\langle 1s_a 1s_a|1\sigma_g 1\sigma_u\rangle^S|^2 = |\langle 1s_b 1s_b|1\sigma_g 1\sigma_u\rangle^S|^2 = \frac{1}{2}. \tag{6.7}$$

and, thus, this state corresponds to 100% probability of occupying a SSDCH molec-

ular state. Taking into account that a DCH molecular state has 75% probability to be in the $|1\sigma_g 1\sigma_u\rangle^T$ state and 25% to be in the $|1\sigma_g 1\sigma_u\rangle^S$ state, based on the multiplicities of the singlet and triplet states [61], it follows that the DCH state $|1\sigma_g 1\sigma_u\rangle$ has 75% probability to access a TSDCH molecular state and 25% probability to access a SSDCH molecular state. The above probabilities are incorporated at every time step of our computations in order to calculate the probability of pathways that access TSDCH and SSDCH molecular states during the interaction of N_2 with an FEL laser pulse.

6.2 Electron spectra
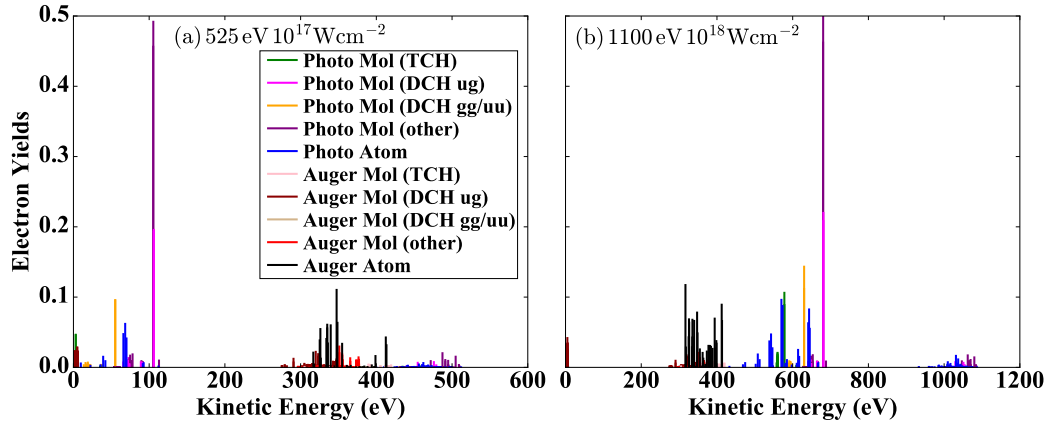
Figure 6.1: Electron spectra resulting from the interaction of N_2 with a 4 fs FWHM FEL pulse (a) with 525 eV photon energy and peak intensity of 10^{17} Wcm^{-2} and (b) with 1100 eV photon energy and peak intensity of 10^{18} Wcm^{-2}. DCH ug denotes transitions involving states with a $1\sigma_g$ electron and a $1\sigma_u$ electron missing. DCH gg/uu denotes the electron yield from transitions involving a state with two $1\sigma_g$ or two $1\sigma_u$ electrons missing. Photo Mol (nCH) and Auger Mol (nCH), with n the number of core holes, denote single-photon ionisation and Auger transitions, respectively, that involve molecular states with no more than n core holes. The label "other" refers to transitions that involve molecular states with either no core holes or a single core hole.

Using the rate equations, we calculate the electron spectra of all atomic and molecular transitions for N_2 interacting with two different FEL pulses. In Fig. 6.1 (a) we show the electron spectra produced by a 10^{17} Wcm^{-2}, 4 fs FEL pulse with 525 eV photon energy. The pulse in Fig. 6.1 (b) also has a 4 fs duration, but has 1100 eV photon energy and a peak intensity of 10^{18} Wcm^{-2}. We choose this duration be-

cause our calculations are most accurate for short duration and high intensity pulses, as we treat the nuclear motion via transitions in the rate equations, as described in section 5.3. Importantly, this pulse duration is experimentally accessible [55]. The 10^{17} Wcm^{-2} and 10^{18} Wcm^{-2} intensities are chosen as they produce large electron yields for transitions involving DCH states. In both cases, the transitions that involve a $|1\sigma_g 1\sigma_u\rangle$ state or a TCH molecular state can not be easily discerned. These transitions would give the strongest evidence of the production of states with core holes on more than one site. We can discern electron yields corresponding to transitions involving a $|1\sigma_g 1\sigma_g\rangle$ or a $|1\sigma_u 1\sigma_u\rangle$ DCH state at 55 eV kinetic energy for the 525 eV FEL pulse and at 630 eV for the 1100 eV FEL pulse. Unfortunately, these DCH states are TSDCH states in only 50% of cases and SSDCH states otherwise. This means that the electron spectra cannot give evidence of the production of a state with core holes on more than one atomic site. However, if we performed these calculations accounting for fine structure we find, from eqn (6.5) and eqn (6.7), that the electron spectra could give evidence of TSDCH states.

6.3 Ion yields

We calculate the ion yields produced by the interaction of molecular nitrogen with an FEL using the rate equations. To determine the contributions from different types of core hole states, we keep track of the population in each state that came via a SCH, SSDCH, TSDCH or TCH state. We then compile this into ion yields, split by the different type of core hole state.

6.3.1 Comparison with experimental and theoretical results

In Fig. 6.2, we compute the atomic ion yields produced by an FEL pulse interacting with molecular nitrogen for three different pulses with various pathways closed. The yields are compared with experimental values [55] and another computational work [23], which treats the molecule as two independent atoms. Using the method outlined in section 5.4, we calculate the FEL flux on a grid of area 10 μm by 10 μm, with 31 points in the x direction and 31 points in the y direction, and use these values to obtain the atomic ion yields. We then integrate these ion yields over the

area and normalise such that the sum of the charged atomic ion yields is 1. We then compare this integrated ion yield with the experimental and theoretical work.
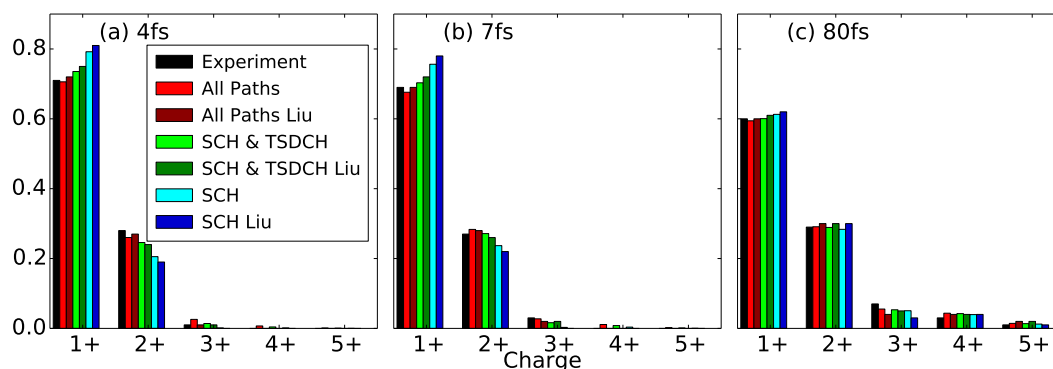
Figure 6.2: Atomic ion yields for molecular nitrogen interacting with FEL pulses of (a) pulse energy 0.15 mJ with 4 fs FWHM and 77% loss (b) pulse energy 0.26 mJ with 7 fs FWHM and 84% loss (c) pulse energy 0.26 mJ with 80 fs FWHM and 70% loss. Our results are compared with the experimental results in Ref. [23, 55]. Atomic ion yields are obtained with all pathways accounted for as well as with certain pathways excluded and are compared with other theoretical results [23].

In Fig. 6.2, we have calculated the atomic ion yields with all pathways allowed (red) and they compare very well with the experimental yields [55] (black) and the other computational work [23] (dark red). We also compare the atomic ion yields generated by pathways that only involve SCH molecular states (light blue) with the equivalent calculation from the other computational work (dark blue) and again we find a good agreement. The ion yields generated by only the SCH and TSDCH pathways are also calculated and our values (light green) compare well with other calculations (dark green) that have the same pathways restricted. This suggests that we correctly account for the percentage of the population that passes through a TSDCH state.

We find that the yields calculated with multiple-core-hole pathways restricted have lower high-charge ion yields and the N^+ ion yield increases as we exclude more pathways. This is expected as the pathways that involve multiple-core hole states will primarily populate the higher-charged atomic ion yields. This effect is diminished in the 80 fs case (c) because the multiple-core-hole pathways have lower contributions in longer pulses.

6.3.2 Contribution of SSDCH, TSDCH and TCH molecular states in atomic ion yields.
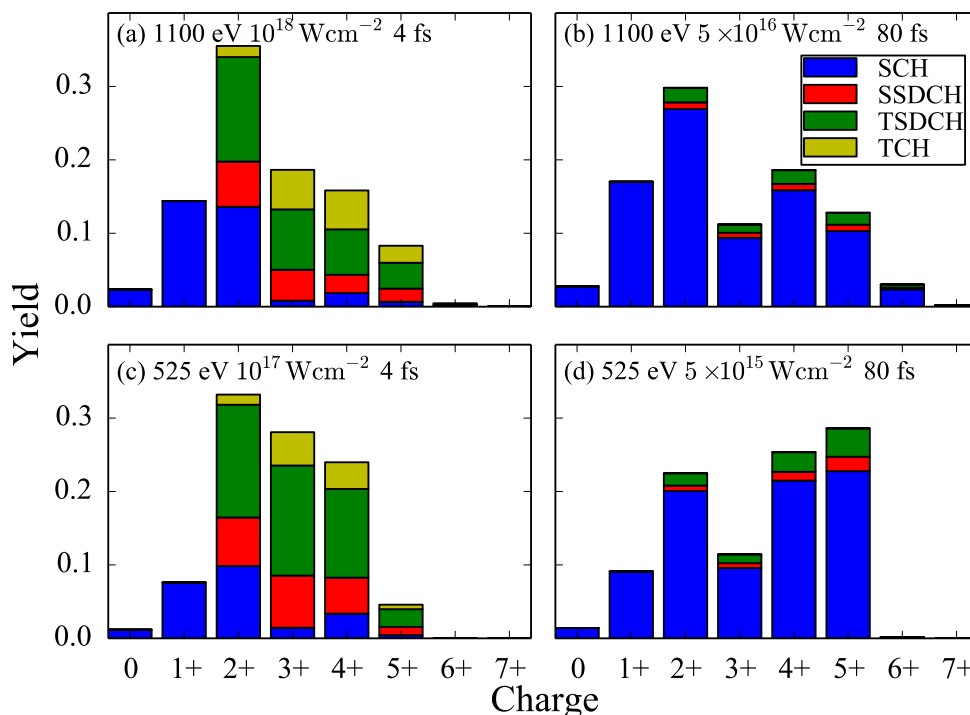
Figure 6.3: Atomic ion yields produced by various FEL pulses interacting with molecular nitrogen. The ion yields are split into the contributions of pathways accessing SCH, SSDCH, TSDCH and TCH molecular states.

In Fig. 6.3, for different FEL pulses, we compute the final atomic ion yields as well as the contribution of SCH, TSDCH, SSDCH and TCH molecular states to each of the final atomic ion yields. In Fig. 6.3 (a) and (c), we find that for short duration, 4 fs FWHM, and high intensity FEL pulses, 49% and 56% of all pathways contributing to all final atomic ion yields are pathways that have accessed TSDCH and TCH molecular states. Moreover, we find that the contribution of pathways that access TSDCH and TCH molecular states increases for higher-charged atomic ion states. The is because the contribution of pathways where two single-photon ionizations take place sequentially, i.e. before an Auger process takes place following the first single-photon ionization, is larger for atomic ions N^{3+} and N^{4+} compared to N^{2+}. For instance, the contribution of pathways that have accessed SSDCH, TSDCH or TCH molecular states account for roughly 90% of the N^{5+} yield for the

short duration and intense FEL pulses, see Fig. 6.3(a) and (c). For the long duration of 80 fs FWHM and small intensity FEL pulses, we find that no more than 10% of all pathways contributing to the atomic ion yields are pathways that have accessed SSDCH, TSDCH and TCH molecular states. In addition, the atomic ion yields of the higher-charged states have much larger values for the 80 fs pulse rather than for the 4 fs FWHM FEL pulse. This is reasonable since for the long duration FEL pulse more single-photon ionization processes take place leading to the formation of higher charged atomic ions.

6.4   Dependence of DCH and TCH molecular states on intensity.
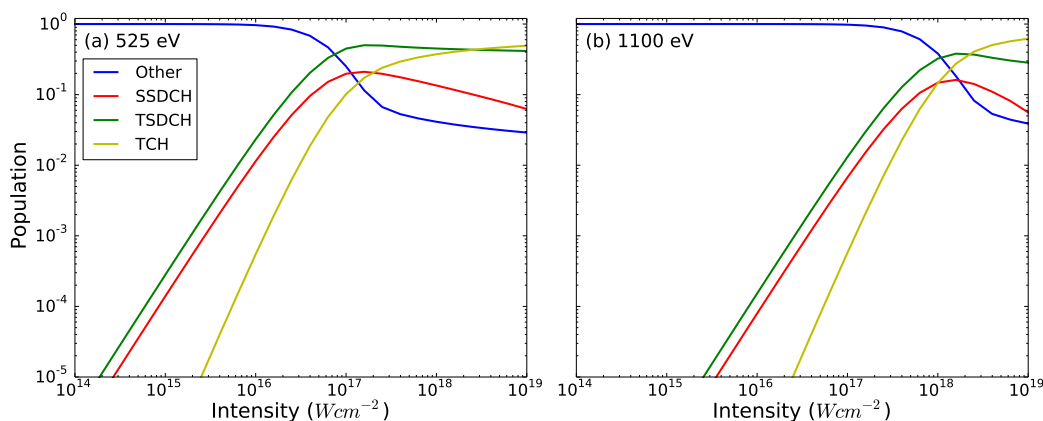
Figure 6.4: Proportion of populations that access different core-hole states of N_2 when driven with a 4 fs FWHM and 525 eV (a) or 1100 eV (b) FEL pulse as a function of intensity.

In Fig. 6.4, we plot the population of pathways that accesses SCH, SSDCH, TSDCH and TCH molecular states as a function of intensity for a 4 fs FEL pulse for 525 eV photon energy (a) and for 1100 eV photon energy (b). We find that for the 525 eV (1100 eV) FEL pulse most of the population accesses multiple-core-hole molecular states for intensities above 10^{17} Wcm^{-2} (10^{18} Wcm^{-2}). The intensity is higher for the higher photon energy pulse since the single-photon ionisation cross sections are higher for the smaller photon energy FEL pulse. Moreover, we find that the contribution of TCH molecular states compared to TSDCH molecular states is

higher for the 1100 eV rather than for the 525 eV FEL pulse for high intensities. The reason for this, is that more molecular states are energetically accessible with the 1100 eV photon energy FEL pulse.

6.5   Summary

Extending the theoretical framework of Chapter 5, we have computed the contribution to the final atomic ion yields of pathways that access SSDCH, TSDCH and TCH molecular states. We have identified the most effective duration and intensity of a 525 eV and a 1100 eV FEL pulse in order to maximize the contribution of pathways that access SSDCH, TSDCH and TCH molecular states. Future work including the effects of fine structure could allow us to explicitly detect TSDCH or SSDCH states, based on section 6.1.

Chapter 7

Conclusion

In this dissertation, we explored the interplay of single-photon ionisations and Auger transitions that take place due to a free-electron laser (FEL) interaction with an atom or molecule. To understand the transitions that occur during such an FEL interaction, we modelled this process computationally using rate equations. To account for the transitions in these models, it was necessary to calculate the Auger rates and photo-ionisation cross-sections for all accessible transitions. We also considered the effects of dissociative transitions in our molecular model. These models allowed us to investigate the formation of multiple-core-hole states that are produced by sequential core single-photon ionisations. We have addressed why these states are interesting and their potential use as a basis for spectroscopic measurements.

To better understand the interplay of photo-ionisation and Auger decay, as well as to create the groundwork for further work, we began by modelling FEL interactions with atoms. This involved calculating Auger and photo-ionization transition rates and using these rates to construct a set of rate equations. The spherical symmetry of atoms implies that these calculations were computationally and conceptually simpler than their molecular equivalents. Using our model of atomic interactions with FEL pulses, we were able to calculate the ion yields and electron spectra produced by argon interacting with various FEL pulses. Using the ion yields, we were able to observe the difference between the population of odd and even-charged ions of argon. Further, by calculating the pathway populations, we found that this was

caused by the combination of core photo-ionisation and Auger decay transitions. We investigated how the odd-even disparity changed with increasing photon energy and found that the number of energetically-accessible core ionisations determined the extent of this pattern. We found that, for the pulses we considered, the odd-even disparity extended up to ion yields with charge equal to twice the number of core holes available. However, as we increased the photon energy, we also saw the emergence of Coster-Kronig transitions. By considering the pathways through which the ion yields are reached, we could see the effect of these Coster-Kronig transitions in populating odd-charged ion yields, reducing the difference between the odd and even-charged ion yields.

After computing FEL transitions with atoms, we studied FEL transitions with molecules. We calculated the single-photon ionisation cross-sections and the Auger decay rates using molecular bound and continuum orbital wavefunctions. By computing the molecular continuum orbital wavefunctions, our calculations should be more accurate that calculations using atomic continuum orbital wavefunctions. The use of molecular continuum orbitals should be most relevant for transitions that emit low energy electrons, as these electrons will spend more time in the molecular potential. To account for the breakdown of the molecular ions, we introduced dissociative transitions, in addition to the Auger and photo-ionization transitions. The molecular model was much more involved computationally and theoretically due to the non-spherical symmetry of the molecular orbitals, necessitating the use of single-centre-expansions to express the wavefunctions in terms of components with well-defined angular momentum. With the techniques described in chapter 5, we were able to determine the atomic and molecular ion yields produced in these interactions, as well as the electron spectra emitted. We found that the atomic ion yields we obtained had very good agreement with experiments. By varying our pulse, we also investigated the effects, on the ion yields, of changing the intensity, pulse length and photon energy. We found that long high-intensity pulses produced more highly-charged ions than short or low-intensity pulses. We also found that the pulses with photon energy closer to the core ionisation energies produced signifi-

cantly more highly-charged ions than the pulses with a higher photon energy, for a given intensity and length.

In addition, we were able to calculate how the molecular population transitioned through different intermediate states to reach these final states. These pathway calculations allowed us to determine the proportion of the population which accesses unstable short-lived states, in particular the ones containing multiple core holes. We found that the proportion of the population which accessed double-core-hole states was highly dependent on the intensity and the photon energy. High intensity and low photon energy significantly increased the proportion of the population which accessed these states with two core holes.

With the projection onto localised atomic orbitals, described in chapter 6, we determined the proportion of the population which accessed two-site or single-site double-core-hole states. This allowed us to determine the percentage of the population that accessed states with a core hole on each atomic site. As expected, we found that this percentage was greatest for short, high intensity pulses with low photon energy. However, due to the nature of this projection, we were unable to provide an observable which would allow the detection of these states.

The aim of this thesis has been to study the production and detection of multiple-core-hole states resulting from FEL interactions with atoms and molecules. By using the pathway rate equations, we were able to ascertain the proportion of the population that accesses various core-hole states in atoms and molecules. By varying the pulse parameters, we could also investigate the conditions which favour the production of these states. By calculating the electron spectra produced in FEL interactions with matter, we also determined observable values which indicate the production of various multiple-core-hole states. However, due to the nature of our model, the subset of these states with the most interest [13, 14], two-site double-core-hole states, could not be explicitly detected using our methods.

In future work, we will build on this model by accounting for the nuclear motion of the molecule and treating the dissociative transitions as a gradual process changing the internuclear separation of the molecule. This will require post-

Hartree-Fock techniques for calculating the molecular wavefunctions, as HF methods are inaccurate at large inter-nuclear distances. These post-Hartree-Fock techniques mean that we will work with more complex wavefunctions and would pose additional computational and conceptual challenges. However, they will also give more accurate wavefunctions and allow us to calculate the wavefunctions during dissociation.

As mentioned in chapter 6, it would also be interesting to include the effects of fine-structure in our wavefunction calculations. While we have summed over the different spin combinations in this work, there are differences in the Auger rates for triplet and singlet states and accounting for this would improve our model. In addition, the inclusion of fine-structure would allow us to uniquely identify whether double-core-hole states had core holes on one or two atomic sites from their delocalised wavefunctions. This would allow us to use the electron spectra produced by our model as an indicator of the production of two-site double-core-hole states.

An additional area of interest for future work is the modelling of different molecular interactions with FEL pulses. In this work, we have considered only one molecule, diatomic nitrogen. While our model was designed to work with homonuclear diatomic molecules, by making modifications to our model, we could simulate the interactions of a variety of molecules with FEL pulses.

Appendix A

Molecular continuum wavefunction calculations

The molecular single-centre coefficients (SCCs) of a molecular continuum wavefunction are found by solving eqn (4.6). This equation depends on three components, the electron-nuclei interaction, $V_{lm,l'm'}^{ne}(r)$, the direct interaction, $J_{lm,l'm'}^{ee}(r)$ and the exchange interaction $X_{lm}[\hat{P}_\varepsilon](r)$. In section 4.3, we summarised these components, but did not offer a derivation of the terms. Below, we detail the full derivation of the components.

A.1 Electron-nuclei interaction

This term describes the Coulomb attraction between the positively-charged nuclei and the negatively-charged electrons. From eqn (4.6), we can write this component as

$$V_{lm,l'm'}^{ne}(r) = \int Y_{lm}^*(\theta,\phi) \sum_{\alpha}^{nuc.} \frac{(-Z_\alpha)}{|\mathbf{r} - \mathbf{R}_\alpha|} Y_{l'm'}(\theta,\phi) d\Omega, \tag{A.1}$$

where Z_α is the charge of the nucleus α and $\mathbf{R}_\alpha$ its position in space. Substituting

the Laplace multipole expansion [94]:

$$\frac{1}{|\mathbf{r} - \mathbf{R}_\alpha|} = \sum_{kq} \frac{4\pi}{2k+1} \frac{r_<^k}{r_>^{k+1}} Y_{kq}(\theta, \phi) Y_{kq}^*(\theta_\alpha, \phi_\alpha), \tag{A.2}$$

where $r_< = \min(r, R_\alpha)$ and $r_> = \max(r, R_\alpha)$, in eqn. (A.1) results in,

$$V_{lm,l'm'}^{ne}(r) = -\sum_\alpha^{nuclei} Z_\alpha \sum_{kq} \frac{4\pi}{2k+1} \frac{r_<^k}{r_>^{k+1}} Y_{kq}^*(\theta_\alpha, \phi_\alpha) \int Y_{lm}^*(\theta, \phi) Y_{kq}(\theta, \phi) Y_{l'm'}(\theta, \phi) d\Omega, \tag{A.3}$$

The integral over three spherical harmonics is given by [94],

$$\int Y_{lm}(\theta, \phi) Y_{kq}(\theta, \phi) Y_{l'm'}(\theta, \phi) d\Omega = \sqrt{\frac{(2l+1)(2k+1)(2l'+1)}{4\pi}} \\ \times \begin{pmatrix} l & k & l' \\ 0 & 0 & 0 \end{pmatrix} \begin{pmatrix} l & k & l' \\ m & q & m' \end{pmatrix}, \tag{A.4}$$

where double row of triples in brackets denote Wigner-3j symbols [60]. Using $Y_{lm}^*(\theta, \phi) = (-1)^m Y_{l-m}(\theta, \phi)$, eqn. (A.4) and eqn. (A.3) can be written as

$$V_{lm,l'm'}^{ne}(r) = -\sum_\alpha^{nuclei} Z_\alpha (-1)^m \sqrt{(2l+1)(2l'+1)} \\ \times \sum_{kq} \begin{pmatrix} l & k & l' \\ 0 & 0 & 0 \end{pmatrix} \begin{pmatrix} l & k & l' \\ -m & q & m' \end{pmatrix} \sqrt{\frac{4\pi}{2k+1}} Y_{kq}^*(\theta_\alpha, \phi_\alpha) \frac{r_<^k}{r_>^{k+1}}, \tag{A.5}$$

thus obtaining the general expression for $V_{lm,l'm'}^{ne}(r)$.

A.2 Direct interaction

From eqn. (4.6), the direct interaction term is,

$$J_{lm,l'm'}(r) = \int Y_{lm}^*(\theta,\phi) \sum_i a_i \int d\mathbf{r}' \frac{\phi_i(\mathbf{r}')\phi_i^*(\mathbf{r}')}{|\mathbf{r}-\mathbf{r}'|} Y_{l'm'}(\theta,\phi)d\Omega. \tag{A.6}$$

With the use of the Laplace expansion in eqn (A.2), the above expression becomes

$$J_{lm,l'm'}(r) = \sum_i a_i \sum_{\substack{l_2m_2,l_3m_3,\\kq}} \frac{4\pi}{2k+1} \int Y_{l_2m_2}^*(\theta',\phi')Y_{kq}(\theta',\phi')Y_{l_3m_3}(\theta',\phi')d\Omega'$$
$$\times \int Y_{lm}^*(\theta,\phi)Y_{kq}^*(\theta,\phi)Y_{l'm'}(\theta,\phi)d\Omega \int_0^\infty \frac{r_<^k}{r_>^{k+1}} P_{i,l_2m_2}^*(r')P_{i,l_3m_3}(r')dr'. \tag{A.7}$$

Using $Y_{lm}^*(\theta,\phi) = (-1)^m Y_{l-m}(\theta,\phi)$ and eqn (A.4), we obtain

$$J_{lm,l'm'}(r) = \sum_i a_i \sum_{\substack{l_2m_2,l_3m_3,\\kq}} (-1)^{m+m_2+q} \sqrt{(2l+1)(2l'+1)(2l_2+1)(2l_3+1)}$$
$$\times \begin{pmatrix} l_2 & k & l_3 \\ 0 & 0 & 0 \end{pmatrix} \begin{pmatrix} l_2 & k & l_3 \\ -m_2 & q & m_3 \end{pmatrix} \begin{pmatrix} l & k & l' \\ 0 & 0 & 0 \end{pmatrix} \begin{pmatrix} l & k & l' \\ -m & -q & m' \end{pmatrix} \tag{A.8}$$
$$\times \int_0^\infty \frac{r_<^k}{r_>^{k+1}} P_{i,l_2m_2}^*(r')P_{i,l_3m_3}(r')dr'.$$

Using the following symmetry relations [60]

$$\begin{pmatrix} l & k & l' \\ m & q & m' \end{pmatrix} = (-1)^{l+k+l'} \begin{pmatrix} l & k & l' \\ -m & -q & -m' \end{pmatrix} \tag{A.9}$$

and

$$
\begin{pmatrix} l & k & l' \\ m & q & m' \end{pmatrix} = (-1)^{l+k+l'} \begin{pmatrix} k & l & l' \\ q & m & m' \end{pmatrix},
\tag{A.10}
$$

eqn (A.8) can be rewritten as

$$
J_{lm,l'm'}(r) = \sum_i a_i \sum_{\substack{l_2 m_2, l_3 m_3, \\ kq}} (-1)^{m_2 + m'} \sqrt{(2l+1)(2l'+1)(2l_2+1)(2l_3+1)}
$$

$$
\times \begin{pmatrix} l_2 & k & l_3 \\ 0 & 0 & 0 \end{pmatrix} \begin{pmatrix} l_2 & k & l_3 \\ -m_2 & q & m_3 \end{pmatrix} \begin{pmatrix} l' & k & l \\ 0 & 0 & 0 \end{pmatrix} \begin{pmatrix} l' & k & l \\ -m' & q & m \end{pmatrix}
\tag{A.11}
$$

$$
\times \int_0^\infty \frac{r_<^k}{r_>^{k+1}} P_{il_2 m_2}^*(r') P_{il_3 m_3}(r') dr'.
$$

Here, we have used $q = m' - m$ to simplify the expression for the sign. This follows as the bottom row of all non-zero Wigner-3j symbols must equal zero [60].

A.3 Exchange interaction

The exchange interaction [102] is a quantum mechanical effect that takes into account the interaction of different spin symmetries. All two-electron wavefunctions must be anti-symmetric, as electrons are fermions [103]. This means that the spin symmetry will determine the spatial symmetry and the different spatial symmetries will have different energies. Anti-symmetric spatial wavefunctions will tend to zero as the separation goes to zero. As a result the expectation value of the distance between these electrons will be higher than in the case with a symmetric spatial wavefunction. Thus, a triplet state has lower energy than a singlet.

The exchange interaction has the effect of a non-local potential [104]. This means that the potential acting on the electron depends on the wavefunction of the electron at all points in the region of the non-locality [105]. Mathematically, we define the contribution of the exchange interaction with a functional of the continuum

orbital wavefunction. As the continuum orbital depends on the energy, the contribution of the exchange interaction is also energy dependent. The exchange term is given by

$$X_{lm}[\hat{P}_\varepsilon](r) = \int Y_{lm}^*(\theta,\phi) \sum_{l'm'} \sum_i^{orb.} b_i \int d\mathbf{r}' \frac{\phi_i^*(\mathbf{r}') P_{\varepsilon l'm'}(r')}{|\mathbf{r}-\mathbf{r}'|} \phi_i(\mathbf{r}) Y_{l'm'}(\theta',\phi') d\Omega.$$

(A.12)

Expressing the bound wavefunctions using a SCE and using eqn (A.2), we can express the exchange term as

$$X_{lm}[\hat{P}_\varepsilon](r) = \sum_{l'm'} \sum_i^{orb.} b_i \sum_{\substack{l_2 m_2, l_3 m_3, \\ kq}} \frac{4\pi}{2k+1} \int Y_{l_2 m_2}^*(\theta',\phi') Y_{kq}(\theta',\phi') Y_{l'm'}(\theta',\phi') d\Omega'$$

$$\times \int Y_{lm}^*(\theta,\phi) Y_{kq}^*(\theta,\phi) Y_{l_3 m_3}(\theta,\phi) d\Omega$$

$$\times \int_0^\infty \frac{r_<^k}{r_>^{k+1}} P_{il_2 m_2}^*(r') P_{\varepsilon l'm'}(r') dr' P_{il_3 m_3}(r).$$

(A.13)

Again using eqn (A.4) and the properties of Wigner-3j symbols given in the previous section (eqn (A.9) and eqn (A.10)), the above expression can be written as

$$X_{lm}[\hat{P}_\varepsilon](r) = \sum_{l'm'} \sum_i^{orb.} b_i \sum_{\substack{l_2 m_2, l_3 m_3, \\ kq}} (-1)^{m_2+m_3} \sqrt{(2l+1)(2l'+1)(2l_2+1)(2l_3+1)}$$

$$\times \begin{pmatrix} l_2 & k & l' \\ 0 & 0 & 0 \end{pmatrix} \begin{pmatrix} l_2 & k & l' \\ -m_2 & q & m' \end{pmatrix} \begin{pmatrix} l_3 & k & l \\ 0 & 0 & 0 \end{pmatrix} \begin{pmatrix} l_3 & k & l \\ -m_3 & q & m \end{pmatrix}$$

$$\times \int_0^\infty \frac{r_<^k}{r_>^{k+1}} P_{il_2 m_2}^*(r') P_{\varepsilon l'm'}(r') dr' P_{il_3 m_3}(r).$$

(A.14)

It is clear when looking at the radial term in eqn (A.14) that the exchange inter-

action depends on the value of the continuum electron wavefunction at all r and is hence non-local. Two methods of solving the Hartree-Fock equation, eqn (4.6), are the iterative method, in which $P_{\varepsilon l'm'}(r)$ is found and then substituted back into the equation until it converges, and the non-iterative method, which is explained in section 4.4.

Appendix B

Hartree-Fock direct and exchange coefficients

In the Hartree-Fock framework, after applying the variational principle [64], the electron-electron interaction terms can be written as

$$\sum_i^{orbs} a_i J_i \phi_\varepsilon - \sum_i^{orbs} b_i K_i \phi_\varepsilon = \varepsilon^{ee} \phi_\varepsilon, \tag{B.1}$$

where ϕ_ε is the spin-orbital of the molecular continuum electron with spin orientation μ_ε and ε^{ee} is the energy contribution of the electron-electron interaction terms. The index i refers to a bound molecular orbital and J_i and K_i are defined as

$$J_i \phi_\varepsilon = \langle \phi_i | \frac{1}{r_{12}} | \phi_i \rangle \phi_\varepsilon \tag{B.2}$$

$$K_i \phi_\varepsilon = \langle \phi_i | \frac{1}{r_{12}} | \phi_\varepsilon \rangle \phi_i.$$

To obtain the a_i and b_i coefficients in the general case, it suffices to obtain a_i and b_i for three limiting cases. Since we consider molecular orbitals in all three limiting cases, the electron occupancy of the shells involved is zero, one or two. If a shell is not occupied, the coefficients a_i and b_i are zero. For the first limiting case, a two-electron system is considered, with both electrons initially occupying a single shell i and one of these electrons finally being emitted to the continuum. Spin is conserved and it is equal to zero in the initial and final states. Therefore, a two-

electron wavefunction must be constructed that is anti-symmetric in spin and anti-symmetric under exchange of electrons. Such a wavefunction is given as a sum of the following two Slater determinants

$$\Phi(\mathbf{r}_1, \mathbf{r}_2) = \frac{1}{\sqrt{2}} \left(\frac{1}{\sqrt{2!}} \begin{vmatrix} \phi_i^\uparrow(\mathbf{r}_1) & \phi_\varepsilon^\downarrow(\mathbf{r}_1) \\ \phi_i^\uparrow(\mathbf{r}_2) & \phi_\varepsilon^\downarrow(\mathbf{r}_2) \end{vmatrix} - \frac{1}{\sqrt{2!}} \begin{vmatrix} \phi_i^\downarrow(\mathbf{r}_1) & \phi_\varepsilon^\uparrow(\mathbf{r}_1) \\ \phi_i^\downarrow(\mathbf{r}_2) & \phi_\varepsilon^\uparrow(\mathbf{r}_2) \end{vmatrix} \right), \tag{B.3}$$

where $\mathbf{r}_1$ and $\mathbf{r}_2$ are the spatial coordinates of the two electrons. Using spin conservation and exchange symmetry, it is found that the energy contribution of the electron-electron interaction term is given by

$$\varepsilon^{ee} = \langle \Phi | \frac{1}{r_{12}} | \Phi \rangle = \langle \phi_i \phi_\varepsilon | \frac{1}{r_{12}} | \phi_i \phi_\varepsilon \rangle + \langle \phi_i \phi_\varepsilon | \frac{1}{r_{12}} | \phi_\varepsilon \phi_i \rangle. \tag{B.4}$$

Using the variational principle in the Hartree-Fock equations scheme [64] for the continuum orbital, the following equations are obtained

$$J_i \phi_\varepsilon + K_i \phi_\varepsilon = \varepsilon^{ee} \phi_\varepsilon. \tag{B.5}$$

Comparing eqn (B.1) and eqn (B.5), we find that $a_i = 1$ and $b_i = -1$.

Another limiting case involves two shells i and j. In the initial state one electron is in shell i and two electrons occupy shell j. In the final state one electron from the j shell escapes to the continuum. A three-electron wavefunction must be constructed which is anti-symmetric in spin regarding the continuum electron and the electron in the j shell and anti-symmetric under exchange of electrons. Such a wavefunction is given as a linear combination of the following two Slater determinants

$$\Phi(\mathbf{r}_1, \mathbf{r}_2, \mathbf{r}_3) = \frac{1}{\sqrt{2 \times 3!}} \begin{vmatrix} \phi_i^\uparrow(\mathbf{r}_1) & \phi_j^\downarrow(\mathbf{r}_1) & \phi_\varepsilon^\uparrow(\mathbf{r}_1) \\ \phi_i^\uparrow(\mathbf{r}_2) & \phi_j^\downarrow(\mathbf{r}_2) & \phi_\varepsilon^\uparrow(\mathbf{r}_2) \\ \phi_i^\uparrow(\mathbf{r}_3) & \phi_j^\downarrow(\mathbf{r}_3) & \phi_\varepsilon^\uparrow(\mathbf{r}_3) \end{vmatrix} \tag{B.6}$$

$$- \frac{1}{\sqrt{2 \times 3!}} \begin{vmatrix} \phi_i^\uparrow(\mathbf{r}_1) & \phi_j^\uparrow(\mathbf{r}_1) & \phi_\varepsilon^\downarrow(\mathbf{r}_1) \\ \phi_i^\uparrow(\mathbf{r}_2) & \phi_j^\uparrow(\mathbf{r}_2) & \phi_\varepsilon^\downarrow(\mathbf{r}_2) \\ \phi_i^\uparrow(\mathbf{r}_3) & \phi_j^\uparrow(\mathbf{r}_3) & \phi_\varepsilon^\downarrow(\mathbf{r}_3) \end{vmatrix}.$$

Following the same procedure as for the other limiting case, the following equations are obtained

$$\left(J_i - \tfrac{1}{2}K_i + J_j + K_j \right) \phi_\varepsilon = \varepsilon^{ee} \phi_\varepsilon, \tag{B.7}$$

Comparing eqn (B.1) and eqn (B.7), it is found that $a_j = 1$ and $b_j = -1$, while $a_i = 1$ and $b_i = \tfrac{1}{2}$.

The third limiting case involves two electrons occupying shell i and two electrons occupying shell j in the initial state, with one electron from orbital j escaping to the continuum in the final state. Following the same procedure as in the other two cases, it can be shown that $a_i = 2$ and $b_i = 1$ and $a_j = 1$ and $b_j = -1$. In general, for all molecular ion states, in the Hartree-Fock formalism, the occupation coefficients a_i and b_i can be obtained using the above three limiting cases.

Appendix C

Code summaries

C.1 Molecular Auger rate calculation code

The molecular Auger rate equation code calculates the matrix elements as given in eqn (4.85) and combines them as described in eqn (4.88). It calculates the Auger rate for a transition involving a particular degenerate continuum orbital, labelled by L. Breaking down the code like this, allows the calculation to be split up into multiple jobs and reduces the time required. The code reads in the single-centre expansion (SCE) coefficients of the bound and continuum orbitals and splines these, using the `gsl_spline` functionality [106], to obtain the radial wavefunctions. It then performs analytic angular integrals using the `WignerSymbols` package [107] and numeric 2D radial integrals using the `boost` package [108]. Through these functions, it calculates the matrix elements and returns the Auger rate, for a given L, in atomic units. These Auger rates are then compiled using a python script.

C.2 Molecular rate equation code

The molecular rate equation code can calculate either the ion and electron yields or the pathway populations. It reads the atomic and molecular state energies and tables of the atomic and molecular photo-ionisation cross-sections and Auger rates as well as the dissociation rates and uses these to construct a set of rate equations. These rate equation are then solved iteratively using Euler's method [109] with 1.2×10^7 steps between -200 fs and 1000 fs. To calculate the pathway populations, the pathways are first constructed by chaining together transitions. We then construct rate

equations for each of these states and solve them iteratively. We construct the list of pathways as follows:

```
Construct an empty temporary vector of pathways
Add a pathway containing the ground state index to this vector.
Append a 1 to the stored vector of pathway populations,
    as all of the population is in the ground state.
While this temporary vector of pathways is not empty,
->Take the first pathway in the vector.
->Determine the possible transitions from the final state of the pathway.
->For each transition,
->->Create a new pathway as a copy of the pathway.
->->Append the final state index of the transition.
->->Add this new pathway to the temporary vector.
->Add the initial pathway to the vector of stored pathways.
->Add a 0 to the stored vector of pathway populations,
    as all of the non-ground states will be unoccupied initially.
->Remove the initial pathway from the temporary vector.
```

At high photon intensities, a large number of transitions are possible. This means that the number of pathways increases to an unwieldy amount, with 6.6 million pathways for molecular nitrogen ionised by 1100 eV photons. To overcome this difficulty, we split the pathways into branches. The pathways can, by definition, only transition to longer pathways. Therefore, a given branch of pathways starting with a certain set of transitions will be independent of pathways that do not start with that set of transitions. Thus, for a given branch, we include the pathways that form the branch start and all of the pathways which they depopulate to, such that the correct amount of the population will be transferred to the branch start. From this, all pathways that start with the branch start will be included and these pathways will have no dependence on the pathways that are excluded. An example is shown below, for the branch starting with $0 \to 2 \to 5$, where 0, 2 and 5 are hypothetical state indices:

0

$0 \to 1$ X

$0 \to 2$

$0 \to 3$ X

$0 \rightarrow 2 \rightarrow 4$ X

$0 \rightarrow 2 \rightarrow 5$

$0 \rightarrow 2 \rightarrow 6$ X

$0 \rightarrow 2 \rightarrow 5 \rightarrow 7$

$0 \rightarrow 2 \rightarrow 5 \rightarrow 8$

All paths from this point start with $0 \rightarrow 2 \rightarrow 5$

Here, the pathways labelled with an X are included in the rate equation calculation, but discarded at the end as their populations are not properly calculated. By splitting up the pathways in this way, we can separate the rate equations into multiple calculations and run them independently.

Bibliography

[1] A. O. G. Wallis, H. I. B. Banks, and A. Emmanouilidou. Traces in ion yields and electron spectra of the formation of Ar inner-shell hollow states by free-electron lasers. *Phys. Rev. A*, 91:063402, Jun 2015.

[2] H. I. B. Banks, D. A. Little, J. Tennyson, and A. Emmanouilidou. Interaction of molecular nitrogen with free-electron-laser radiation. *Phys. Chem. Chem. Phys.*, 19:19794–19806, 2017.

[3] H. I. B. Banks, D. A. Little, and A. Emmanouilidou. Multiple core-hole formation by free-electron laser radiation in molecular nitrogen. *Journal of Physics B: Atomic, Molecular and Optical Physics*, 51(9):095001, 2018.

[4] C. Pellegrini. The history of X-ray free-electron lasers. *European Physical Journal H*, 37:659–708, October 2012.

[5] C Bostedt, John Bozek, P H Bucksbaum, Ryan Coffee, J B Hastings, Z Huang, Richard Lee, Sebastian Schorb, J N Corlett, P Denes, P Emma, Roger Falcone, R W Schoenlein, Gilles Doumy, Elliot Kanter, Bertold Krssig, S Southworth, L Young, Li Fang, and Louis Dimauro. Ultra-fast and ultra-intense x-ray sciences: First results from the linac coherent light source free-electron laser. *Journal of Physics B: Atomic, Molecular and Optical Physics*, 46:164003, 08 2013.

[6] J. P. Marangos. Introduction to the new science with x-ray free electron lasers. *Contemporary Physics*, 52(6):551–569, 2011.

[7] J. Ullrich, A. Rudenko, and R. Moshammer. Free-electron lasers: New avenues in molecular physics and photochemistry. *Annual Review of Physical Chemistry*, 63(1):635–660, 2012. PMID: 22404584.

[8] M.N. Piancastelli, M. Simon, and K. Ueda. Present trends and future perspectives for atomic and molecular physics at the new x-ray light sources. *Journal of Electron Spectroscopy and Related Phenomena*, 181(2):98 – 110, 2010. Electronic Spectroscopy and Structure (ICESS-11).

[9] Richard Neutze, Remco Wouts, David van der Spoel, Edgar Weckert, and Janos Hajdu. Potential for biomolecular imaging with femtosecond x-ray pulses. *Nature*, 406:752–757, 2000.

[10] Henry N. Chapman, Anton Barty, Michael J. Bogan, Sébastien Boutet, Matthias Frank, Stefan P. Hau-Riege, Stefano Marchesini, Bruce W. Woods, Saša Bajt, W. Henry Benner, Richard A. London, Elke Plönjes, Marion Kuhlmann, Rolf Treusch, Stefan Düsterer, Thomas Tschentscher, Jochen R. Schneider, Eberhard Spiller, Thomas Möller, Christoph Bostedt, Matthias Hoener, David A. Shapiro, Keith O. Hodgson, David van der Spoel, Florian Burmeister, Magnus Bergh, Carl Caleman, Gösta Huldt, M. Marvin Seibert, Filipe R. N. C. Maia, Richard W. Lee, Abraham Szöke, Nicusor Timneanu, and Janos Hajdu. Femtosecond diffractive imaging with a soft-x-ray free-electron laser. *Nature Physics*, 2:839 EP –, 11 2006.

[11] Ilme Schlichting and Jianwei Miao. Emerging opportunities in structural biology with x-ray free-electron lasers. *Current Opinion in Structural Biology*, 22(5):613 – 626, 2012.

[12] Lars Redecke, Karol Nass, Daniel P. DePonte, Thomas A. White, Dirk Rehders, Anton Barty, Francesco Stellato, Mengning Liang, Thomas R.M. Barends, Sébastien Boutet, Garth J. Williams, Marc Messerschmidt, M. Marvin Seibert, Andrew Aquila, David Arnlund, Sasa Bajt, Torsten Barth, Michael J. Bogan, Carl Caleman, Tzu-Chiao Chao, R. Bruce Doak, Hol-

ger Fleckenstein, Matthias Frank, Raimund Fromme, Lorenzo Galli, Ingo Grotjohann, Mark S. Hunter, Linda C. Johansson, Stephan Kassemeyer, Gergely Katona, Richard A. Kirian, Rudolf Koopmann, Chris Kupitz, Lukas Lomb, Andrew V. Martin, Stefan Mogk, Richard Neutze, Robert L. Shoeman, Jan Steinbrener, Nicusor Timneanu, Dingjie Wang, Uwe Weierstall, Nadia A. Zatsepin, John C. H. Spence, Petra Fromme, Ilme Schlichting, Michael Duszenko, Christian Betzel, and Henry N. Chapman. Natively inhibited trypanosoma brucei cathepsin B structure determined by using an x-ray laser. *Science*, 339(6116):227–230, 2013.

[13] L. S. Cederbaum, F. Tarantelli, A. Sgamellotti, and J. Schirmer. On double vacancies in the core. *The Journal of Chemical Physics*, 85(11):6513–6523, 1986.

[14] L. S. Cederbaum, F. Tarantelli, A. Sgamellotti, and J. Schirmer. Double vacancies in the core of benzene. *The Journal of Chemical Physics*, 86(4):2168–2175, 1987.

[15] Motomichi Tashiro, Masahiro Ehara, Hironobu Fukuzawa, Kiyoshi Ueda, Christian Buth, Nikolai V. Kryzhevoi, and Lorenz S. Cederbaum. Molecular double core hole electron spectroscopy for chemical analysis. *The Journal of Chemical Physics*, 132(18):184302, 2010.

[16] P. Salén, P. van der Meulen, H. T. Schmidt, R. D. Thomas, M. Larsson, R. Feifel, M. N. Piancastelli, L. Fang, B. Murphy, T. Osipov, N. Berrah, E. Kukk, K. Ueda, J. D. Bozek, C. Bostedt, S. Wada, R. Richter, V. Feyer, and K. C. Prince. Experimental verification of the chemical sensitivity of two-site double core-hole states formed by an x-ray free-electron laser. *Phys. Rev. Lett.*, 108:153003, Apr 2012.

[17] Nora Berrah, Li Fang, Brendan Murphy, Timur Osipov, Kiyoshi Ueda, Edwin Kukk, Raimund Feifel, Peter van der Meulen, Peter Salen, Henning T. Schmidt, Richard D. Thomas, Mats Larsson, Robert Richter, Kevin C.

Prince, John D. Bozek, Christoph Bostedt, Shin-ichi Wada, Maria N. Piancastelli, Motomichi Tashiro, and Masahiro Ehara. Double-core-hole spectroscopy for chemical analysis with an intense x-ray femtosecond laser. *Proceedings of the National Academy of Sciences*, 108(41):16912–16915, 2011.

[18] Robin Santra, Nikolai V. Kryzhevoi, and Lorenz S. Cederbaum. X-ray two-photon photoelectron spectroscopy: A theoretical study of inner-shell spectra of the organic para-aminophenol molecule. *Phys. Rev. Lett.*, 103:013002, Jul 2009.

[19] L. Fang, M. Hoener, O. Gessner, F. Tarantelli, S. T. Pratt, O. Kornilov, C. Buth, M. Gühr, E. P. Kanter, C. Bostedt, J. D. Bozek, P. H. Bucksbaum, M. Chen, R. Coffee, J. Cryan, M. Glownia, E. Kukk, S. R. Leone, and N. Berrah. Double core-hole production in N_2: Beating the Auger clock. *Phys. Rev. Lett.*, 105:083005, Aug 2010.

[20] L. Fang, T. Osipov, B. Murphy, F. Tarantelli, E. Kukk, J. P. Cryan, M. Glownia, P. H. Bucksbaum, R. N. Coffee, M. Chen, C. Buth, and N. Berrah. Multi-photon ionization as a clock to reveal molecular dynamics with intense short x-ray free electron laser pulses. *Phys. Rev. Lett.*, 109:263001, Dec 2012.

[21] V Zhaunerchyk, M Kamiska, M Mucke, R J Squibb, J H D Eland, M N Piancastelli, L J Frasinski, J Grilj, M Koch, B K McFarland, E Sistrunk, M Gühr, R N Coffee, C Bostedt, J D Bozek, P Salén, P v d Meulen, P Linusson, R D Thomas, M Larsson, L Foucar, J Ullrich, K Motomura, S Mondal, K Ueda, R Richter, K C Prince, O Takahashi, T Osipov, L Fang, B F Murphy, N Berrah, and R Feifel. Disentangling formation of multiple-core holes in aminophenol molecules exposed to bright X-FEL radiation. *Journal of Physics B: Atomic, Molecular and Optical Physics*, 48(24):244003, 2015.

[22] Christian Buth, James P. Cryan, James M. Glownia, Matthias Hoener, Ryan N. Coffee, and Nora Berrah. Ultrafast absorption of intense x-rays

by nitrogen molecules. *The Journal of Chemical Physics*, 136(21):214310, 2012.

[23] Ji-Cai Liu, Nora Berrah, Lorenz S Cederbaum, James P Cryan, James M Glownia, Kenneth J Schafer, and Christian Buth. Rate equations for nitrogen molecules in ultrashort and intense x-ray pulses. *Journal of Physics B: Atomic, Molecular and Optical Physics*, 49(7):075602, 2016.

[24] V. Carravetta and H. Ågren. Symmetry breaking and hole localization in multiple core electron ionization. *The Journal of Physical Chemistry A*, 117(31):6798–6802, 2013. PMID: 23859627.

[25] L. B. Madsen and P. Lambropoulos. Line shapes in photoexcitation of triply excited hollow states. *Journal of Physics B: Atomic, Molecular and Optical Physics*, 34(10):1855, 2001.

[26] Cheng Gao, Yongjun Li, Pengfei Liu, Xiaohui Fan, and Jiaolong Zeng. Triple-core-hole states produced in the interaction of solid-state density plasmas with a relativistic femtosecond optical laser. *Scientific Reports*, 8, 12 2018.

[27] A. A. Sorokin, S. V. Bobashev, T. Feigl, K. Tiedtke, H. Wabnitz, and M. Richter. Photoelectric effect at ultrahigh intensities. *Phys. Rev. Lett.*, 99:213002, Nov 2007.

[28] L. Young, E. P. Kanter, B. Krässig, Y. Li, A. M. March, S. T. Pratt, R. Santra, S. H. Southworth, N. Rohringer, L. F. DiMauro, G. Doumy, C. A. Roedig, N. Berrah, L. Fang, M. Hoener, P. H. Bucksbaum, J. P. Cryan, S. Ghimire, J. M. Glownia, D. A. Reis, J. D. Bozek, C. Bostedt, and M. Messerschmidt. Femtosecond electronic response of atoms to ultra-intense x-rays. *Nature*, 466:56 EP –, 07 2010.

[29] G. Doumy, C. Roedig, S.-K. Son, C. I. Blaga, A. D. DiChiara, R. Santra, N. Berrah, C. Bostedt, J. D. Bozek, P. H. Bucksbaum, J. P. Cryan, L. Fang,

S. Ghimire, J. M. Glownia, M. Hoener, E. P. Kanter, B. Krässig, M. Kuebel, M. Messerschmidt, G. G. Paulus, D. A. Reis, N. Rohringer, L. Young, P. Agostini, and L. F. DiMauro. Nonlinear atomic response to intense ultrashort x rays. *Phys. Rev. Lett.*, 106:083002, Feb 2011.

[30] B. F. Murphy, L. Fang, M.-H. Chen, J. D. Bozek, E. Kukk, E. P. Kanter, M. Messerschmidt, T. Osipov, and N. Berrah. Multiphoton l-shell ionization of H_2S using intense x-ray pulses from a free-electron laser. *Phys. Rev. A*, 86:053423, Nov 2012.

[31] H. Fukuzawa, S.-K. Son, K. Motomura, S. Mondal, K. Nagaya, S. Wada, X.-J. Liu, R. Feifel, T. Tachibana, Y. Ito, M. Kimura, T. Sakai, K. Matsunami, H. Hayashita, J. Kajikawa, P. Johnsson, M. Siano, E. Kukk, B. Rudek, B. Erk, L. Foucar, E. Robert, C. Miron, K. Tono, Y. Inubushi, T. Hatsui, M. Yabashi, M. Yao, R. Santra, and K. Ueda. Deep inner-shell multiphoton ionization by intense x-ray free-electron laser pulses. *Phys. Rev. Lett.*, 110:173005, Apr 2013.

[32] L. J. Frasinski, V. Zhaunerchyk, M. Mucke, R. J. Squibb, M. Siano, J. H. D. Eland, P. Linusson, P. v.d. Meulen, P. Salén, R. D. Thomas, M. Larsson, L. Foucar, J. Ullrich, K. Motomura, S. Mondal, K. Ueda, T. Osipov, L. Fang, B. F. Murphy, N. Berrah, C. Bostedt, J. D. Bozek, S. Schorb, M. Messerschmidt, J. M. Glownia, J. P. Cryan, R. N. Coffee, O. Takahashi, S. Wada, M. N. Piancastelli, R. Richter, K. C. Prince, and R. Feifel. Dynamics of hollow atom formation in intense x-ray pulses probed by partial covariance mapping. *Phys. Rev. Lett.*, 111:073002, Aug 2013.

[33] A. O. G. Wallis, L. Lodi, and A. Emmanouilidou. Auger spectra following inner-shell ionization of argon by a free-electron laser. *Phys. Rev. A*, 89:063417, Jun 2014.

[34] M. G. Makris, P. Lambropoulos, and A. Mihelič. Theory of multiphoton multielectron ionization of xenon under strong 93-eV radiation. *Phys. Rev. Lett.*, 102:033002, Jan 2009.

[35] H Pulkkinen, S Aksela, O-P Sairanen, A Hiltunen, and H Aksela. Correlation effects in the $L_{2,3}$ - MM Auger transitions of Ar. *Journal of Physics B: Atomic, Molecular and Optical Physics*, 29(14):3033, 1996.

[36] P. Lablanquie, L. Andric, J. Palaudoux, U. Becker, M. Braune, J. Viefhaus, J.H.D. Eland, and F. Penent. Multielectron spectroscopy: Auger decays of the argon 2p hole. *Journal of Electron Spectroscopy and Related Phenomena*, 156–158:51 – 57, 2007. Electronic Spectroscopy and Structure: ICESS-10.

[37] C. P. Bhalla, N. O. Folland, and M. A. Hein. Theoretical K-shell Auger rates, transition energies, and fluorescence yields for multiply ionized neon. *Phys. Rev. A*, 8:649–657, Aug 1973.

[38] Sang-Kil Son and Robin Santra. Monte Carlo calculation of ion, electron, and photon spectra of xenon atoms in x-ray free-electron laser pulses. *Phys. Rev. A*, 85:063415, Jun 2012.

[39] S.-M. Huttula, P. Lablanquie, L. Andric, J. Palaudoux, M. Huttula, S. Sheinerman, E. Shigemasa, Y. Hikosaka, K. Ito, and F. Penent. Decay of a $2p$ inner-shell hole in an Ar^+ ion. *Phys. Rev. Lett.*, 110:113002, Mar 2013.

[40] Nina Rohringer and Robin Santra. X-ray nonlinear optical processes using a self-amplified spontaneous emission free-electron laser. *Phys. Rev. A*, 76:033416, Sep 2007.

[41] Yajiang Hao, Ludger Inhester, Kota Hanasaki, Sang-Kil Son, and Robin Santra. Efficient electronic structure calculation for molecular ionization dynamics at high x-ray intensity. *Structural Dynamics*, 2(4):041707, 2015.

[42] Zoltan Jurek, Sang-Kil Son, Beata Ziaja, and Robin Santra. *XMDYN* and *XATOM*: versatile simulation tools for quantitative modeling of X-ray free-

electron laser induced dynamics of matter. *Journal of Applied Crystallography*, 49(3):1048–1056, Jun 2016.

[43] Ludger Inhester, Kota Hanasaki, Yajiang Hao, Sang-Kil Son, and Robin Santra. X-ray multiphoton ionization dynamics of a water molecule irradiated by an x-ray free-electron laser pulse. *Phys. Rev. A*, 94:023422, Aug 2016.

[44] B. Erk, D. Rolles, L. Foucar, B. Rudek, S. W. Epp, M. Cryle, C. Bostedt, S. Schorb, J. Bozek, A. Rouzee, A. Hundertmark, T. Marchenko, M. Simon, F. Filsinger, L. Christensen, S. De, S. Trippel, J. Küpper, H. Stapelfeldt, S. Wada, K. Ueda, M. Swiggers, M. Messerschmidt, C. D. Schröter, R. Moshammer, I. Schlichting, J. Ullrich, and A. Rudenko. Ultrafast charge rearrangement and nuclear dynamics upon inner-shell multiple ionization of small polyatomic molecules. *Phys. Rev. Lett.*, 110:053003, Jan 2013.

[45] Paola Bolognesi, Marcello Coreno, Lorenzo Avaldi, Loriano Storchi, and Francesco Tarantelli. Site-selected Auger electron spectroscopy of N_2O. *The Journal of Chemical Physics*, 125(5):054306, 2006.

[46] V. Feyer, P. Bolognesi, M. Coreno, K. C. Prince, L. Avaldi, L. Storchi, and F. Tarantelli. Effects of nuclear dynamics in the low-kinetic-energy Auger spectra of CO and CO_2. *The Journal of Chemical Physics*, 123(22):224306, 2005.

[47] R Püttner, H Fukuzawa, X-J Liu, S K Semenov, N A Cherepkov, T Tanaka, M Hoshino, H Tanaka, and K Ueda. State-dependent gerade/ungerade intensity ratios in the Auger spectrum of N_2. *Journal of Physics B: Atomic, Molecular and Optical Physics*, 41(14):141001, 2008.

[48] H. Iwayama, N. Sisourat, P. Lablanquie, F. Penent, J. Palaudoux, L. Andric, J. H. D. Eland, K. Bučar, M. Žitnik, Y. Velkov, Y. Hikosaka, M. Nakano, and E. Shigemasa. A local chemical environment effect in site-specific

Auger spectra of ethyl trifluoroacetate. *The Journal of Chemical Physics*, 138(2):024306, 2013.

[49] L. Storchi, F. Tarantelli, S. Veronesi, P. Bolognesi, E. Fainelli, and L. Avaldi. The Auger spectroscopy of pyrimidine and halogen-substituted pyrimidines. *The Journal of Chemical Physics*, 129(15):154309, 2008.

[50] S.L. Sorensen, C. Miron, R. Feifel, M.-N. Piancastelli, O. Björneholm, and S. Svensson. The influence of the resonance on the Auger decay of core-ionized molecular nitrogen. *Chemical Physics Letters*, 456(13):1 − 6, 2008.

[51] W J Griffiths, N Correia, M P Keane, A Naves de Brito, S Svensson, and L Karlsson. Doubly ionized states of N_2O studied by photon-induced Auger electron and double charge transfer spectroscopies. *Journal of Physics B: Atomic, Molecular and Optical Physics*, 24(19):4187, 1991.

[52] Ph. V. Demekhin, A. Ehresmann, and V. L. Sukhorukov. Single center method: A computational tool for ionization and electronic excitation studies of molecules. *The Journal of Chemical Physics*, 134(2):024113, 2011.

[53] J P Cryan, J M Glownia, J Andreasson, A Belkacem, N Berrah, C I Blaga, C Bostedt, J Bozek, N A Cherepkov, L F DiMauro, L Fang, O Gessner, M Gühr, J Hajdu, M P Hertlein, M Hoener, O Kornilov, J P Marangos, A M March, B K McFarland, H Merdji, M Messerschmidt, V S Petrović, C Raman, D Ray, D A Reis, S K Semenov, M Trigo, J L White, W White, L Young, P H Bucksbaum, and R N Coffee. Molecular frame Auger electron energy spectrum from N_2. *Journal of Physics B: Atomic, Molecular and Optical Physics*, 45(5):055601, 2012.

[54] K. Ueda, R. Püttner, N. A. Cherepkov, F. Gel'mukhanov, and M. Ehara. High resolution x-ray photoelectron spectroscopy on nitrogen molecules. *The European Physical Journal Special Topics*, 169(1):95–107, 2009.

[55] M. Hoener, L. Fang, O. Kornilov, O. Gessner, S. T. Pratt, M. Gühr, E. P. Kanter, C. Blaga, C. Bostedt, J. D. Bozek, P. H. Bucksbaum, C. Buth, M. Chen,

R. Coffee, J. Cryan, L. DiMauro, M. Glownia, E. Hosler, E. Kukk, S. R. Leone, B. McFarland, M. Messerschmidt, B. Murphy, V. Petrovic, D. Rolles, and N. Berrah. Ultraintense x-ray induced ionization, dissociation, and frustrated absorption in molecular nitrogen. *Phys. Rev. Lett.*, 104:253002, Jun 2010.

[56] Kiyoshi Ueda. To be or not to be localized. *Science*, 320(5878):884–885, 2008.

[57] D. Coster and R. De L. Kronig. New type of Auger effect and its influence on the x-ray spectrum. *Physica*, 2(1–12):13 – 24, 1935.

[58] Wolfgang Pauli. *Wave Mechanics: Volume 5 of Pauli Lectures on Physics*. Wiley, 2000.

[59] V. Shevelko and H. Tawara. *Atomic Processes in Basic and Applied Physics*. Springer, 2012.

[60] B. W. Shore and D. H. Menzel. *Principles of Atomic Spectra*. Wiley, 1968.

[61] J. J. Sakurai. *Modern Quantum Mechanics*. Addison-Wesley, 1994.

[62] A. R. Edmonds. *Angular Momentum in Quantum Mechanics*. Princeton University Press, 1960.

[63] Richard Zare. *Angular Momentum: understanding spatial aspects in chemistry and physics*. Wiley, 1988.

[64] B H Bransden and C J Joachain. *Physics of Atoms and Molecules*. Pearson Education, 2003.

[65] J. C. Slater. A simplification of the Hartree-Fock method. *Phys. Rev.*, 81:385–390, Feb 1951.

[66] Merle E. Riley and Donald G. Truhlar. Approximations for the exchange potential in electron scattering. *The Journal of Chemical Physics*, 63(5):2182–2191, 1975.

[67] Frank Herman and Sherwood Skillman. *Atomic structure calculations*. Prentice-Hall, New Jersey, 1963.

[68] M.   D   Pauli.   Herman-Skillman   program. http://hermes.phys.uwm.edu/projects/elecstruct/hermsk/HS.TOC.html.

[69] Lampros A. A. Nikolopoulos. Calculation method for the continuum states of atomic systems. *Central European Journal of Physics*, 11(9):1074–1081, Sep 2013.

[70] Ian J. Thompson and Filomena M. Nunes. *Nuclear Reactions for Astrophysics*. Cambridge University Press, 2009.

[71] H. J. Werner, P. J. Knowles, R. Lindh, F. R. Manby, M. Schütz, et al. MOLPRO, a package of ab initio programs, 2010. see http://www.molpro.net/.

[72] Los Alamos National Laboratory Atomic Physics Codes; see http://aphysics2.lanl.gov/tempweb/lanl/.

[73] Mau Hsiung Chen and Bernd Crasemann. Multiplet effects on the $L_{2,3}$ fluorescence yield of multiply ionized ar. *Phys. Rev. A*, 10:2232–2239, Dec 1974.

[74] Pascal Lablanquie, Saana-Maija Huttula, Marko Huttula, Lidija Andric, Jerome Palaudoux, John H. D. Eland, Yasumasa Hikosaka, Eiji Shigemasa, Kenji Ito, and Francis Penent. Multi-electron spectroscopy: Auger decays of the argon 2s hole. *Phys. Chem. Chem. Phys.*, 13:18355–18364, 2011.

[75] F. von Busch, U. Kuetgens, J. Doppelfeld, and S. Fritzsche. $L_{23}[L_{23}] - MM[L_{23}]$ and $L_{23}[M^2] - MM[M^2]$ Auger vacancy satellite spectra of argon. *Phys. Rev. A*, 59:2030–2042, Mar 1999.

[76] U. Alkemper, J. Doppelfeld, and F. von Busch. $L_{23} - MM$ Auger spectrum of K-ionized argon: Decomposition by electron-ion and electron-electron coincidence techniques. *Phys. Rev. A*, 56:2741–2749, Oct 1997.

[77] F von Busch, J Doppelfeld, C Gunther, and E Hartmann. Argon $L_{23} - MM$ Auger satellite spectrum emitted after K ionization. *Journal of Physics B: Atomic, Molecular and Optical Physics*, 27(11):2151, 1994.

[78] Nguyên Trong Anh. *Frontier Orbitals*. Wiley, 2007.

[79] S. F. Boys. Electronic wave functions - I. a general method of calculation for the stationary states of any molecular system. *Proceedings of the Royal Society of London A: Mathematical, Physical and Engineering Sciences*, 200(1063):542–554, 1950.

[80] Ira N. Levine. *Quantum Chemistry*. Prentice-Hall, 2000.

[81] R. Ditchfield, W. J. Hehre, and J. A. Pople. Self-consistent molecular-orbital methods. IX. an extended gaussian-type basis for molecular-orbital studies of organic molecules. *The Journal of Chemical Physics*, 54(2):724–728, 1971.

[82] A. D. McLean and G. S. Chandler. Contracted gaussian basis sets for molecular calculations. I. Second row atoms, Z=11-18. *The Journal of Chemical Physics*, 72(10):5639–5648, 1980.

[83] Eugene J. McGuire. *L*-shell Auger and Coster-Kronig electron spectra. *Phys. Rev. A*, 3:1801–1810, Jun 1971.

[84] K G Dyall and F P Larkins. Satellite structure in atomic spectra. IV. the $L_{23} - MM$ Auger spectrum of argon. *Journal of Physics B: Atomic and Molecular Physics*, 15(17):2793, 1982.

[85] A. Nayak, I. Orfanos, I. Makos, M. Dumergue, S. Kühn, E. Skantzakis, B. Bodi, K. Varju, C. Kalpouzos, H. I. B. Banks, A. Emmanouilidou, D. Charalambidis, and P. Tzallas. Multiple ionization of argon via multi-xuv-photon absorption induced by 20-gw high-order harmonic laser pulses. *Phys. Rev. A*, 98:023426, Aug 2018.

[86] L. Inhester, C. F. Burmeister, G. Groenhof, and H. Grubmüller. Auger spectrum of a water molecule after single and double core ionization. *The Journal of Chemical Physics*, 136(14), 2012.

[87] L. Inhester, G. Groenhof, and H. Grubmller. Core hole screening and decay rates of double core ionized first row hydrides. *The Journal of Chemical Physics*, 138(16):164304, 2013.

[88] M.Y Amusia and L.V Chernysheva. *Computation of Atomic Processes: A Handbook for the ATOM Programs*. CRC Press, 1997.

[89] Ian J. Thompson and Filomena M. Nunes. *Nuclear Reactions for Astrophysics*. Cambridge University Press, 2009.

[90] Joe D. Hoffman and Steven Frankel. *Numerical Methods for Engineers and Scientists*. CRC Press, 2001.

[91] M. Abramowitz and I. Stegun. *Handbook of Mathematical Functions*. Dover Publications, 1965. available online.

[92] Yu lin Xu. Fast evaluation of gaunt coefficients: recursive approach. *Journal of Computational and Applied Mathematics*, 85(1):53 – 65, 1997.

[93] Thom H. Dunning Jr. Gaussian basis sets for use in correlated molecular calculations. I. the atoms boron through neon and hydrogen. *The Journal of Chemical Physics*, 90(2):1007–1023, 1989.

[94] G. B. Arfken and H. J. Weber. *Mathematical Methods for Physicists*. Elsevier, 2005.

[95] C Beylerian and C Cornaggia. Coulomb explosion imaging of fragmentation channels following laser-induced double ionization of N_2. *Journal of Physics B: Atomic, Molecular and Optical Physics*, 37(13):L259, 2004.

[96] S. K. Semenov, N. A. Cherepkov, G. H. Fecher, and G. Schönhense. Generalization of the atomic random-phase-approximation method for diatomic

molecules: N_2 photoionization cross-section calculations. *Phys. Rev. A*, 61:032704, Feb 2000.

[97] C M Liegener. Calculations on the Auger spectrum of N_2. *Journal of Physics B: Atomic and Molecular Physics*, 16(23):4281, 1983.

[98] Hans Ågren. On the interpretation of molecular valence Auger spectra. *The Journal of Chemical Physics*, 75(3):1267–1283, 1981.

[99] Mary Coville and T. Darrah Thomas. Molecular effects on inner-shell lifetimes: Possible test of the one-center model of Auger decay. *Phys. Rev. A*, 43:6053–6056, Jun 1991.

[100] U. Hergenhahn, O. Kugeler, A. Rüdel, E. E. Rennie, and A. M. Bradshaw. Symmetry-selective observation of the N 1s shape resonance in N_2. *The Journal of Physical Chemistry A*, 105(23):5704–5708, 2001.

[101] M. S. Schöffler, J. Titze, N. Petridis, T. Jahnke, K. Cole, L. Ph. H. Schmidt, A. Czasch, D. Akoury, O. Jagutzki, J. B. Williams, N. A. Cherepkov, S. K. Semenov, C. W. McCurdy, T. N. Rescigno, C. L. Cocke, T. Osipov, S. Lee, M. H. Prior, A. Belkacem, A. L. Landers, H. Schmidt-Böcking, Th. Weber, and R. Dörner. Ultrafast probing of core hole localization in N_2. *Science*, 320(5878):920–923, 2008.

[102] P. A. M. Dirac. On the theory of quantum mechanics. *Proceedings of the Royal Society of London. Series A, Containing Papers of a Mathematical and Physical Character*, 112(762):661–677, 1926.

[103] S. J. Blundell and K. M. Blundell. *Concepts in Thermal Physics*. Oxford University Press, 2006.

[104] H. Friedrich. *Theoretical Atomic Physics*. Springer, 2003.

[105] M. Razavy. Scattering by non-local potentials. *Nuclear Physics*, 78(2):256 – 264, 1966.

[106] https://www.gnu.org/software/gsl/.

[107] https://github.com/joeydumont/wignerSymbols.

[108] http://www.boost.org.

[109] K. F. Riley, M. P. Hobson, and S. J. Bence. *Modern Quantum Chemistry*. Dover Publications, 1996.